Mextram Model Development for Improved Distortion Modeling of SiGe HBTs

by

Huaiyuan Zhang

A dissertation submitted to the Graduate Faculty of
Auburn University
in partial fulfillment of the
requirements for the Degree of
Doctor of Philosophy

Auburn, Alabama
December 14, 2019

Keywords: SiGe HBT, linearity, avalanche, depletion capacitance

Approved by

Guofu Niu, Chair, Professor of Electrical and Computer Engineering
Fa Dai, Professor of Electrical and Computer Engineering
Bogdan Wilamowski, Professor of Electrical and Computer Engineering
Michael Hamilton, Professor of Electrical and Computer Engineering

Abstract

Linearity of SiGe HBTs has been widely studied nowadays. The accuracy on modeling of the third order intercept point (IP3) always puts strict requirements on compact models that can reproduce measured IP3 characteristics in advanced SiGe HBT technologies. In this dissertation, two options of collector-base (CB) depletion capacitance model have been presented to correctly model IP3 peak and high injection base-collector capacitance (C_{BC}) for a common-emitter SiGe HBT. A new technique to implement Volterra series with complete Mextram model is proposed. A new extended avalanche model with excellence in wide temperature range and current dependence at high injection has been verified to have improved IP3 dependence for common-base SiGe HBT.

For common-emitter SiGe HBT, the measured and simulated magnitude, real and imaginary part of third order output current ($i_{2,3rd}$) are compared near the IP3 peak. The simulated $i_{2,3rd}$ from Mextram 504.12 shows that its imaginary part dominates over the real part and is much higher than measurement. This points to C_{BC} modeling as an issue for IP3 peak modeling. Two new options of CB depletion capacitance model are then presented to correctly model the bias dependence of peak IP3. Also, the influence of each CB depletion capacitance model on peak cut-off frequency (f_T) and high injection C_{BC} are examined.

For common-base SiGe HBT, the avalanche model plays a critical role in accuracy of modeling IP3 dependence on both V_{CB} and I_E. An avalanche factor (M-1) model with improved CB voltage V_{CB} and collector current I_C dependence is first developed, which semi-empirically models the decrease of M-1 with increasing current. This was implemented in the official release of Mextram 505.00. To further improve the description of current dependence of M-1, another model is developed based on modeling the evolution of the peak electric field. This allows a more physical description of the decrease of M-1 at relatively lower I_C, and the rise of M-1 at high I_C when the electrical CB junction interface shifts from the original metallurgical junction to the epi-layer/buried layer interface. Parameters are also introduced to model the

transition region between the low I_C and high I_C cases. This new extended avalanche model enables accurate fitting of the emitter current dependence of base current at high V_{CB} up to a high level of injection above peak f_T roll-off, which was not possible with existing avalanche models.

To understand the V_{CB} and V_{BE} dependences of IP3, as well as to identify the physical mechanisms of IP3 peak, a Volterra series analysis program is developed with a modified circuit topology that more closely resembles that of an ideal transistor equivalent circuit where the base-emitter and base-collector voltages control all circuit elements. Symbolic analysis is carried out to yield analytically the first order derivatives of all circuit elements on the two control voltages. Higher order derivatives are evaluated using numerical differentiation, with special attention paid to the handling of self heating. The validity of the Volterra series analysis program is verified by comparison with harmonic balance simulations at a lower RF power level.

A unique advantage of Volterra series is that nonlinearities from various circuit elements can be turned on and off individually, in a fashion similar to linear circuit analysis. The responses add to each other, and IP3 peak occurs when the responses cancel each other. Among 25 nonlinearities, the main current nonlinearity (I_N) including epi-layer high injection effect and the avalanche current nonlinearity (I_{AVL}) are found to dominate. The cancellation between these two dominant nonlinearities leads to IP3 peaks for both V_{CB} dependence and V_{BE} dependence.

A detailed evaluation is made on the IP3 modeling capability of Mextram 504.12, 505.00, and the newly developed extended avalanche model. The main difference lies in common-base configuration at high V_{CB} and I_E. The new model overall allows much more accurate DC modeling, much improved V_{CB} dependence modeling, and much improved V_{BE}/I_E dependence modeling.

Acknowledgments

I would like to express my grateful thanks to my advisor, Dr. Guofu Niu, whose helps in life and studies make this dissertation to be possible. I appreciate him for his famous reputation and authority that bring me to front edge of research in electronic devices. His encouragement always inspires me to face every challenge and his vast knowledge always illuminates me the right direction. His serious attitude and devotion to science have been deeply impressed in my brain, which will guide me to advance in my future life. I would also like to thank the other committee members, Dr. Fa Dai, Dr. Bogdan Wilamowski and Dr. Michael Hamilton for their kind assistances in both my studies and research.

Several people deserve special recognition for their contributions to this work. I would like to thank Dr. A. J. Scholten, Dr. M. B. Willemsen and Dr. R. M. T. Pijper of NXP Semiconductors for their great helps in measurement data and discussion. I would like to thank Dr. W. Chen of Texas Instruments, Dr. G. Coram of Analog Devices. and Dr. J. Xie of Cadence. for their helps with model testing and implementation in Mextram.

Finally, I would like to thank my parents for their support and confidence on me through my entire life. Without them, I would never have begun my studies abroad and finished this dissertation.

Table of Contents

List of Figures

List of Tables

Chapter 1

Introduction

Linearity of SiGe HBTs has been widely studied. The third order intercept point (IP3) is important for RF design and requires accurate compact models that can reproduce measured IP3 characteristics, particularly for optimization of transistor bias [5] [6] [7] [8]. While modern compact models do a good job with IP3 modeling at relatively low injection level, accurate high injection IP3 modeling is much more challenging [9] [10]. Part of the difficulty is that there is no dedicated model parameter to tune IP3 separately from DC I-V and S-parameters, and accurate higher order derivatives of I-V and C-V are required.

1.1 Measurement

In this dissertation, all the following data both in common-emitter and common-base SiGe HBTs are measured by NXP Semiconductors: DC I-V curves on RF structure, S-parameters and X-parameters.

For DC measurement, cable resistances are first measured and extracted. The typical gummel curve, forced-I_E and output curves on transistors are then obtained. Fig. 1.1(a) shows a diagram of DUT with probes pads and interconnects parasitics. Z_1, Z_2 and Z_3 represent series parasitics. Y_1, Y_2 and Y_3 represent parallel parasitics. For S-parameter measurement, OPEN, SHORT and DUT are separately measured at frequency from 0.1 to 45 GHz and at each bias. Then open-short de-embedding method [11] is applied to extract capacitances and f_T without influence of parasitics. Fig. 1.1(b) shows a diagram of X-parameter measurement. The real, imaginary and magnitude parts of complex AC currents i_1, i_2 and voltages v_1, v_2 at f_0, $2f_0$,

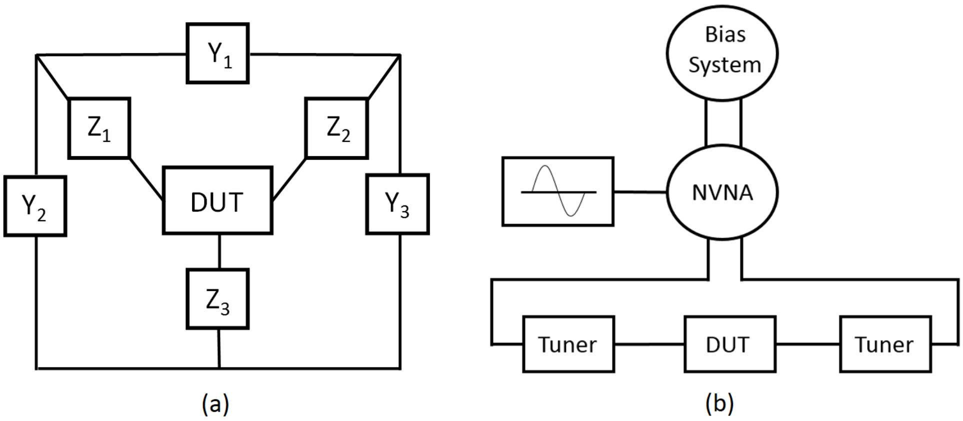

Figure 1.1: A diagram of (a) DUT with parasitics and (b) X-parameter measurement.

$3f_0$ are obtained. The fundamental frequency f_0 = 2 GHz. i_1 and i_2 equal emitter and collector current respectively. OIP3 can then be calculated by

$$P_{out}(f_0) = \frac{1}{2}\Re(v_2(f_0) \times i_2^*(f_0)), \tag{1.1}$$

$$P_{out}(3f_0) = \frac{1}{2}\Re(v_2(3f_0) \times i_2^*(3f_0)). \tag{1.2}$$

where "$\Re$" stands for real part, "*" denotes conjugate. OIP3 in dBm is calculated as

$$\text{OIP3}|_{\text{dBm}} = 10\log_{10}\left(\frac{P_{out}^3(f_0)}{P_{out}(3f_0)}\right) + 30\text{ dBm}. \tag{1.3}$$

(1.3) assumes that the slopes of P_{out} (dBm) versus available source power P_{avs} (dBm) are 1:1 and 3:1 at f_0 and $3f_0$, respectively. $P_{avs} = A^2/8R_s$ [4] is set to -30 dBm to ensure these assumptions are satisfied. Fig. 1.2 shows real, imaginary and magnitude parts of i_2-V_{BE} at DC, AC and harmonics for V_{CB} = 3.75 V as the common-base OIP3 in Fig. 1.14. The magnitude of i_2 decreases at higher orders, which makes the accuracy of measured i_2 difficult. It is clear to see V_{BE} dependence of $i_{2,3rd}$ determines OIP3 trend, as $i_{2,1st}$ is weakly dependent on V_{BE}. So $i_{2,3rd}$ determines OIP3 trend for V_{CB} dependence.

It should be noted that the X-parameter measurement is very challenging, particularly for common-base, as the linearity is very high, and nonlinearities of measuring instruments can come into play.

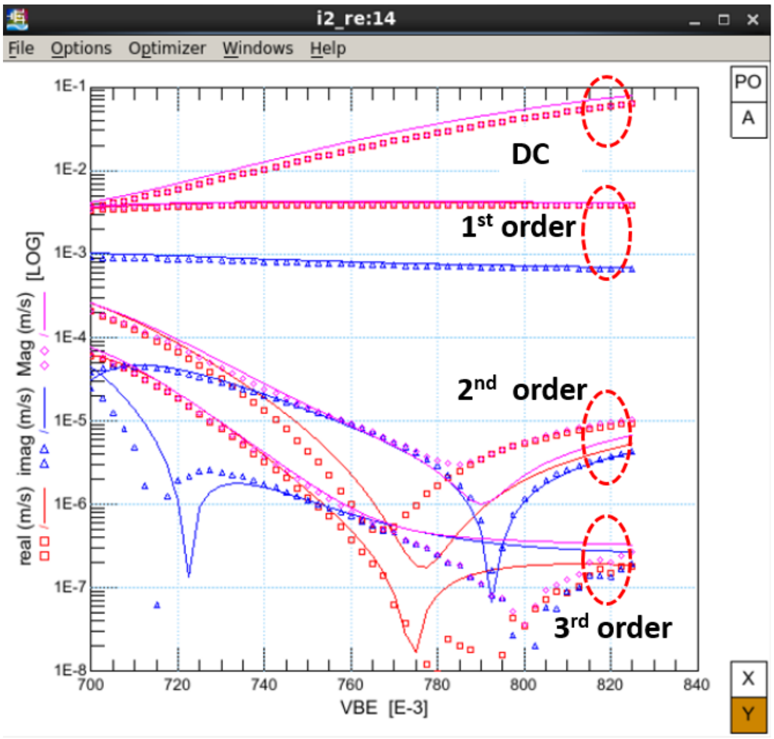

Figure 1.2: Initialization of real, imaginary and magnitude part of i_2 at DC, AC and harmonics for V_{CB} = 3.75 V on common-base SiGe HBT.

1.2 Problems with using MEXTRAM 504.12

The following figures will show the initial status of measured and MEXTRAM 504.12 simulated DC, S-parameters and OIP3 on common-emitter and common-base SiGe HBTs before the start of this PhD project. Initially parameter extraction was improved, in an effort to improve IP3 modeling, this however, is far from sufficient, and it was clear that new model developments are required.

1.2.1 Initial figures in common-emitter SiGe HBT

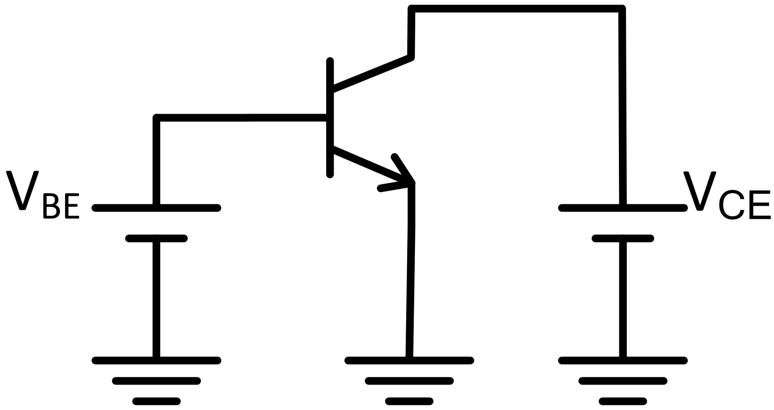

Figure 1.3: A schematic of DC measurement for input V_{BE} and V_{CE}.

Fig. 1.3 shows DC measurement for input biases of V_{BE} and V_{CE}. The cable and probe resistances are not shown.

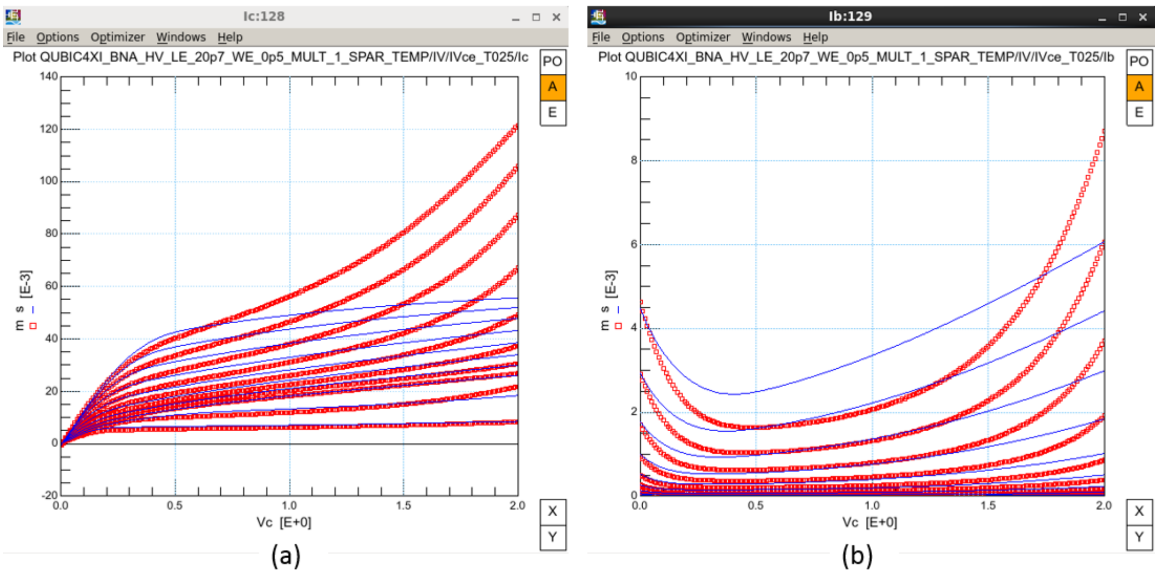

Figure 1.4: Output curves for measured and MEXTRAM 504.12 simulated (a) I_C-V_{CE} and (b) I_B-V_{CE} at V_{BE} from 0.78 to 0.96 V.

Fig. 1.4(a) shows output curves for measured and MEXTRAM 504.12 simulated I_C-V_{CE} at V_{BE} from 0.78 to 0.96 V. For an increasing V_{BE}, the simulated I_C becomes to deviate from measurement at smaller V_{CE}, which implies the parameters about temperature scaling are not well extracted. Fig. 1.4(b) shows output curves for measured and MEXTRAM 504.12 simulated I_B-V_{CE} at V_{BE} from 0.78 to 0.96 V. I_B-V_{CE} cannot be fitted well at high V_{BE}, which may be related to parameters about temperature scaling and resistance.

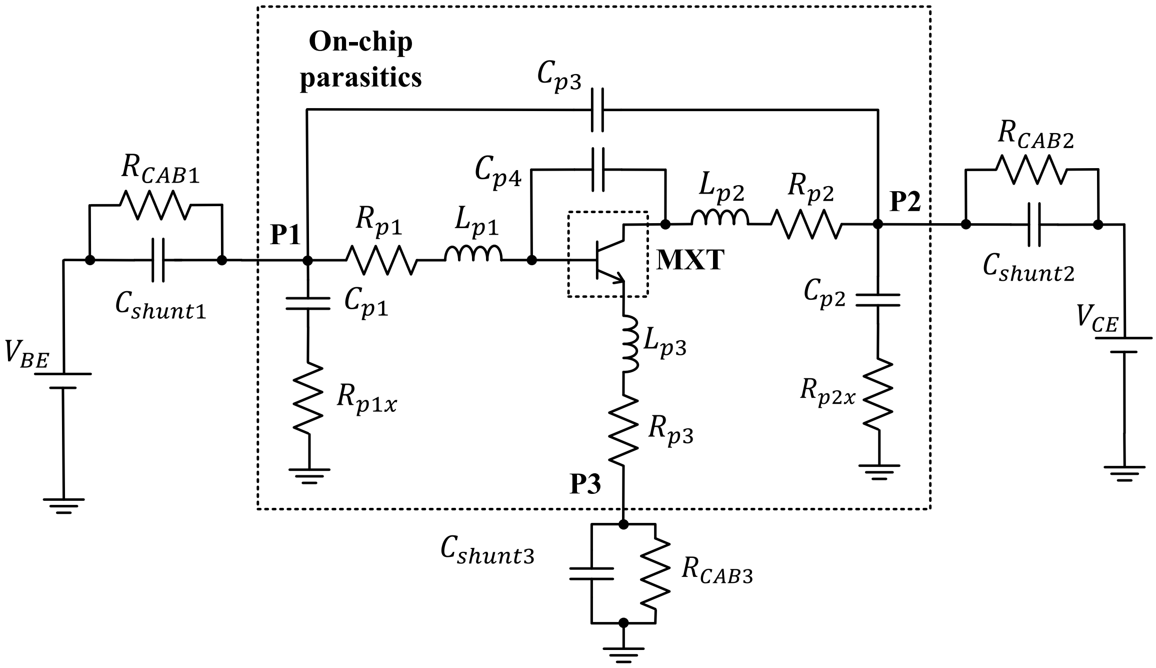

Figure 1.5: A schematic of S-parameter measurement for sweeping V_{BE} at fixed V_{CE} = 1.5 V.

Fig. 1.5 shows a schematic of S-parameter measurement for sweeping V_{BE} at fixed V_{CE} = 1.5 V. R_{CAB1}, R_{CAB2} and R_{CAB3} are cable resistances. C_{p1}, C_{p2}, C_{p3} and C_{p4}, are pad capacitances. R_{p1}, R_{p2}, R_{p3}, R_{p1x} and R_{p2x}, are series resistances. L_{p1}, L_{p2} and L_{p3} are series inductances of interconnects. C_{shunt1}, C_{shunt2} and C_{shunt3} are added to calibrate simulated RF loss compared to measurement. The frequency ranges from 0.1 to 45 GHz. All parasitics are removed using standard open short de-embedding at each frequency.

Fig. 1.6(a) shows initial status of C_{BC}-V_{BE} at V_{CE} = 1.5 V. C_{BC} is extracted from imaginary part of Y_{12}, $\Im(Y_{12})$, using $C_{BC} = -\Im(Y_{12})/\omega$. ω is angular frequency. A clear kink in measured C_{BC} can be clear seen around V_{BE} = 0.82 V, which is not captured by simulation. Fig. 1.6(b) shows initial status of f_T-V_{BE} at V_{CE} = 1.5 V. The peak f_T at V_{BE} = 0.8 V can be fitted well at this bias. So the kink observed on C_{BC} in Fig. 1.6(a) is related to high injection effect.

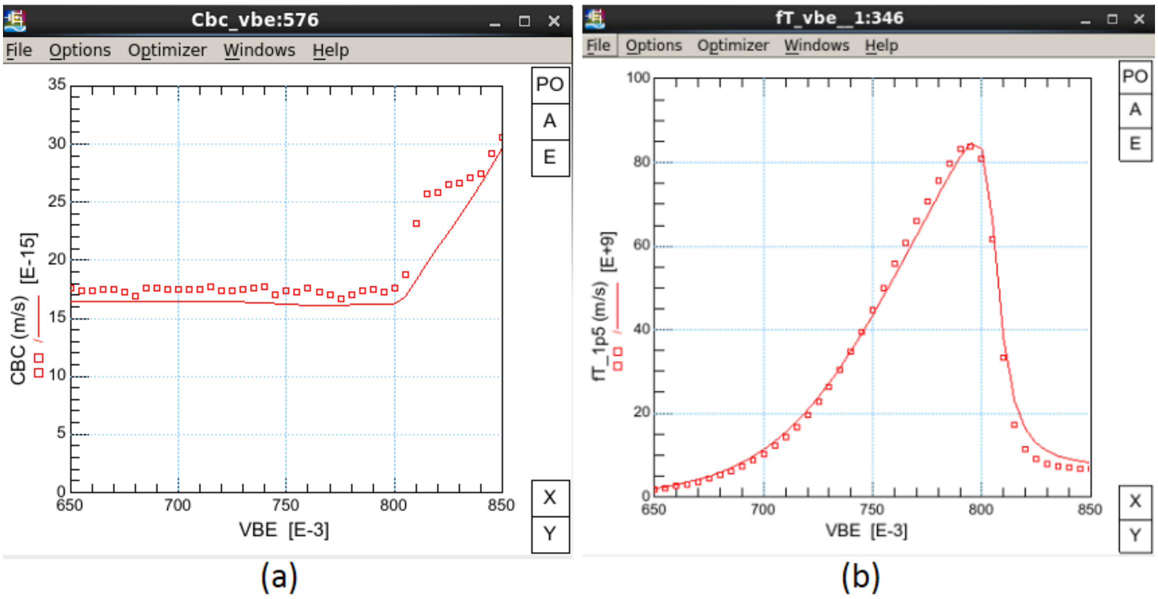

Figure 1.6: Initial status of (a) C_{BC}-V_{BE} and (b) f_T-V_{BE} at V_{CE} = 1.5 V.

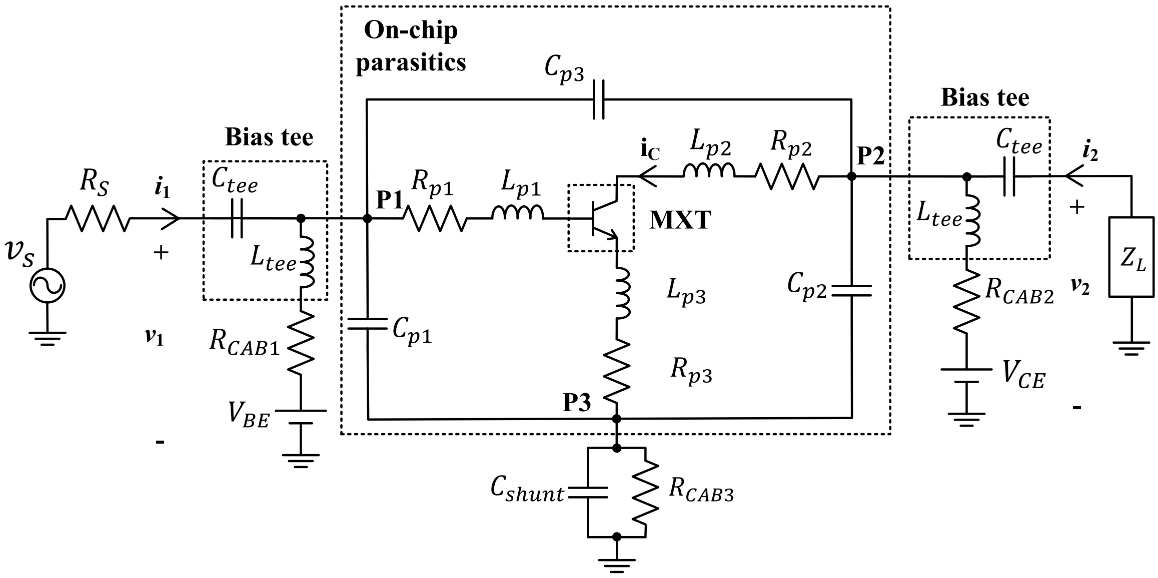

Figure 1.7: Circuit schematic for simulation of IP3.

Fig. 1.7 shows the circuit schematic used for IP3 simulation. V_{BE} and V_{CE} are DC base and collector biases. The bias tees are used to couple RF and DC signals. R_{CAB1}, R_{CAB2} and R_{CAB3} are cable resistances measured by probing an impedance standard substrate (ISS) short structure. The on-chip pad and interconnect parasitics are modeled by C_{p1}, C_{p2}, C_{p3}, R_{p1}, R_{p2}, R_{p3}, L_{p1}, L_{p2}, L_{p3}, which are extracted from S-parameters of OPEN and SHORT structures. C_{shunt} is placed in parallel with R_{CAB3} to shunt RF signal in simulation, and does not correspond to a physical capacitance. In measurements, RF losses on cable are already accounted for through calibration. L_{tee} blocks RF signal, and thus no shunt capacitance is needed for R_{CAB1} and R_{CAB2}. The source voltage is $v_s(t) = A\cos(2\pi f_0)$ with A being amplitude, f_0 being fundamental frequency. f_0 = 2 GHz. The source resistance R_s = 48.82 Ω. Z_L is load impedance and its value is measured at all frequencies. At f_0, Z_L = 300.14 + j0.37 Ω. Complex AC currents i_1, i_2, and voltages v_1, v_2 at f_0 , $2f_0$ and $3f_0$ are obtained from measured X-parameters. i_2 is approximately equal to collector current i_C from 2 to 6 GHz according to simulation. First and third harmonic output powers are calculated as

$$P_{out}(f_0) = \frac{1}{2}\Re(v_2(f_0) \times i_2^*(f_0)), \tag{1.4}$$

$$P_{out3}(3f_0) = \frac{1}{2}\Re(v_2(3f_0) \times i_2^*(3f_0)). \tag{1.5}$$

where "$\Re$" stands for real part, "*" denotes conjugate. OIP3 in dBm is calculated as

$$\text{OIP3}|_{\text{dBm}} = 10\log_{10}\left(\frac{P^3_{out}(f_0)}{P_{out}(3f_0)}\right) + 30 \text{ dBm}. \tag{1.6}$$

(1.6) assumes that the slopes of P_{out} (dBm) at f_0 and $3f_0$ versus available source power P_{avs} (dBm) are 1:1 and 3:1, respectively. $P_{avs} = A^2/8R_s$ [4] is set to -30 dBm to ensure these assumptions are satisfied. Fig. 1.8 shows initial status of OIP3-V_{BE} at V_{CE} = 1.5 V on a common-emitter SiGe HBT using MEXTRAM 504.12. Compared to the measured OIP3, the simulated OIP3 is overestimated in the linear part from 0.65 to 0.73 V and also clearly underestimated around its peak from 0.73 to 0.78V. For common-emitter OIP3 issues, we also know

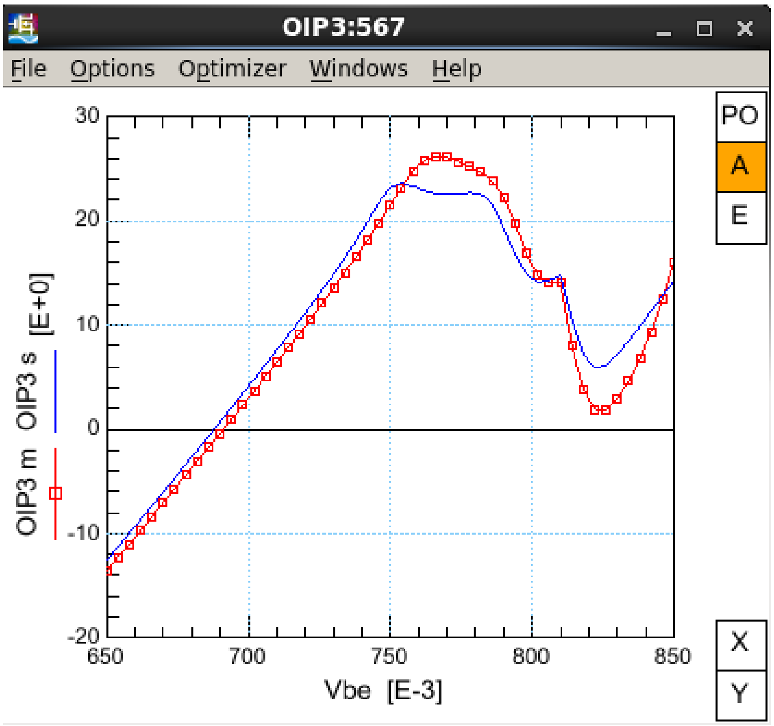

Figure 1.8: Initial status of OIP3-V_{BE} at V_{CE} = 1.5 V on a common-emitter SiGe HBT.

from NXP that CB depletion capacitance model has impact, which will be further investigated below.

1.2.2 Initial figures in common-base SiGe HBT

The DC, S-parameters and X-parameters schematics on common-base SiGe HBT are very similar to the ones shown in common-emitter SiGe HBT. So the following will directly show the initial status of simulations using MEXTRAM 504.12 compared to measurement.

Fig. 1.9 shows initial status of I_C-V_{BE} and I_B-V_{BE} at V_{CB} = 0 V. I_B is calculated from measured I_C and I_E, which results in noisy I_B at medium range. Although measured I_C is well fitted, the simulated I_B at high V_{BE} larger than 0.8 V is much larger than measurement because high injection effect and R_E are not well extracted.

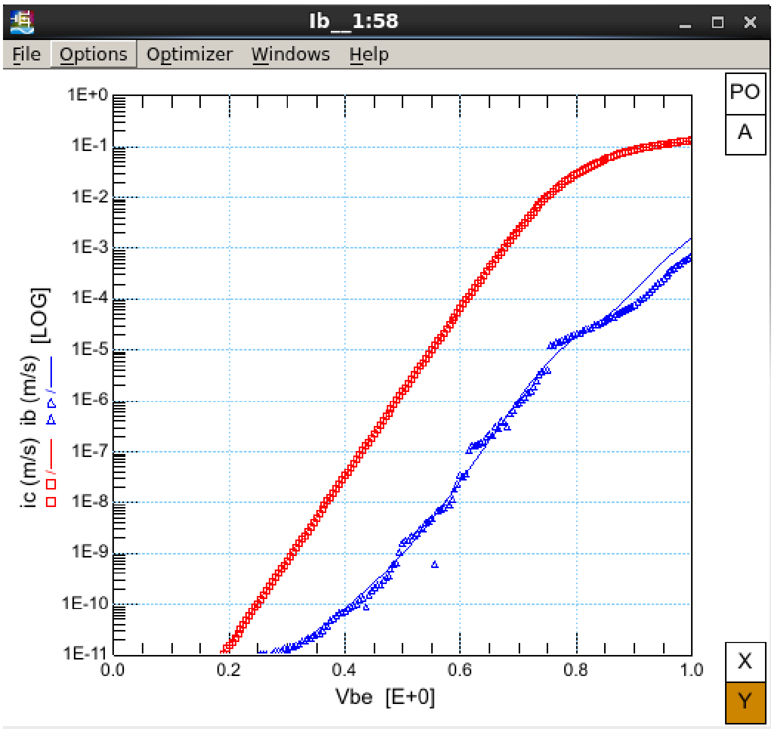

Figure 1.9: Initial status of I_C-V_{BE} and I_B-V_{BE} at V_{CB} = 0 V for common-base SiGe HBT on RF structure.

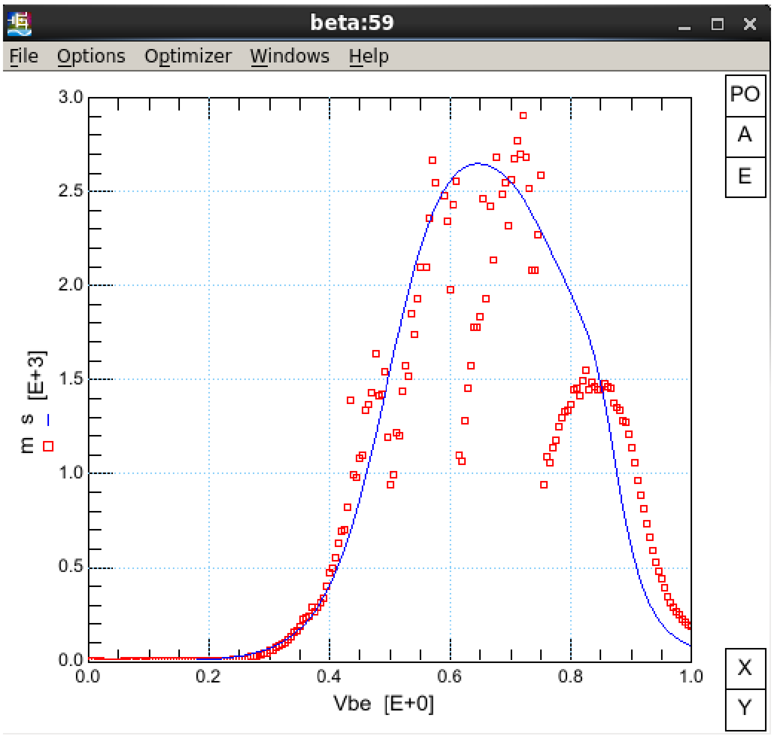

Figure 1.10: Initial status of β-V_{BE} at V_{CB} = 0 V for common-base SiGe HBT.

Fig. 1.10 shows initial status of β-V_{BE} at V_{CB} = 0 V for common-base SiGe HBT. β is calculated from I_C and I_B. $\beta = I_C/I_B$. The noisy β is due to noisy I_B obtained on RF structure. Due to an overestimated I_B seen in Fig. 1.9 at high V_{BE}, an estimated β in simulation can be clearly seen at V_{BE} larger than 0.8 V. From calculated β, the peak β can reach above 2500 and β can keep around 1000 even when high injection occurs around V_{BE} = 0.8 V. Such high β means that I_B can easily be negative when V_{CB} increases, especially considering the bias condition of OIP3 of interest in both Fig. 1.14 and Fig. 1.15.

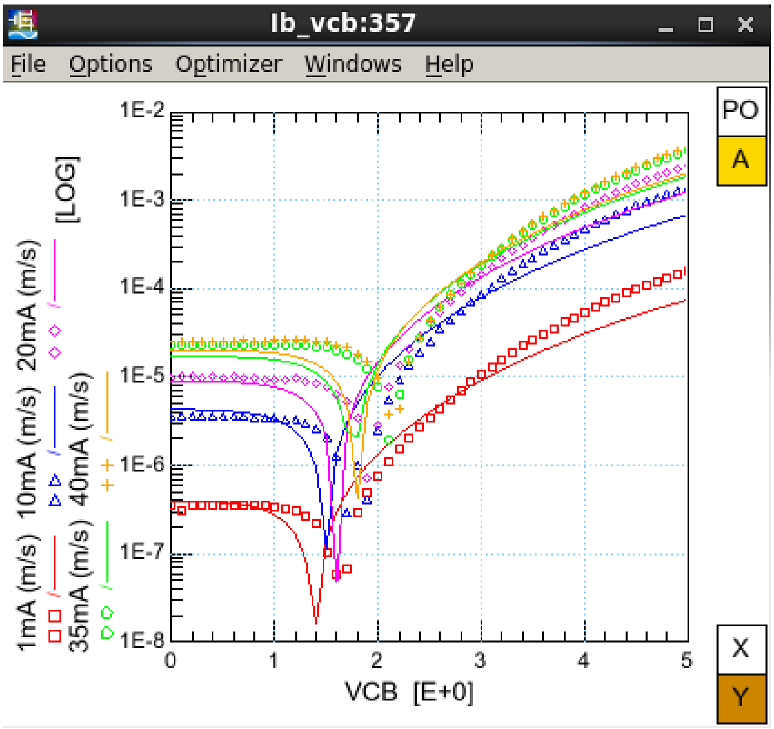

Figure 1.11: Initial status of I_B-V_{CB} at I_E up to 40 mA for common-base SiGe HBT.

Fig. 1.11 shows initial status of I_B-V_{CB} at I_E up to 40 mA. I_B can be approximately calculated from β and M-1 as

$$I_B \approx I_C \cdot (\frac{1}{\beta} - (M-1)). \tag{1.7}$$

A large difference observed on I_B-I_E is due to poor fitting of V_{CB} and I_E dependence of avalanche current. The sharp dips denote the V_{CB} where the sign of I_B changes from positive to negative because holes of avalanche effect flowing into base becomes larger than holes that flowing into base. At higher I_E, the V_{CB} where the sign of measured I_B changes becomes larger. It is because β in Fig. 1.10 decreases at $V_{BE} > 0.6$ V, then avalanche should be larger at high V_{CB} to make I_B negative.

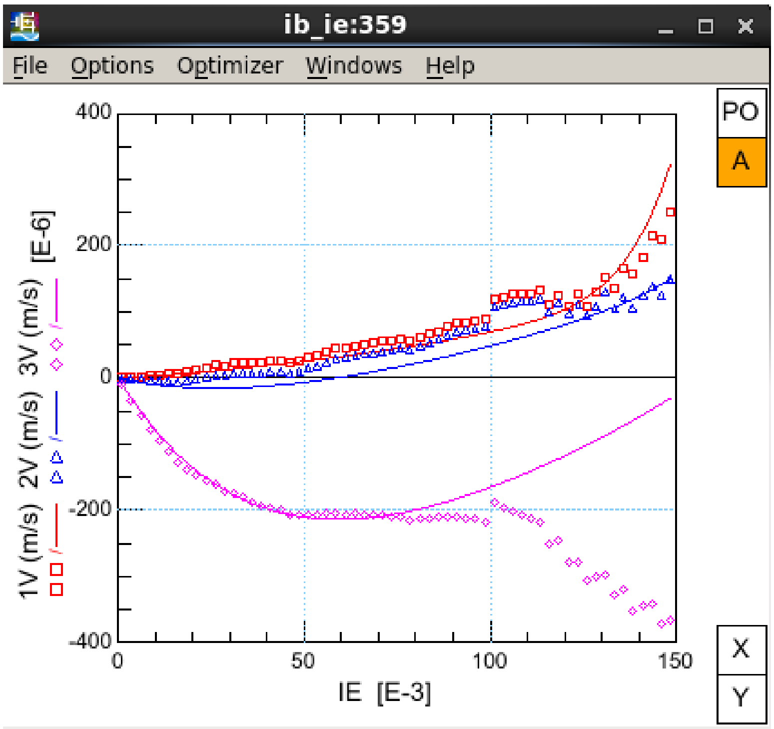

Figure 1.12: Initial status of I_B-I_E up to 150 mA at V_{CB} from 1 to 3 V for common-base SiGe HBT.

Fig. 1.12 shows initial status of I_B-I_E up to 150 mA at V_{CB} from 1 to 3 V. As I_E increases from 1 to 50 mA, both β and (M-1) become lower, which makes I_B slowly decrease with increasing I_E. At I_E between 50 to 100 mA, I_B becomes almost constant because $1/\beta$ becomes compared to M-1. At I_E larger than 100 mA, I_B clearly decreases because M-1 increases with increasing I_E as Kirk effect occurs.

Fig. 1.13 shows initial status of f_T-I_E at V_{CB} from 1 to 3 V. The front part and peak of f_T are not fitted well due to bias dependence of depletion and diffusion base-emitter and base-collector capacitances. The bad fitting of f_T at high I_E is due to self-heating and high injection effect that may not be well considered.

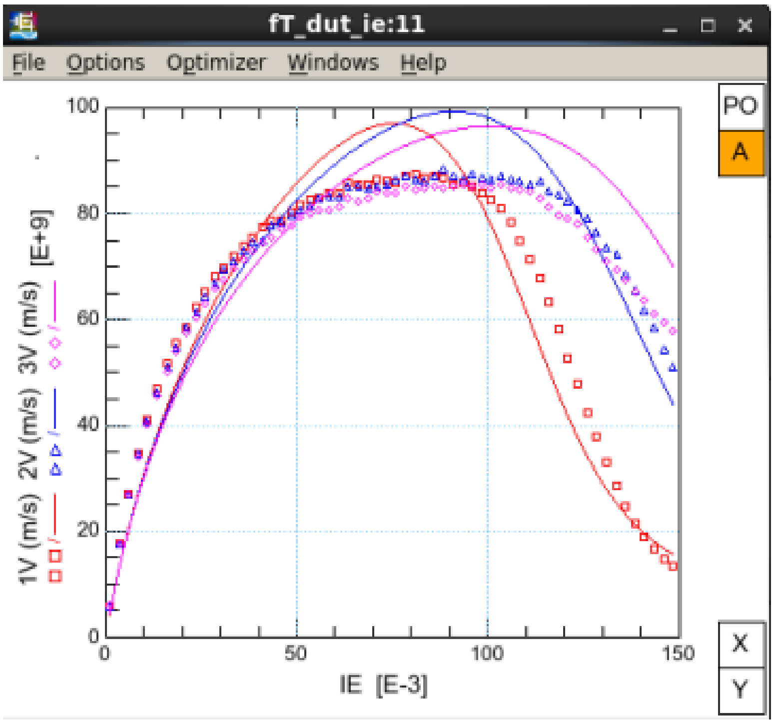

Figure 1.13: Initial status of f_T-I_E at V_{CB} from 1 to 3 V for common-base SiGe HBT.

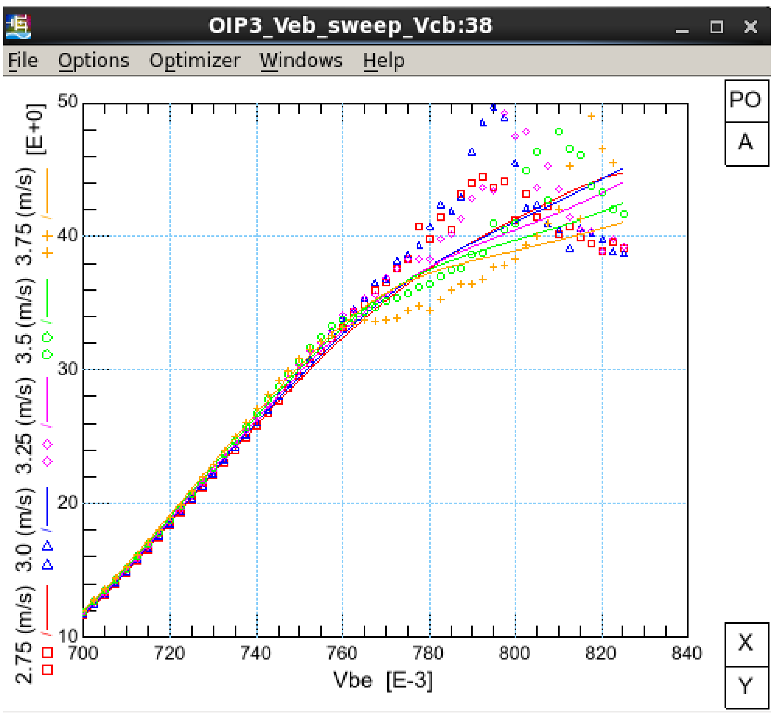

Figure 1.14: Initial status of OIP3-V_{BE} at multiple V_{CB} on a common-base SiGe HBT.

Fig. 1.14 shows initial status of OIP3-V_{BE} at multiple V_{CB} on a common-base SiGe HBT. Compared to the measured OIP3, the simulated OIP3 at $V_{BE} > 0.76$ V is way off and peaks at each V_{CB} are not well captured. On prior studies, an accurate modeling of I-V and C-V characteristics is important for distortion analysis. The avalanche model and CB depletion capacitance are two dominant nonlinearities to determine IP3 modeling [12] [13] [14].

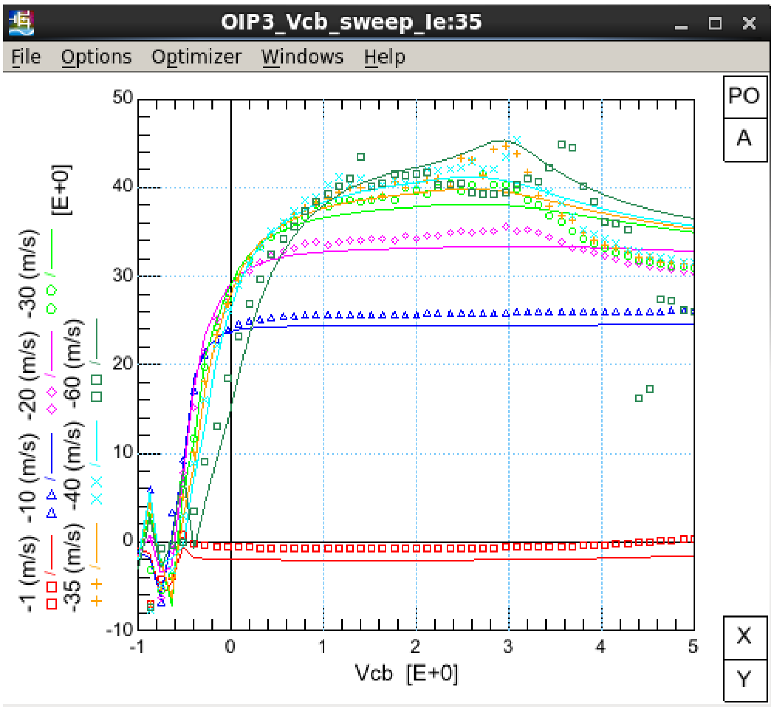

Figure 1.15: Initial status of OIP3-V_{CB} at multiple I_E on a common-base SiGe HBT.

Fig. 1.15 shows initial status of OIP3-V_{CB} at multiple I_E on a common-base SiGe HBT. Compared to the measurement, the simulated OIP3-V_{CB} shows a clear difference at each I_E. Also, the measured peak OIP3 at I_E higher than 20 mA cannot be obtained in simulation.

Clear improvements on both V_{BE} and V_{CB} dependence of common-emitter and common-base OIP3 as well as their DC, AC characteristics have been achieved in this dissertation. The following figures will show them separately.

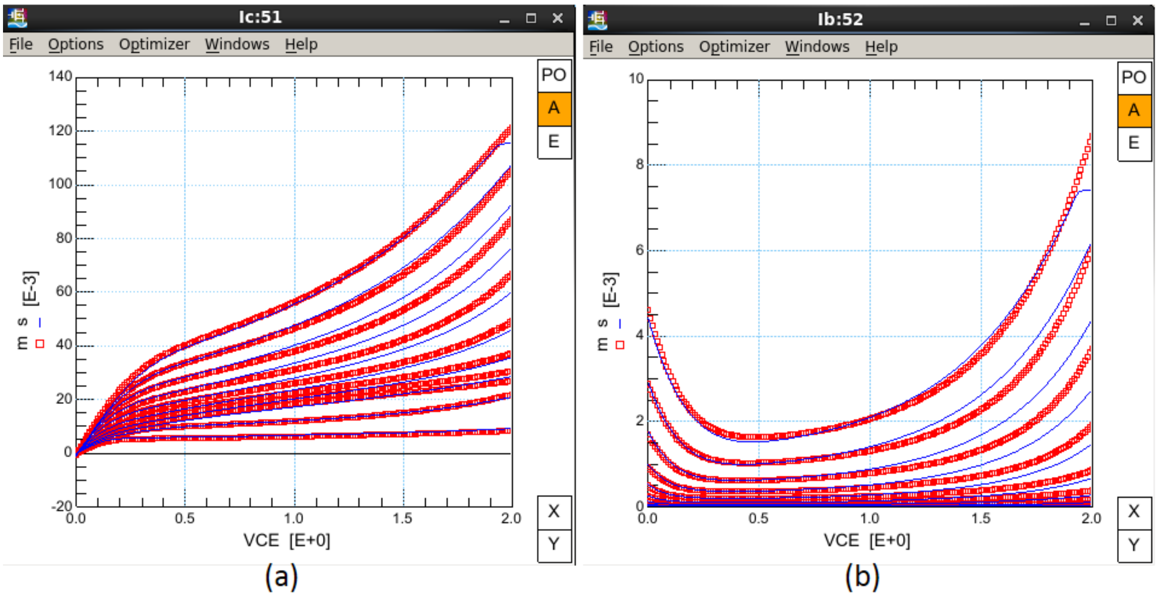

Figure 1.16: Improved output curves of (a) I_C-V_{CE} and (b) I_B-V_{CE} at V_{BE} from 0.78 to 0.96 V on common-emitter SiGe HBT.

For common-emitter SiGe HBT, Fig. 1.16(a) shows improved output curves of I_C-V_{CE}. A clear improvement is achieved at high current by improving temperature dependence of V_{DC}. Fig. 1.16(b) shows improved output curves of I_B-V_{CE}. An overall good fitting is due to reasonable extraction of R_E and its temperature coefficient A_E.

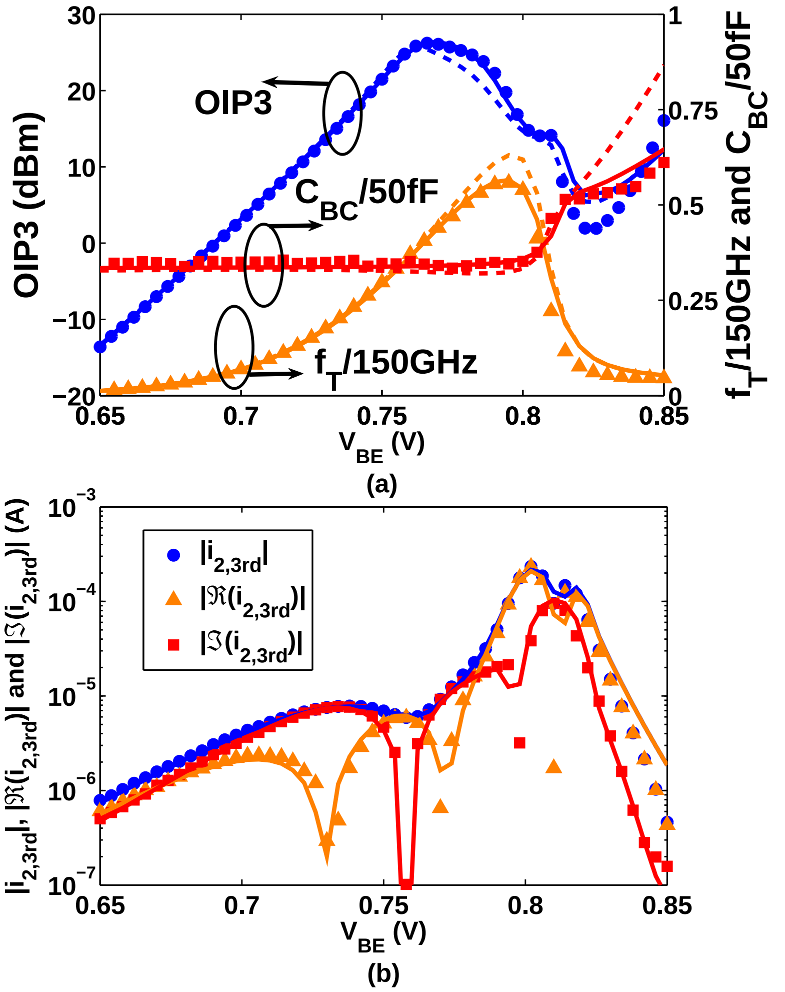

Figure 1.17: Improved V_{BE} dependence of OIP3, C_{BC} and f_T at V_{CB} = 1.5 V on common-emitter SiGe HBT.

Fig. 1.17(a) shows improved V_{BE} dependence of OIP3, C_{BC} and f_T at V_{CB} = 1.5 V. The linear part of OIP3 at low V_{BE} and peak OIP3 can be well modeled. At high V_{BE}, peak f_T and a kink of C_{BC} can be well captured and fitted. Fig. 1.17(b) shows improved V_{BE} dependence of real, imaginary and magnitude parts of $i_{2,3rd}$. Both real and imaginary parts of $i_{2,3rd}$ can be well modeled, which result in a good fitting of $i_{2,3rd}$ and finally improved OIP3 modeling.

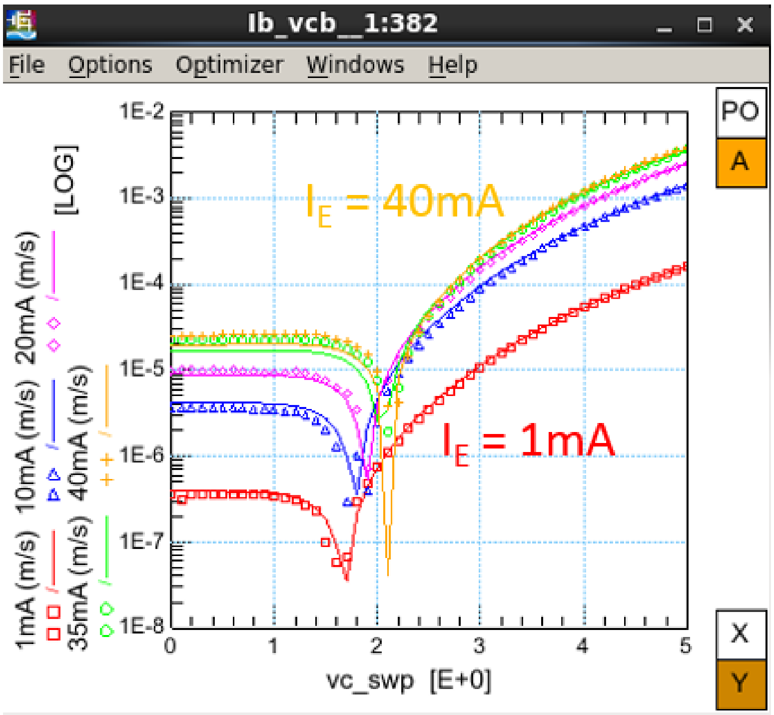

Figure 1.18: Improved I_B-V_{CB} at I_E from 1 to 40 mA on common-base SiGe HBT.

For common-base SiGe HBT, Fig. 1.18 shows improved I_B-V_{CB} at I_E from 1 to 40 mA. With V_{CB} and I_E dependence of M-1 well fitted, a good fitting of I_B-V_{CB} at each I_E can be obtained.

Fig. 1.19 shows improved I_B-I_E up to 150 mA at V_{CB} from 1 to 3 V. When self-heating and Kirk effect are better considered by incorporating the new extended avalanche model to accurately fit extracted actual M-1 at high current, I_B-I_E from low to high current range can be well fitted.

Fig. 1.20 shows improved f_T-I_E at V_{CB} from 1 to 3 V. The clear improvement is due to bias dependence of base-emitter and base-collector capacitances, self-heating effect, epi-layer model parameters and knee current.

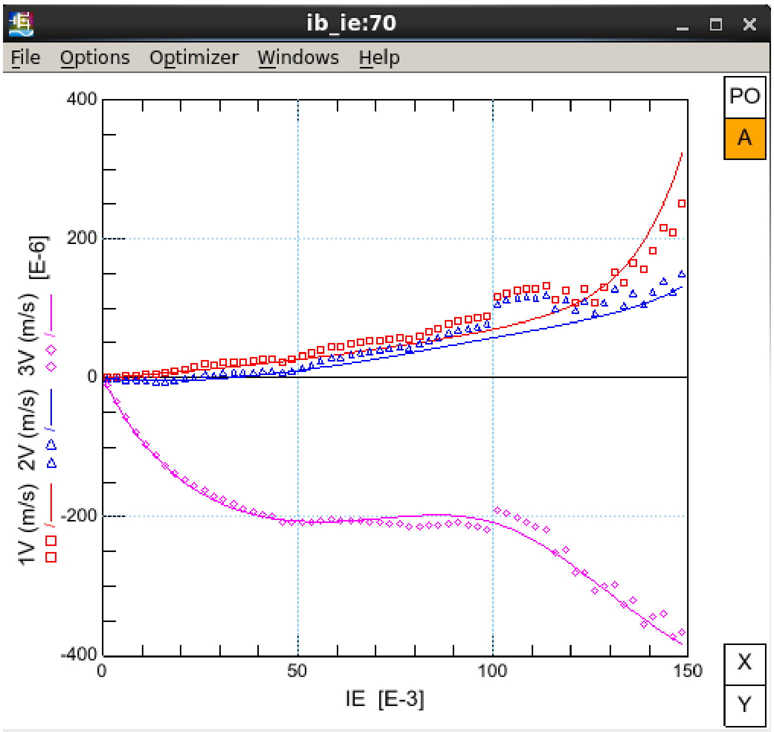

Figure 1.19: Improved I_B-I_E up to 150 mA at V_{CB} from 1 to 3 V on common-base SiGe HBT.

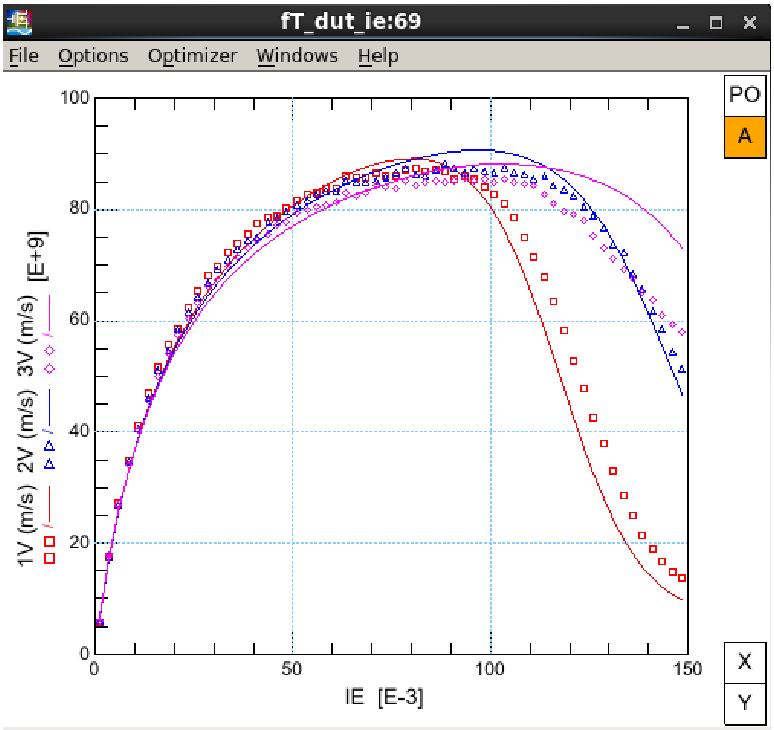

Figure 1.20: Improved f_T-I_E at V_{CB} from 1 to 3 V on common-base SiGe HBT.

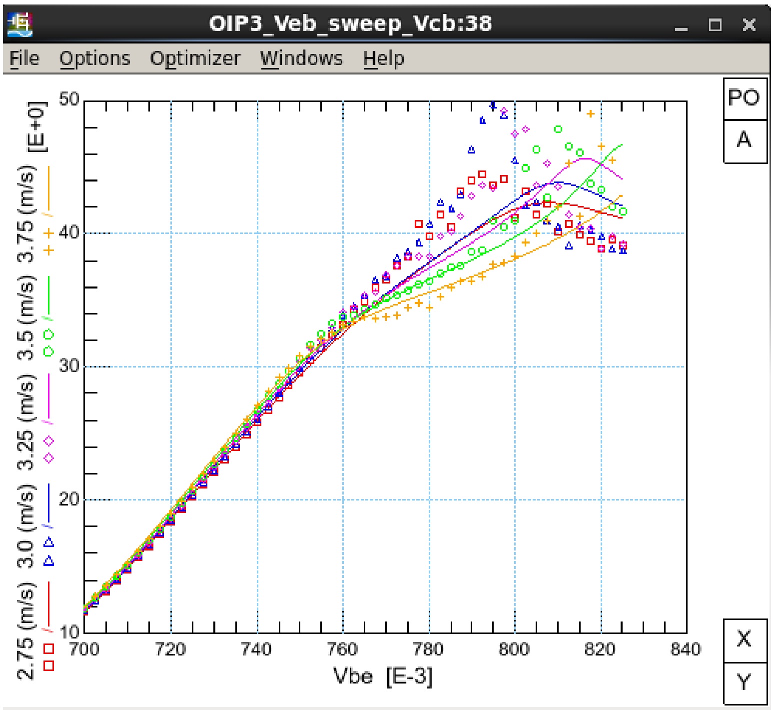

Figure 1.21: Improved OIP3-V_{BE} on common-base SiGe HBT.

Fig. 1.21 shows improved OIP3-V_{BE}. As current dependence of avalanche current has been well modeled, OIP3-V_{BE} is well modeled at low V_{BE} up to 0.76 V. Compared to initial status in Fig. 1.14, OIP3-V_{BE} can be well fitted up to V_{BE} = 0.8 V for V_{CB} = 3.75 V and up to V_{BE} = 0.79 V for V_{CB} = 3.5 V, which is due to improved avalanche model at medium current. For V_{CB} = 2.75, 3 and 3.25 V, OIP3 peaks can be clearly seen but still deviate with measurement. Further improvements on above can be possibly achieved by accurate extraction of source resistance, epi-layer model parameter about high injection effect, which has not verified yet.

Fig. 1.22 shows improved OIP3-V_{CB}. At I_E = 20, 30, 35 and 40 mA, the new extended avalanche model does a good job in capturing the location of the OIP3 peak. The actual values of the IP3 peak are difficult to determine accurately in both simulation and measurements, and of less practical interest than the location of IP3 peak. Compared to the initial status shown in Fig. 1.15, the higher V_{CB} portion of all curves, e.g. $V_{CB} > 3$V, are much better fitted.

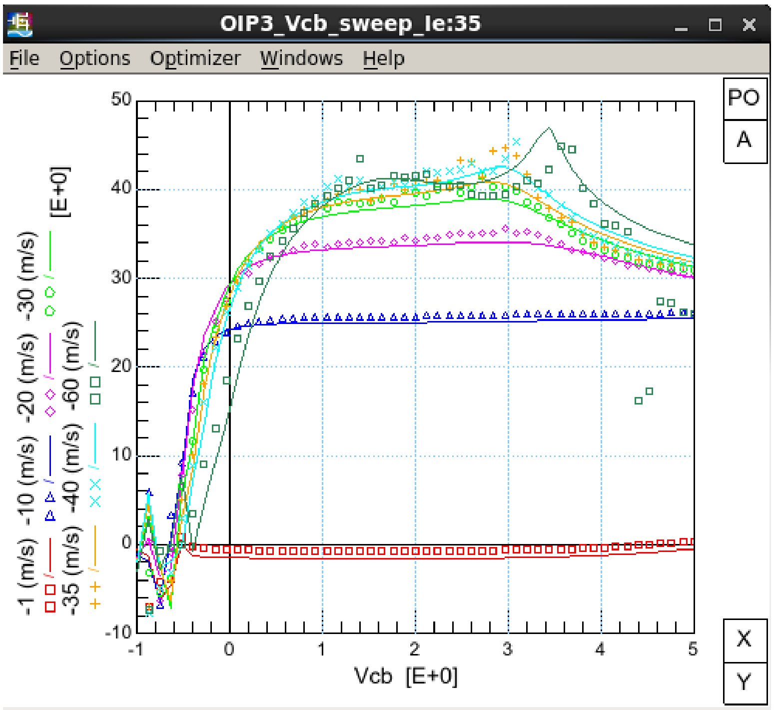

Figure 1.22: Improved OIP3-V_{CB} on common-base SiGe HBT.

1.4 Dissertation Contributions

The following chapters aim to well model IP3 dependence on V_{CB} and I_C for common-emitter and common-base SiGe HBTs. To achieve this goal, various analysis including CB depletion capacitance model, improved avalanche model, Volterra series implementation are provided in each chapter.

Chapter 1 introduces DC, S-parameter and X-parameter measurement used in this dissertation. The simulation setups for each measurement are described. The initial status using MEXTRAM 504.12 for critical characteristics in each measurement are shown for common-emitter and common-base SiGe HBT, respectively. The achievements on each characteristics are presented.

Chapter 2 reviews complete circuit in Mextram 505.00 and new features which are achieved in this dissertation from Mextram 504.12 to Mextram 505.00. The epi-layer model is based on Kull model in reverse mode, but taking Kirk effect and smoothing transition around onset of high injection into consideration in forward mode, which adds complexity in main current

I_N and charges calculated by I_N and leads to inclusion of an effective intrinsic CB junction bias $V^{\star}_{B_2C_2}$. The main current is calculated from $V^{\star}_{B_2C_2}$ and also considers a linearly graded band gap change for HBT. The CB depletion capacitance in MEXTRAM is controlled by a smoothly limiting junction voltage in order to avoid discontinuity around CB built-in potential. The avalanche model in MEXTRAM 505.00 has improved V_{CB} and I_E dependence when compared to the one in MEXTRAM 504 at low current. However, the empirical current dependence in MEXTRAM 505.00 has poor performance at medium current and is impossible to model high injection effect at high current.

Chapter 3 compares the measured and simulated magnitude, real and imaginary part of third order output current ($i_{2,3rd}$) near the IP3 peak for common-emitter SiGe HBT, CB depletion capacitance C_{tC} modeling is identified to be significant for IP3 peak modeling. Two new options of CB depletion capacitance model are then presented to correctly model the bias dependence of peak IP3. Implications of each C_{tC} modeling options on IP3, f_T, C_{BC} are presented.

Chapter 4 shows clear limitations of avalanche model in MEXTRAM 504.12 and MEXTRAM 505 for high current fitting. Based on current dependence of CB depletion capacitance, a new avalanche model is derived at low current. With Kirk effect at high current and a smoothing transition at medium current, a new extended avalanche model is derived. A new M-1 extraction method is also proposed at high current. The performance of new extended avalanche model at high current is verified by a good fitting of V_{CB} and I_C dependence of M-1 up to high injection range in two different sizes of SiGe HBT on DC structures.

Chapter 5 describes the implementation of Volterra series with Mextram to analyse V_{CB} and I_C dependence of IP3 for common-base SiGe HBT. AC and harmonic balance simulations are used as reference to examine the accuracy of implementation results from first to third order output current $I_{2,3rd}$. The contributions from main current and avalanche current are examined to be dominant in $I_{2,3rd}$, thus IP3.

Chapter 6 presents the performance of Mextram 504.12, Mextram 505.00 and the newly developed extended avalanche model in modeling of IP3 dependence on V_{CB} and V_{BE}, respectively. The new extended avalanche model shows an overall good IP3 modeling of V_{CB} dependence at each I_E from 1 to 60 mA.

Chapter 7 draws conclusions.

Chapter 2

Mextram Compact Model

Mextram is an industrial standard compact model for bipolar transistor, which has proven excellent for Si and SiGe processes, including analog, mixed-signal, high speed RF as well as high voltage high power technologies. It accounts for high injection effects with a dedicated epi-layer model, self heating, avalanche, low and high frequency noises in physical manners, and is formulated with minimal interactions between DC and AC characteristics that simplifies parameter extraction [15].

In 2017, Mextram was updated to version 505.00. The following improved models and new parameters as contributions of this dissertation have been included in Mextram 505.00 [1] and will be detailed in following chapters:

- Avalanche current I_{AVL} is calculated from main current I_N as initiating current, and I_{AVL} limitation without M-1<1 are also updated accordingly.
- A new avalanche model is added with A_{AVL}, B_{AVL}, C_{AVL}, V_{DCAVL}, T_{BAVL} as model parameters and used as default.
- I_{TOavl} is added as a model parameter to empirically model current dependence of M-1.
- SWVJUNC, a switch for calculation of the CB junction voltage for controlling depletion charge, V_{junc}, is added. If SWVJUNC = 0 (default), then V_{junc} = $V_{B_2C_2}$. If SWVJUNC = 1, then V_{junc} = $V_{B_2C_1}$. If SWVJUNC = 2, then V_{junc} = $V_{B_2C_1}$ + V_{xi0}, where V_{xi0} is epi-layer voltage drop assuming that epi-layer resistance is at its injection width x_i = 0 value when quasi-saturation starts [1].

- SWVCHC, a switch for transition voltage width V_{ch}, is added. If SWVCHC = 0 (default), then V_{ch} = $0.1V_{dCT}$, where V_{dCT} is CB built-in potential with temperature scaling. If SWVCHC = 1, then V_{ch} = $V_{dCT}(0.1 + 2\frac{I_{C_1C_2}}{I_{C_1C_2}+I_{qs}})$, where $I_{C_1C_2}$ is epi-layer current and I_{qs} is quasi-saturation onset current [1].

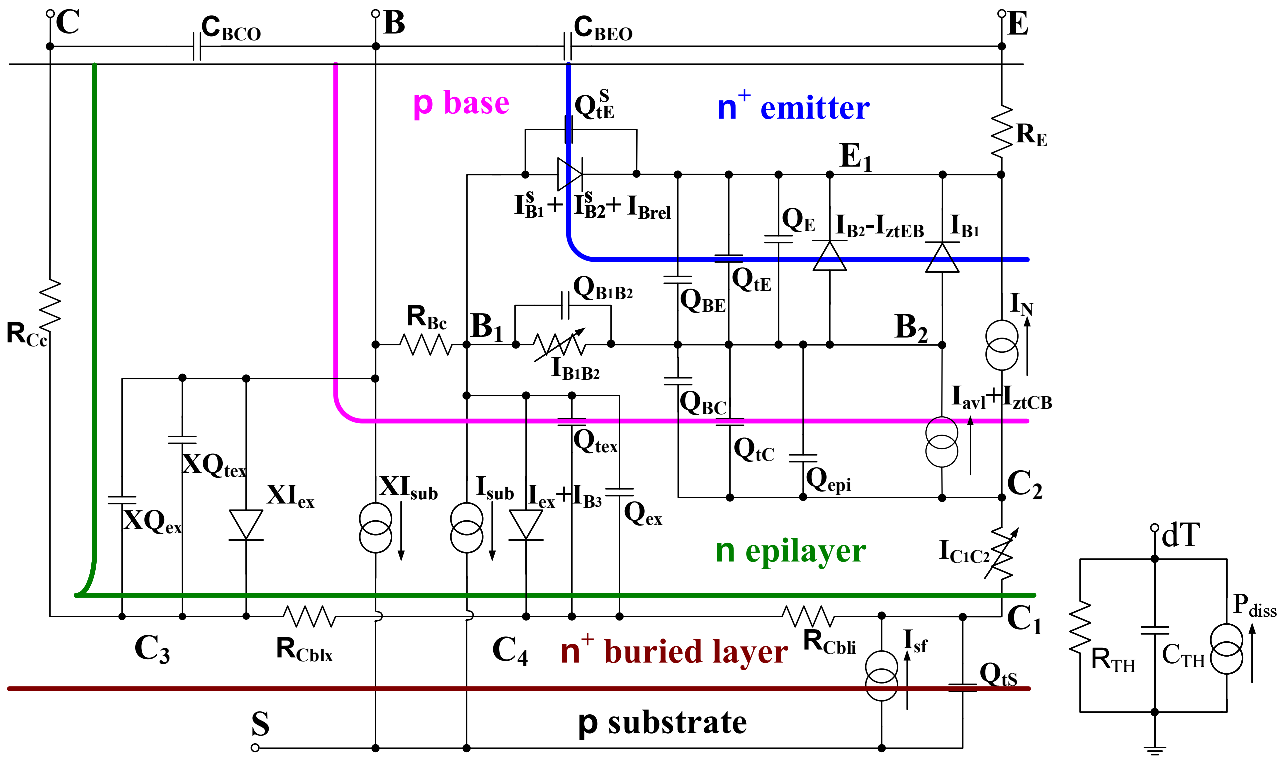

Figure 2.1: The complete equivalent circuit for Mextram 505.00 [1].

Fig. 2.1 shows the complete equivalent circuit for Mextram 505.00 [1]. C, C_1, C_2, C_3, C_4, B, B_1, B_2, E, E_1, S are circuit nodes. The components between C_2, B_2 and E_1 model the intrinsic NPN transistor. The side-wall components are placed between B_1 and E_1. The parasitic PNP transistor is formed by the extrinsic p-base of the NPN, which acts as emitter of the PNP, n-collector of the NPN, which acts as base of the PNP, and the p-substrate, which acts as the collector of the PNP. The parasitic PNP can be optionally further partitioned to account for distributive effect by EXMOD = 1 and 2. The intrinsic NPN components shown in Fig. 2.1 contain

- I_N, the main current.

- I_{AVL}, the avalanche current.
- I_{B1} and I_{B2}, the ideal and non-ideal base currents.
- I_{ztCB} and I_{ztEB}, the collector-base and emitter-base tunneling currents.
- Q_{tC}, Q_{BC} and Q_{epi}, the intrinsic base-collector depletion charge, base-collector diffusion charge and epi-layer diffusion charge, respectively.
- Q_{tE}, Q_{BE} and Q_E, the intrinsic base-emitter depletion charge, base-emitter diffusion charge and emitter diffusion charge, respectively.

The extrinsic NPN components contain

- $I_{C_1C_2}$, the epi-layer current.
- $I_{B_1B_2}$, the variable base resistance for current crowding effect.
- $Q_{B_1B_2}$, the charge for current crowding effect.

The side-wall components contain

- I_{B1}^S and I_{B2}^S, the side-wall ideal and non-ideal base currents.
- I_{Brel}, the base reliability current.
- Q_{tE}^S, the side-wall base-emitter depletion charge.
- R_{Cblx}, R_{Cbli}, the intrinsic and extrinsic resistances in collector buried layer.

The PNP parasitic components contain

- I_{ex}, the extrinsic reverse base current between B_1 and C_4.
- I_{B3}, the non-ideal reverse base current.
- Q_{tex} and Q_{ex}, the extrinsic base-collector depletion and diffusion charges between B_1 and C_4.
- I_{sub}, the substrate current between B_1 and S.

- XI_{ex}, the extrinsic reverse base current between B and C_3.
- XQ_{tex} and XQ_{ex}, the extrinsic base-collector depletion and diffusion charges between B and C_3.
- XI_{sub}, the substrate current between B and S.
- Q_{tS}, the substrate-collector depletion charge.
- I_{Sf}, the substrate failure current when substrate-collector is in forward bias.

The parasitic resistance and capacitance contain

- R_{CC}, R_{BC}, R_E, the constant collector, base and emitter resistances, respectively.
- C_{BCO}, C_{BEO}, the base-collector and base-emitter overlay capacitances.

It should be noted that $I_{C_1C_2}$ is calculated from $V_{B_2C_1}$ and $V_{B_2C_2}$ using the Kull model [16]. I_N, unlike in Gummel-Poon model [17] or VBIC [18] where it is calculated from $V_{B_2E_1}$ and $V_{B_2C_2}$, is calculated from $V^{\star}_{B_2C_2}$ and $V_{B_2E_1}$, $V^{\star}_{B_2C_2}$ is an effective intrinsic CB junction bias calculated from $I_{C_1C_2}$ and $V_{B_2C_1}$, and used for I_N. The control voltage for Q_{tC} is not simply $V_{B_2C_2}$ due to epi-layer complexity, although Q_{tC} is placed between B_2 and C_2.

In circuit simulators, the node voltages are given to calculate the currents and charges, so current and charge as a function of voltages are written in compact model, like the epi-layer current $I_{C_1C_2}$ as a function of $V_{B_2C_1}$ and $V_{B_2E_1}$ given by the Kull model [16]. However, it is not always the case that an explicit function can be expressed from voltages to calculate currents, as Kull model has no flexibility in ohmic quasi-saturation and fails to take velocity saturation in space charge region into consideration [19]. In MEXTRAM improved epi-layer model, $I_{C_1C_2}$ cannot be expressed as a function of $V_{B_2C_1}$ and $V_{B_2C_2}$. Instead, the epi-layer current $I_{C_1C_2}$ as a current sensor is calculated from $V_{B_2C_1}$ and $V_{B_2C_2}$. An internal voltage $V^{\star}_{B_2C_2}$ is then calculated from $I_{C_1C_2}$ and $V_{B_2C_1}$ with high injection effect in epi-layer well considered. The $V^{\star}_{B_2C_2}$ and $V_{B_2E_1}$ are finally used to calculate other quantities, like I_N and base charge.

2.1 The Epi-layer Model

As stated above, $I_{C_1C_2}$ should be first calculated from $V_{B_2C_1}$ and $V_{B_2C_2}$ as a current sensor for $V^{\star}_{B_2C_2}$ calculation using Kull model [16]. The current through the epi-layer $I_{C_1C_2}$ is given by

$$K_0 = \sqrt{1 + 4\, e^{(V_{B_2C_2} - V_{dC})/V_T}}, \tag{2.1}$$

where V_T=kT/q is thermal voltage, k is Boltzmann constant, T is absolute temperature and q is elementary charge.

$$K_W = \sqrt{1 + 4\, e^{(V_{B_2C_1} - V_{dC})/V_T}}, \tag{2.2}$$

$$p_W = \frac{2\, e^{(V_{B_2C_1} - V_{dC})/V_T}}{1 + K_W}, \tag{2.3}$$

where p_W is the normalized hole charge density to the doping level at the interface with buried layer.

$$E_c = V_T \left[K_0 - K_W - \ln\left(\frac{K_0 + 1}{K_W + 1}\right)\right], \tag{2.4}$$

$$I_{C_1C_2} = \frac{E_c + V_{C_1C_2}}{R_{CV}}, \tag{2.5}$$

where $V_{C_1C_2}$ = $V_{B_2C_2}$- $V_{B_2C_1}$. In reverse mode the node voltage difference $V_{B_2C_2}$ is the quantity that we use in further calculations. In forward mode, Kull model has an abrupt onset of injection and Kirk effect that carrier travels with velocity saturation in space charge region is not considered in Kull model. So we will instead calculate $V^{\star}_{B_2C_2}$ that is to be used in subsequent calculations. It has smoother properties than $V_{B_2C_2}$ itself. For the rest of the quantities in the epi-layer model a distinction must be made between forward and reverse mode [1].

In forward mode that $I_{C_1C_2} > 0$, the voltage drop over epi-layer and epi-layer current at which quasi-saturation or Kirk effect starts are given by

$$V_{qs}^{th} = V_{dC} + 2\, V_T \ln\left(\frac{I_{C_1C_2} R_{CV}}{2V_T} + 1\right) - V_{B_2C_1}, \tag{2.6}$$

where V_{qs}^{th} is the voltage drop over epi-layer at onset of injection, which is calculated to keep $x_i/W_{epi} \to 1$ and $p_0^\star \gg 1$ when going into hard saturation at high currents [1].

$$V_{qs} = \frac{1}{2}\left(V_{qs}^{th} + \sqrt{(V_{qs}^{th})^2 + 4\,(0.1\,V_{dC})^2}\right), \tag{2.7}$$

V_{qs} is limitation on V_{qs}^{th} to be positive.

$$I_{qs} = \frac{V_{qs}}{SCR_{Cv}}\,\frac{V_{qs} + I_{hc}SCR_{Cv}}{V_{qs} + I_{hc}R_{CV}}, \tag{2.8}$$

where SCR_{CV} is space charge resistance. I_{hc} is hot carrier current. From this we calculate α, the ratio of $I_{C_1C_2}$ over I_{qs} [1]

$$\alpha = \frac{1 + a_{x_i}\;\ln\{1 + \exp[(I_{C_1C_2}/I_{qs} - 1)/a_{x_i}]\}}{1 + a_{x_i}\;\ln\{1 + \exp[-1/a_{x_i}]\}}. \tag{2.9}$$

Kull model has an abrupt transition into quasi-saturation. Instead, α is brought in to create a smooth and adjustable transition determined by smoothing parameter a_{x_i}. We need to solve [1]

$$\alpha\,I_{qs} = \frac{V_{qs}}{SCR_{Cv}\;y_i^2}\,\frac{V_{qs} + SCR_{Cv}I_{hc}\,y_i}{V_{qs} + R_{CV}I_{hc}}, \tag{2.10}$$

which leads to

$$v = \frac{V_{qs}}{I_{hc}SCR_{Cv}}, \tag{2.11}$$

$$y_i = \frac{1 + \sqrt{1 + 4\,\alpha\,v\,(1+v)}}{2\,\alpha\,(1+v)}, \tag{2.12}$$

The injection thickness x_i/W_{epi} is given by [15]

$$\frac{x_i}{W_{epi}} = 1 - \frac{y_i}{1 + p_W y_i}. \tag{2.13}$$

When $I_{epi} \to 0$ and hence $y_i \to 1$, then $x_i/W_{epi} \to p_W/(p_W{+}1)$ is obtained to keep a continuous resistance in forward and reverse bias [1].

The hole density p_0^* normalized by doping level N_{epi} at the base-collector junction is given by [1]

$$g = \frac{I_{C_1C_2}R_{CV}}{2V_T}\,\frac{x_i}{W_{epi}}, \tag{2.14}$$

$$p_0^* = \frac{g-1}{2} + \sqrt{\left(\frac{g-1}{2}\right)^2 + 2g + p_W(p_W + g + 1)}. \tag{2.15}$$

For numerical reasons: when $p_0^* < e^{-40}$ we take $p_0^* \to 0$ [1].

$$e^{V^*_{B_2C_2}/V_T} = p_0^*(p_0^* + 1)\, e^{V_{dC}/V_T}. \tag{2.16}$$

In reverse mode, $I_{C_1C_2} < 0$, the hole density at the base-collector junction is given by [1]

$$p_0^* = \frac{2\, e^{(V_{B_2C_2} - V_{dC})/V_T}}{1 + K_0}, \tag{2.17}$$

$$e^{V^*_{B_2C_2}/V_T} = e^{V_{B_2C_2}/V_T}. \tag{2.18}$$

The injection thickness is [1]

$$\frac{x_i}{W_{epi}} = \frac{E_c}{E_c + V_{B_2C_2} - V_{B_2C_1}}. \tag{2.19}$$

Numerical problems might arise for $I_{C_1C_2} \simeq 0$. When $|V_{C_1C_2}| < 10^{-5}\, V_T$ or $|E_c| < e^{-40}\, V_T\ (K_0 + K_W)$ we approximate [1]

$$p_{\text{av}} = \frac{p_0^* + p_W}{2}, \tag{2.20}$$

$$\frac{x_i}{W_{epi}} = \frac{p_{\text{av}}}{p_{\text{av}} + 1}. \tag{2.21}$$

We illustrate below the key characteristics of MEXTRAM's epi-layer model using the parameters extracted for common-emitter SiGe HBT used in this work. V_{CB} is fixed at 0 V, and V_{BE} is swept from 0 to 1.2 V. The following DC and AC simulation results show that $V^{\star}_{B_2C_2}$ directly determines Q_{BC} and Q_{epi} at high current.

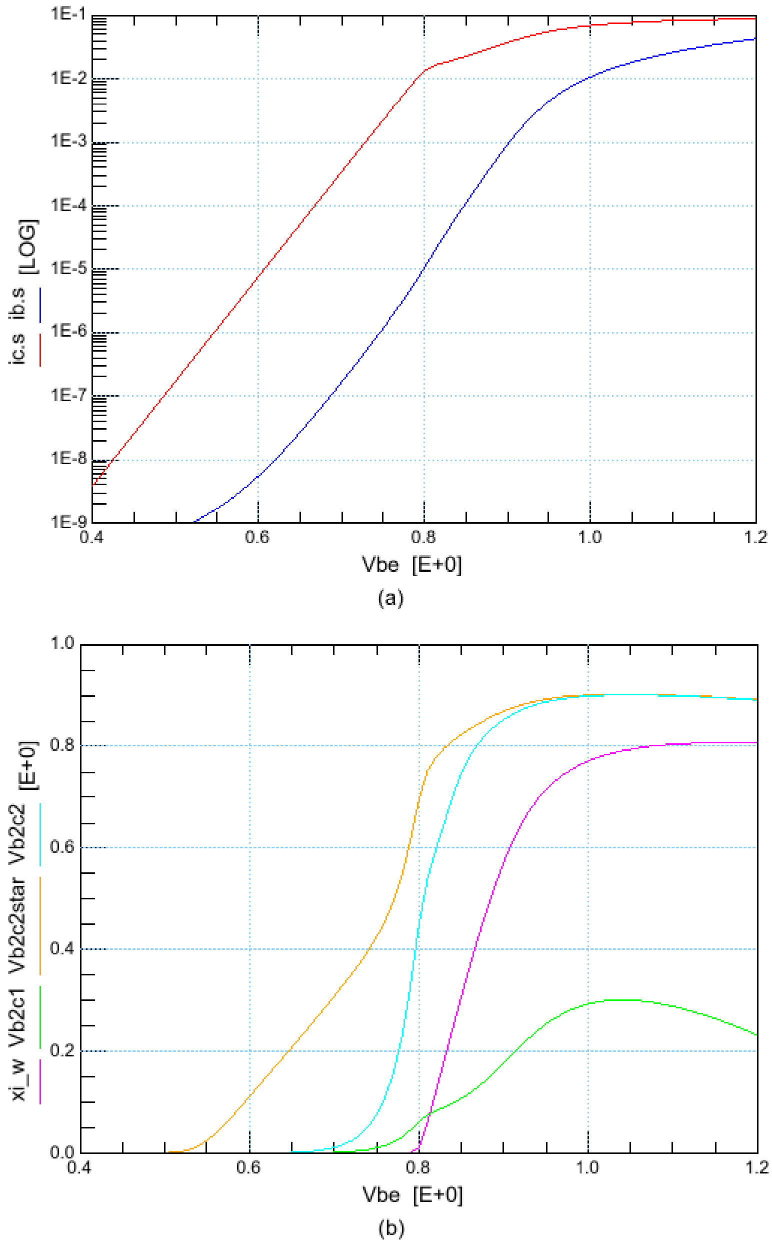

Figure 2.2: Simulated (a) I_C, I_B and (b) x_i/W_{epi}, $V_{B_2C_1}$, $V^{\star}_{B_2C_2}$, $V_{B_2C_2}$ versus V_{BE} at V_{CB} = 0V.

Fig. 2.2(a) shows I_C and I_B versus V_{BE}. A kink observed on I_C-V_{BE} at V_{BE} = 0.8 V implies when high injection occurs. Fig. 2.2(b) shows x_i/W_{epi}, $V_{B_2C_1}$, $V^{\star}_{B_2C_2}$ and $V_{B_2C_2}$ versus V_{BE}. At low V_{BE}, $V_{B_2C_1}$ = V_{BC} = 0 V. With increasing V_{BE}, a voltage drop over R_{CC} compared to R_{BV} and R_{BC} makes $V_{B_2C_1}$ increase up to V_{BE} = 1 V and then decrease with higher V_{BE}. At high $V_{BE} > 0.7$ V, an increasing $V_{B_2C_2}$-V_{BE} and a large voltage drop over epi-layer for the difference of $V_{B_2C_1}$ and $V_{B_2C_2}$ can be seen. At V_{BE} = 0.8 V, x_i/W_{epi} starts to increase much with increasing V_{BE} due to high injection effect, which also leads to an increase of $V^{\star}_{B_2C_2}$.

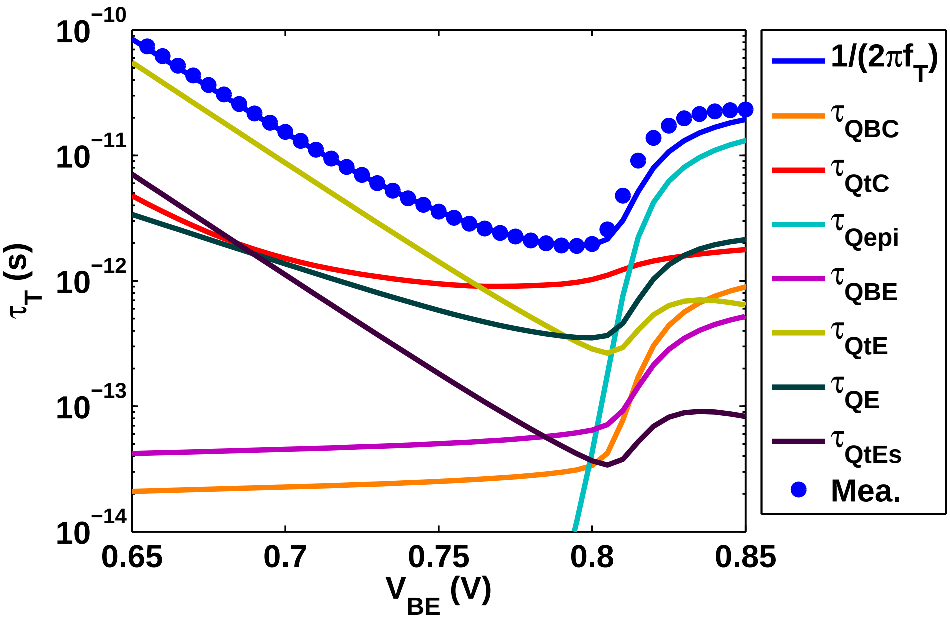

Figure 2.3: Measured and simulated τ_T versus V_{BE} at V_{CE} = 1.5 V. Individual contributions are simulated using MEXTRAM 504.12.

Fig. 2.3 shows measured and simulated τ_T versus V_{BE} at V_{CE} = 1.5 V. Individual contributions are simulated using MEXTRAM 504.12. For each charge Q, f_T is simulated by turning on only that charge, the corresponding transit time is denoted as τ_Q. τ_T drops with increasing V_{BE} first, mainly due to Q_{tE}. Peak f_T is observed at V_{BE} = 0.8 V where minimum τ_T is observed. Q_{tC} determines τ_T around peak f_T at V_{BE} = 0.8 V. τ_T increases at $V_{BE} >$ 0.8 V is due to largely increasing Q_{epi} when high injection occurs.

2.2 Main Current

I_N is based on the generalized Moll-Ross relation [20] [21], also known as the integral charge control relation (ICCR):

$$I_N = \frac{I_f - I_r}{q_B^I}. \tag{2.22}$$

where I_f is forward current

$$I_f = I_s \exp\left(\frac{V_{B_2E_1}}{N_{FF} \cdot V_T}\right), \tag{2.23}$$

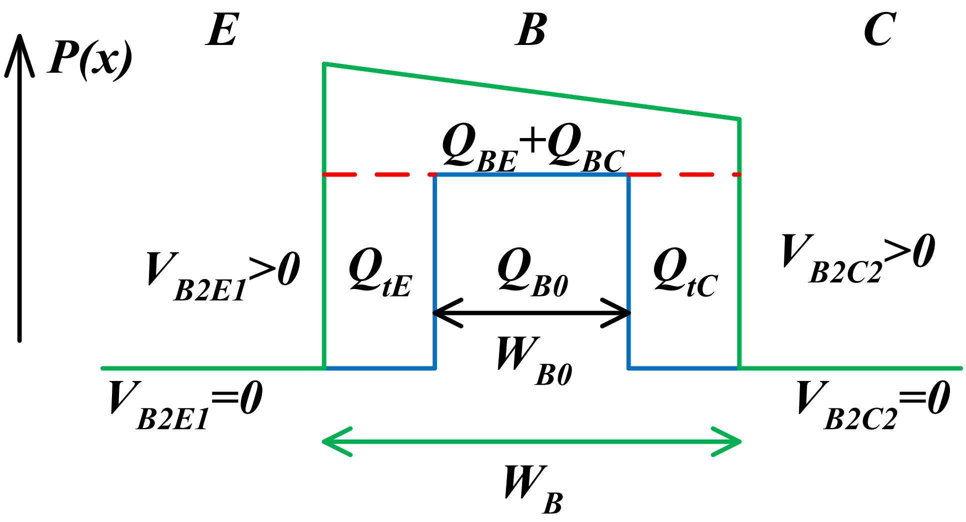

Figure 2.4: Definition of depletion and diffusion charges used in Mextram [1].

where I_s is saturation current, N_{FF} is empirical forward non-ideality factor, $V_T = kT/q$ is thermal voltage, $V_{B_2E_1}$ is intrinsic base-emitter voltage. I_r is reverse current

$$I_r = \begin{cases} I_s e^{V^*_{B_2C_2}/N_{FR}V_T} & I_{C_1C_2} \geq 0 \\ I_s e^{V_{B_2C_2}/N_{FR}V_T} & I_{C_1C_2} \leq 0 \end{cases} \tag{2.24}$$

where N_{FR} is empirical reverse non-ideality factor.

$V^\star_{B_2C_2}$ only equals the node voltage $V_{B_2C_2}$ in reverse mode. q^I_B is normalized neutral base hole charge taking into account SiGe grading effect. Fig. 2.4 shows that neutral base charges Q_{B0} changes due to depletion charges Q_{tE} and Q_{tC} and diffusion charges Q_{BE} and Q_{BC} for a Si transistor. q^I_B is a product of two terms, a q_1 term representing neutral base width change, and another term representing minority carrier injection.

$$q^I_B = q^I_1 \left(1 + \frac{1}{2} n_0(V_{B_2E_1}) + \frac{1}{2} n_B(V_{B_2C^*_2})\right), \tag{2.25}$$

where n_0 and n_B are normalized electron densities to base doping at the emitter and collector edge of neutral base. According to pn product junction laws at the neutral base edges, n_0 is a function of $V_{B_2E_1}$ and n_B is a function of $V^\star_{B_2C_2}$. q^I_1 is limiting function on q^I_0 to avoid dividing by zero

$$q^I_1 = \frac{q^I_0 + \sqrt{(q^I_0)^2 + 0.01}}{2}. \tag{2.26}$$

q_0^I models the effect of neutral base width modulation on the effective Gummel number [22] [23], and was derived assuming a linearly graded band gap change and constant base doping [24]

$$q_0^I = \frac{\exp\left[\left(\frac{V_{t_E}}{V_{er}}+1\right)\frac{dE_g}{V_T}\right] - \exp\left(\frac{-V_{t_C}}{V_{ef}}\cdot\frac{dE_g}{V_T}\right)}{\exp\left(\frac{dE_g}{V_T}\right)-1}. \tag{2.27}$$

where V_{t_E} and V_{t_C} represent base width changes, calculated from changes of base-emitter and base-collector depletion charges. V_{er} and V_{ef} are reverse and forward Early voltages. dE_g is the band gap difference across the neutral base at V_{BE} = 0 V and V_{BC} = 0 V, i.e. in thermal dynamic equilibrium. V_{tC} relates to Q_{tC}, so there is the question of what the control voltage should be, given the previous discussions of multiple internal V_{BC} voltages, which will be discussed in the next section.

An accurate modeling of I-V and C-V characteristics are important for distortion analysis for SiGe HBT. The avalanche model and CB depletion capacitance are two dominant nonlinearities to determine IP3 modeling [12] [13] [14]. CB depletion capacitance and avalanche model will be described.

2.3 Collector-base Depletion Capacitance Model

In Mextram 504.12 [15] and 505.00 [1], the intrinsic collector-base (CB) depletion capacitance C_{tC} is given by

$$C_{tC} = \frac{dQ_{tC}}{dV_{junc}} = XCJC \cdot C_{jC}\left[(1-X_p)\frac{f_I(I_{C_1C_2})}{(1-V_{jC}/V_{dC})^{P_C}} + X_p\right], \tag{2.28}$$

where $XCJC$ is fraction of intrinsic CB depletion capacitance. C_{jC} is the zero bias C_{tC}, V_{dC} is CB built-in potential, P_C is CB junction grading coefficient. X_p is a parameter for describing full depletion of epi-layer at high V_{CB}. The current modulation factor $f_I(I_{C_1C_2})$ has its own grading coefficient M_C and uses the parameter I_{hc} from the epi-layer model [1]

$$f(I_{C_1C_2}) = \left(1 - \frac{I_{C_1C_2}}{I_{C_1C_2}+I_{hc}}\right)^{M_C}, \tag{2.29}$$

where I_{hc} is hot-carrier current [15] and M_C is a parameter controlling I_C dependence. V_{jC} is the effective CB junction voltage for depletion capacitance model. V_{jC} is a smoothly limited version of V_{junc}, the CB junction voltage for controlling depletion charge Q_{tC}. The smoothing function used is

$$V_{jC} = V_{junc} - V_{ch} \ln \left[1 + \exp \left(\frac{V_{junc} - V_{FC}}{V_{ch}} \right) \right], \tag{2.30}$$

where V_{ch} controls the abruptness of the smooth limiting, $V_{FC} = V_{dC}(1 - a_{jC}^{-P_C})$, with model constant $a_{jC} = 2$ for CB depletion capacitance. Three options of V_{junc} are specified by SWVJUNC in MEXTRAM 505.00

$$V_{junc} = \begin{cases} V_{B_2C_2} & \text{for SWVJUNC = 0} \\ V_{B_2C_1} & \text{for SWVJUNC = 1} \\ V_{B_2C_1} + V_{xi0} & \text{for SWVJUNC = 2} \end{cases}, \tag{2.31}$$

where V_{xi0} is epi-layer voltage drop assuming that epi-layer resistance is at its injection width $x_i = 0$ value when quasi-saturation starts, calculated by [1]

$$B_1 = \frac{1}{2} SCR_{CV} (I_{C_1C_2} - I_{hc}), \tag{2.32}$$

$$B_2 = SCR_{CV} \cdot R_{CV} \cdot I_{hc} \cdot I_{C_1C_2}, \tag{2.33}$$

$$V_{xi0} = B_1 + \sqrt{B_1^2 + B_2}. \tag{2.34}$$

V_{ch} is made to increase with $I_{C_1C_2}$ to avoid a steep increase of the overall C_{BC} with V_{BE} at high injection [1]. Two options of V_{ch} are given by SWVCHC in MEXTRAM 505.00

$$V_{ch} = \begin{cases} 0.1 V_{dC} & \text{for SWVCHC = 0} \\ V_{dC} \left(0.1 + 2 \frac{I_{C_1C_2}}{I_{C_1C_2} + I_{qs}} \right) & \text{for SWVCHC = 1} \end{cases}, \tag{2.35}$$

where I_{qs} is quasi-saturation onset current [1].

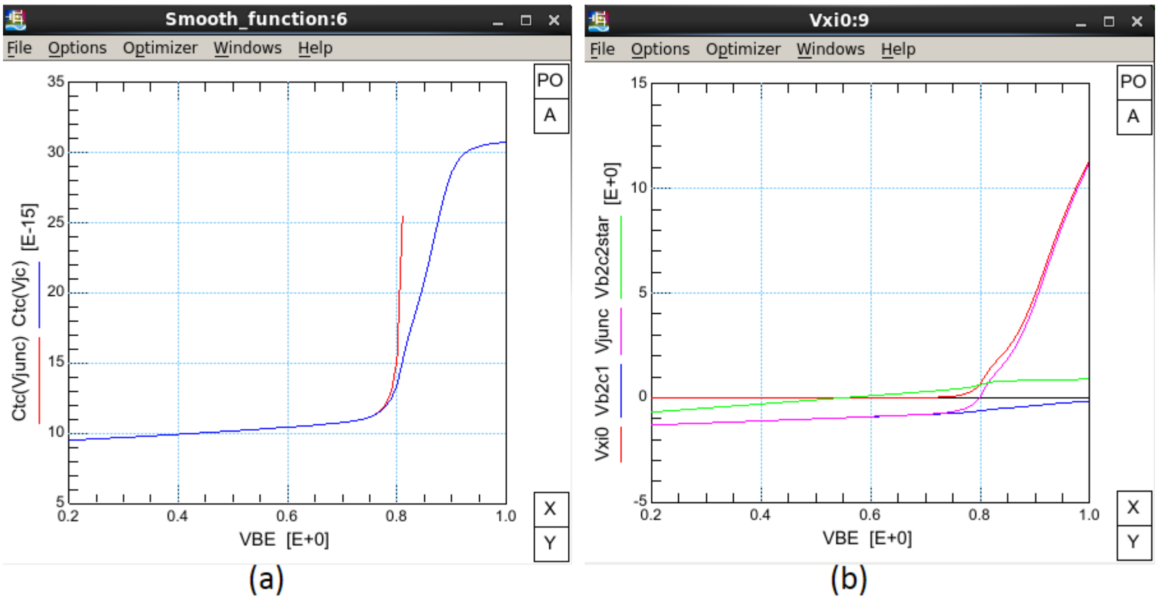

Figure 2.5: (a) Simulated C_{tC}-V_{BE} in (2.3) compared to junction voltage without smoothing limitation using the parameters extracted for the common-emitter SiGe HBT. (b) V_{BE} dependence of V_{xi0}, $V_{B_2C_1}$, $V^{\star}_{B_2C_2}$ and $V_{junc} = V_{B_2C_1} + V_{xi0}$. V_{CB} = 1.5 V

Fig. 2.5(a) shows simulated C_{tC}-V_{BE} in (2.3) using the parameters extracted for the common-emitter SiGe HBT. V_{CB} = 1.5 V. The simulated C_{tC}-V_{BE} calculated by junction voltage without smoothing limitation with the same parameters is also shown. The ideal formulation without smoothing limitation gives problems when $V_{junc} > V_{dC}$ around V_{BE} = 0.8 V, although it is not so important in MEXTRAM 504.12 to have a physical description of depletion charge for $V_{junc} > V_{dC}$ when the diffusion charge dominates [15]. With V_{jC}, a smoothly limiting version of V_{junc}, V_{jC} will be always smaller than V_{dC} and C_{tC} turns to $a_{jC} \cdot C_{jC}$ when $V_{jC} > V_{dC}$. V_{ch} is used to adjust the abruptness of transition. However, an underestimated C_{tC} would directly result in OIP3 issue as will be shown in Chapter 3. Fig. 2.5(b) shows V_{BE} dependence of V_{xi0}, $V_{B_2C_1}$, $V^{\star}_{B_2C_2}$ and $V_{junc} = V_{B_2C_1} + V_{xi0}$. V_{CB} = 1.5 V. V_{xi0} becomes rapidly increases when high injection occurs around V_{BE} = 0.8 V, which results in a rapid increase of V_{junc} at high current. It can be clearly seen that $V^{\star}_{B_2C_2}$ is much larger than $V_{B_2C_1}$ even at low V_{BE} and gives unphysical value for Q_{tC} purpose if used as V_{junc} at low current, because it is mainly a result of mathematical smoothing of epi-layer injection width x_i before onset of quasi-saturation. So $V^{\star}_{B_2C_2}$ is not used as V_{junc}, although Q_{tC}, the CB depletion charge corresponding to C_{tC}, is placed between B_2 and C_2.

2.4 Avalanche Model

In reverse mode ($I_{C_1C_2} < 0$) or hard saturation $V_{B_2C_1} > V_{dCT}$, both the avalanche current I_{AVL} and the multiplication factor M-1 are zero. So M-1 and its each order derivatives, at least the first order derivative should be 0 as $\frac{\partial(M-1)}{\partial V_{B_2C_1}}\Big|_{V_{B_2C_1=V_{dCT}}}$ = 0. In forward mode, three options of M-1 are specified by SWAVL in Mextram 505.00. For SWAVL=0, avalanche current and M-1 will be zero.

$$I_{AVL} = 0, M - 1 = 0. \tag{2.36}$$

For SWAVL=1, the avalanche model [25] first introduced in Mextram 505.00 is used for improved voltage dependence and improved temperature dependence.

$$M - 1 = \frac{A_{avl}}{B_{avlT}}\phi \exp(-B_{avlT}\phi^{C_{avl}}), \tag{2.37}$$

and temperature dependence of M-1 relies on variable B_{avlT}.

$$B_{avlT} = B_{avl}(T_{ref}) \cdot (1 + T_{Bavl} \cdot (T - T_{ref})), \tag{2.38}$$

where B_{avl} and T_{Bavl} are model parameters. T is ambient temperature and T_{ref} is reference temperature. ϕ is CB junction potential drop

$$\phi = (V_{dCavl} - V_{B_2C_1}) \exp(-\frac{I_N}{I_{TOavl}}), \tag{2.39}$$

where A_{avl}, B_{avl}, C_{avl}, V_{dCavl}, T_{Bavl} are model parameters. A_{avl} and B_{avl} are directly related to model constant A_n and B_n in Mextram 504.12 but with extra degree of freedom in fitting. I_{TOavl} is an extra parameter to empirically model current dependence of M-1, making ϕ at high I_N decrease and thus M-1 decrease. M-1 = 0 when $\phi < 0$, so the continuity should be kept at first order derivative of M-1 around ϕ = 0 as

$$\begin{aligned}\frac{\partial(M-1)}{\partial V_{B_2C_1}} =&\frac{\partial(M-1)}{\partial\phi}\cdot\frac{\partial\phi}{\partial V_{B_2C_1}}\\ =&\frac{A_{avl}}{B_{avlT}}\cdot\exp(-B_{avlT}\cdot\phi^{C_{avl}})\cdot(1-B_{avlT}C_{avl}\phi^{C_{avl}})\cdot\big[-\exp(-\frac{I_N}{I_{TOavl}})\big]^{,}\end{aligned} \tag{2.40}$$

where

$$\lim_{\phi\to0^+}\phi^{C_{avl}}=0, \tag{2.41}$$

$$\lim_{\phi\to0^+}\exp(-B_{avlT}\cdot\phi^{C_{avl}})=0, \tag{2.42}$$

so $\lim\limits_{\phi\to0^+}\dfrac{\partial(M-1)}{\partial V_{B_2C_1}}=0$. M-1 and $\partial(M-1)/\partial V_{B_2C_1}$ are continuous at all V_{CB}.

For SWAVL=2, avalanche model in earlier Mextram 504.12 is used. M-1 is derived based on Chynoweth's empirical law [26] for the ionisation coefficient

$$M-1=\int_0^{W_{\mathrm{AVL}}}A_n\exp\left(-\frac{B_n}{|E(x)|}\right)dx, \tag{2.43}$$

$$=\frac{A_n}{B_n}\lambda_D E_M\left\{\exp\left[-\frac{B_n}{E_M}\right]-\exp\left[-\frac{B_n}{E_M}\left(1+\frac{W_{\mathrm{AVL}}}{\lambda_D}\right)\right]\right\}, \tag{2.44}$$

where E_M is maximum electric field, λ_D is zero field extrapolation length, W_{AVL} is effective epi-layer width. A_n and B_n are model constants. At given V_{CB}, E_M and λ_D are calculated using standard abrupt junction electrostatics theory, with a doping concentration determined from W_{AVL} and V_{AVL}, the only two dedicated M-1 model parameters.

Fig. 2.6(a) shows the electrical field distribution assumed in MEXTRAM 504.12 at low current, when the maximum electrical field located between base and epi-layer. W_D is the width of the depletion region. EXAVL is a switch for extended avalanche model to model an increasing E_M with I_N at high current due to Kirk effect. When EXAVL = 0, the slope of $|E|$ is negative in this case. Fig. 2.6(b) shows the electrical field distribution in MEXTRAM 504.12 at high current when quasi-saturation occurs. The maximum electrical field is located between epi-layer and buried layer when EXAVL = 1.

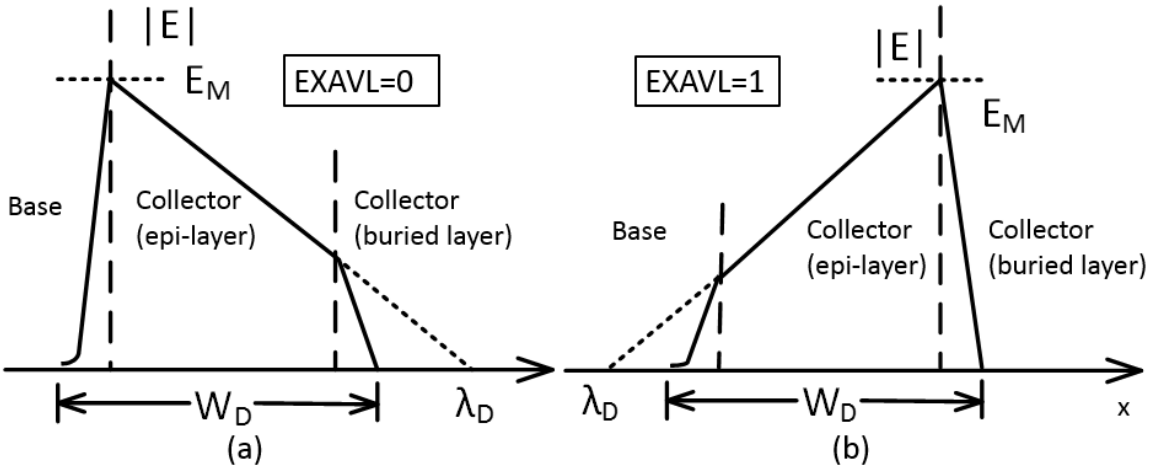

Figure 2.6: The MEXTRAM 504.12 considerations on electrical field distribution for (a) maximum electrical field located between base and epi-layer when EXAVL = 0. (b) maximum electrical field located between epi-layer and buried layer when EXAVL = 1.

The gradient of the electric field for zero bias is first calculated [15]:

$$dEdx_0 = \frac{2\,V_{avl}}{W_{avl}^2}. \tag{2.45}$$

The depletion layer thickness is then calculated [15]:

$$x_D = \sqrt{\frac{2}{dEdx_0}}\,\sqrt{\frac{V_{dC} - V_{B_2C_1}}{1 - I_{\mathrm{cap}}/I_{hc}}}, \tag{2.46}$$

and I_{cap} is limiting version of $I_{C_1C_2}$ that is always smaller than I_{hc} as [15]

$$I_{cap} = \frac{I_{hc} I_{C_1C_2}}{I_{hc} + I_{C_1C_2}}. \tag{2.47}$$

When EXAVL=0, then the effective thickness of the epi-layer is [15]

$$W_{\mathrm{eff}} = W_{avl}. \tag{2.48}$$

When EXAVL=1, [15],

$$W_{\mathrm{eff}} = W_{avl}\left(1 - \frac{x_i}{2\,W_{epi}}\right)^2. \tag{2.49}$$

For either value of EXAVL the thickness over which the electric field is important is [15]

$$W_D = \frac{x_D\, W_{\text{eff}}}{\sqrt{x_D^2 + W_{\text{eff}}^2}}. \tag{2.50}$$

The average electric field and the field at the base-collector junction are [15]

$$E_{\text{av}} = \frac{V_{dC} - V_{B_2C_1}}{W_D}, \tag{2.51}$$

$$E_0 = E_{\text{av}} + \frac{1}{2} W_D dEdx_0 \left(1 - \frac{I_{\text{cap}}}{I_{hc}}\right), \tag{2.52}$$

When EXAVL=0, then the maximum of the electric field is

$$E_M = E_0. \tag{2.53}$$

When EXAVL=1, the current crowding effect is also considered through spreading parameter S_{fH} to model a modified maximum electrical field as [15]

$$SH_W = 1 + 2\, S_{fH} \; \left(1 + 2\, \frac{x_i}{W_{epi}}\right), \tag{2.54}$$

$$E_{\text{fi}} = \frac{1 + S_{fH}}{1 + 2\, S_{fH}}, \tag{2.55}$$

$$E_W = E_{\text{av}} - \frac{1}{2} W_D dEdx_0 \left(E_{\text{fi}} - \frac{I_{C_1C_2}}{I_{hc} SH_W}\right), \tag{2.56}$$

$$E_M = \frac{1}{2}\left(E_W + E_0 + \sqrt{(E_W - E_0)^2 + 0.1\ E_{\text{av}}^2\ I_{\text{cap}}/I_{hc}}\right). \tag{2.57}$$

The injection thickness x_i/W_{epi} is given in main current calculation. For either value of EXAVL the intersection point λ_D is [15]

$$\lambda_D = \frac{E_M\, W_D}{2\,(E_M - E_{\text{av}})}. \tag{2.58}$$

Temperature dependence is accounted for through V_{DC} and B_n.

Compared to avalanche model in MEXTRAM 504, our previous work in [25] shows that the proposed avalanche model in MEXTRAM 505.00 has an improved V_{CB} dependence over a wide temperature range from 93 K to 393 K in an IBM 5AM SiGe BiCMOS technology [27].

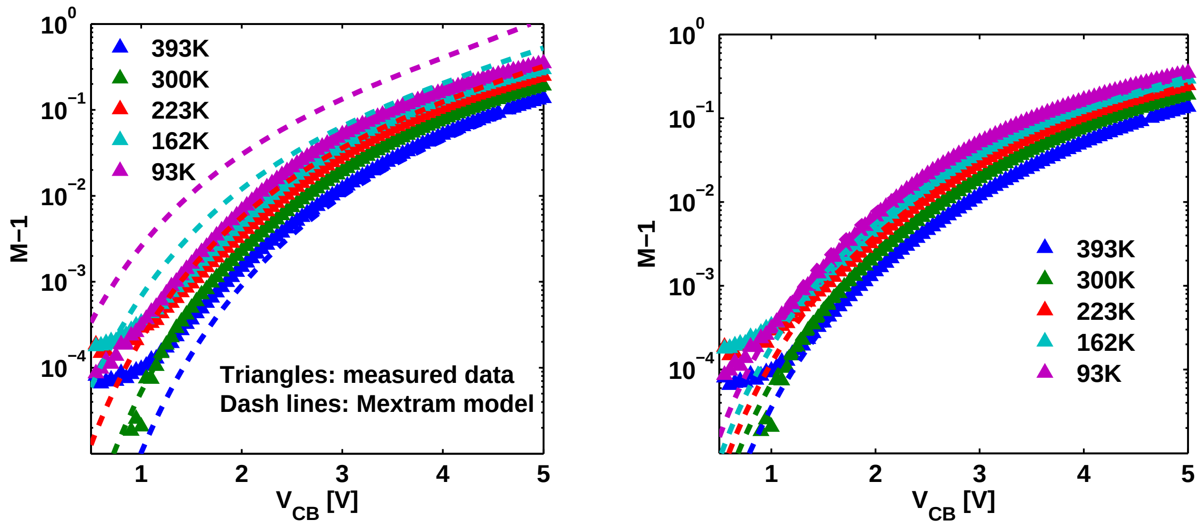

Figure 2.7: Measured and simulated (a) M-1-V_{CB} using Mextram 504.12 and (b) M-1-V_{CB} using Mextram 505.00 from 93 K to 393 K in an IBM 5AM SiGe BiCMOS technology. A low I_C around 7 μA is used.

Fig. 2.7(a) shows measured and simulated M-1 versus V_{CB} using Mextram 504.12 from 93 K to 393 K for the IBM 5AM SiGe HBTs. Only two dedicated parameters WAVL and VAVL cannot provide enough accuracy for V_{CB} dependence even at low current and room temperature. Also, an empirically fixed temperature dependent B_n show a large difference on M-1 at low temperatures compared to measurement. Fig. 2.7(b) shows measured and simulated M-1 versus V_{CB} using Mextram 505.00 from 93 K to 393 K shown in logarithmic scale. A clear improvement in temperature dependence modeling can be observed. The V_{CB} dependence of M-1 at each temperature is also better modeled.

Fig. 2.8(a) shows measured and simulated I_B-V_{CB} using MEXTRAM 504.12 at I_E from 10 μA to 40 mA for common-base HV SiGe HBT from NXP QUBiC4Xi technology. At I_E = 10 μA, I_B-V_{CB} cannot be fitted well, which implies the V_{CB} dependence of M-1 needs to be improved even at low current. With increasing I_E, a clear difference can be also observed on I_B-V_{CB} at lower V_{CB}, which implies that the M-1 model has limited accuracy for current

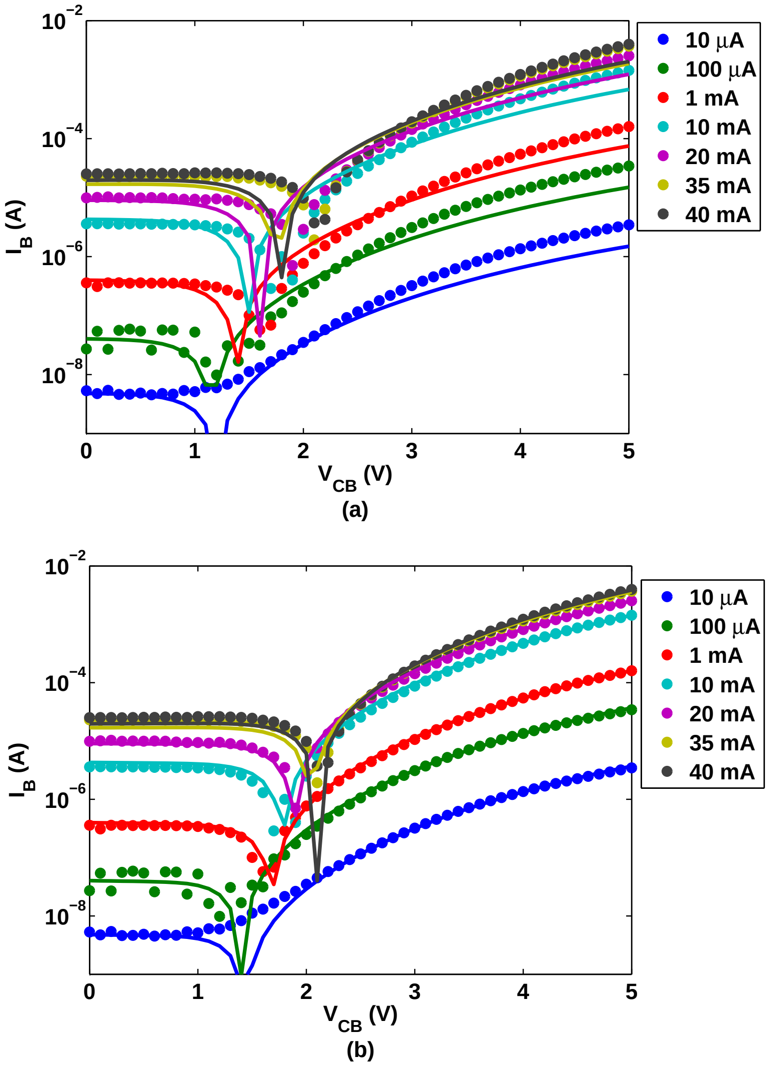

Figure 2.8: Measured and simulated (a) I_B-V_{CB} using MEXTRAM 504.12 (b) I_B-V_{CB} using MEXTRAM 505.00 at I_E from 10 μA to 40 mA. The common-base HV SiGe HBT from NXP technology is used.

dependence. Fig. 2.8(b) shows measured and simulated I_B-V_{CB} using MEXTRAM 505.00 at I_E from 10 μA to 40 mA. At each I_E up to 40 mA, a good fitting of I_B-V_{CB} implies that both I_E and V_{CB} dependence of M-1 are accurately fitted in MEXTRAM 505.00.

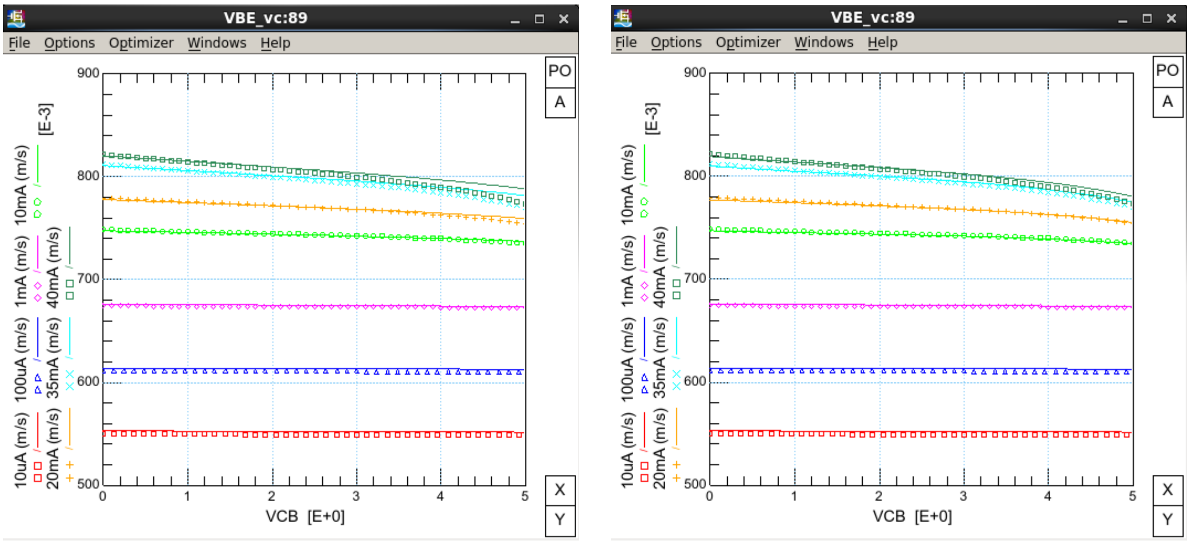

(a) (b)

Figure 2.9: Measured and simulated (a) V_{BE}-V_{CB} using MEXTRAM 504.12 (a) V_{BE}-V_{CB} using MEXTRAM 505.00 at I_E from 10μA to 40 mA.

Fig. 2.9(a) shows measured and simulated (a) V_{BE}-V_{CB} using MEXTRAM 504.12 at I_E from 10μA to 40 mA. A good fitting for V_{BE}-V_{CB} at low $I_E < 10$ mA is due to an accurate R_E extraction. The difference of V_{BE} can be observed $V_{CB} > 3$ V at $I_E > 20$ mA because I_B is not fitted well. So underestimated I_B at both high V_{CB} and I_E in Fig. 2.8(a) leads to smaller voltage drop over base resistance and overestimated V_{BE} in Fig. 2.9(a). Fig. 2.9(b) shows measured and simulated (a) V_{BE}-V_{CB} using MEXTRAM 505.00 at I_E from 10μA to 40 mA. An improved I_B-V_{CB} in Fig. 2.8(b) directly results in a good fitting of V_{BE}-V_{CB} at both high V_{CB} and I_E.

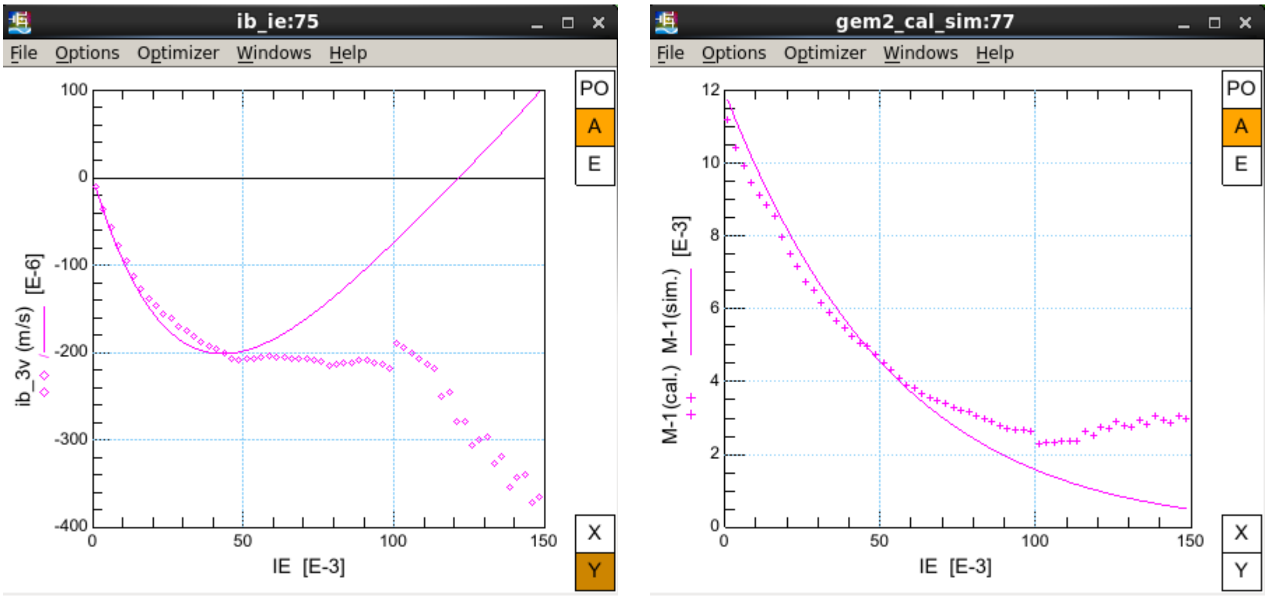

(a) (b)

Figure 2.10: (a) Measured and MEXTRAM 505.00 simulated I_B-I_E up to I_E = 150 mA. (b) Simulated M-1 versus I_E and the extracted M-1 from [2] is also shown as reference. V_{CB} = 3 V. The common-base HV SiGe HBT from NXP technology is used.

Fig. 2.10(a) shows measured and MEXTRAM 505.00 simulated I_B-I_E up to I_E = 150 mA. V_{CB} = 3 V. The common-base HV SiGe HBT from NXP technology is used. A clear difference can be seen for I_B-I_E at $I_E > 50$ mA, although a good fitting can be obtained at low current. Fig. 2.10(b) shows simulated and extracted M-1 versus I_E. The M-1 extraction method in [2] is used. A clear limitation on current dependence of avalanche model of MEXTRAM 505.00 can be seen at medium $I_E > 50$ mA. At $I_E > 100$ mA, an increasing extracted M-1 can be seen due to high injection effect when the maximum of electrical field is located in the interface between epi-layer and buried layer.

Chapter 3

Common-Emitter IP3 modeling

The main purpose of this chapter is to solve the critical problems of accurately simulating the third order distortion current, real part, imaginary part as well as magnitude, and the resulting IP3 for common-emitter configuration within the framework of the industry standard Mextram model. Parameter extraction interdependence for simultaneous fitting of transistor S-parameters and distortion are addressed. The solution also has implications on the modeling of high injection C_{BC} beyond f_T roll-off. We will present a solution that allows much improved modeling of both third order distortion and C_{BC} at high injection.

The device used is a 0.5×20.7 μm^2 high breakdown SiGe HBT with performance similar to HBTs of QUBiC4Xi technology [28]. Peak f_T = 84 GHz. f_{max} = 162 GHz. BV_{CBO} = 12 V. DC I-V, S-parameters and X-parameters are measured on-wafer. An Agilent X-parameter nonlinear network analyzer is used for measuring X-parameters [29]. Both the real and imaginary parts of voltage and current are measured. To our best knowledge, this is the first time measured real and imaginary parts of harmonic current is compared with compact modeling for bipolar transistors. Model parameters are extracted by fitting DC I-V, S-parameters and harmonic currents, particularly f_T and OIP3. Note that there are no dedicated parameters for fitting harmonic currents or OIP3. However, a major issue is that near the measured OIP3 peak, the model cannot fit measurement well, no matter how model parameters are adjusted, even if we sacrifice fitting of f_T.

Fig. 3.1(a) shows measured OIP3 versus base-emitter voltage (V_{BE}) on the left y-axis, together with normalized cut-off frequency (f_T) and base-collector capacitance (C_{BC}) on the right y-axis for a common-emitter SiGe HBT at a V_{CE} of 1.5 V. Also shown are simulations

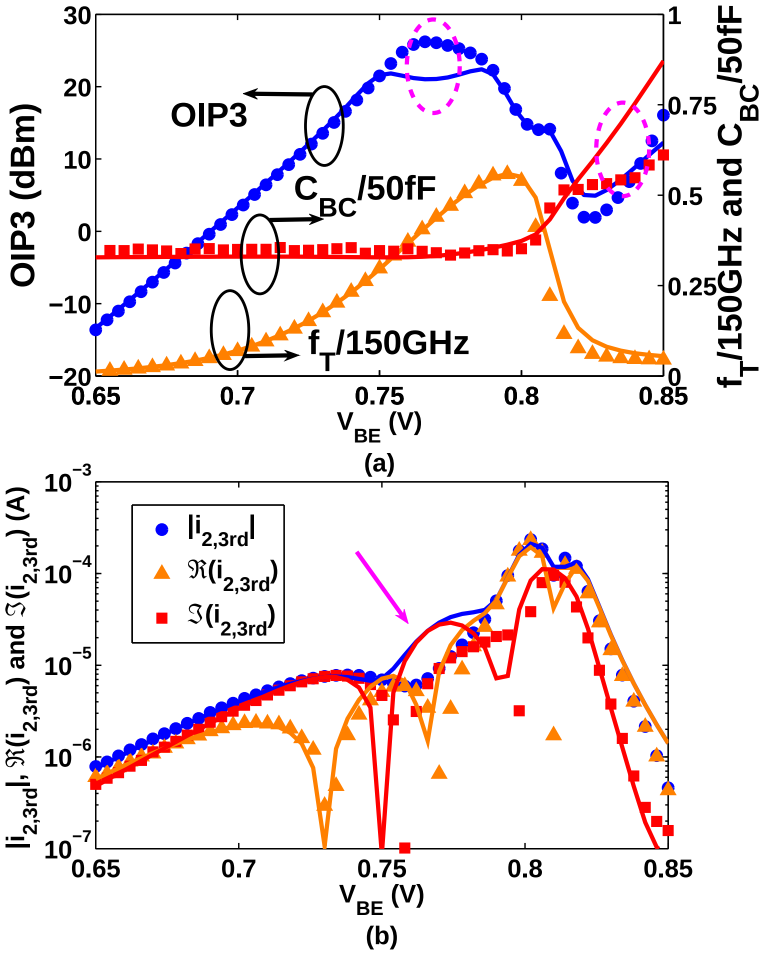

Figure 3.1: (a) OIP3, on the left y-axis, and f_T/100GHz, C_{BC}/50fF on the right y-aixs versus V_{BE}. (b) Magnitude, real and imaginary part of third order output current $i_{2,3rd}$ versus V_{BE}. V_{CE} = 1.5 V. The simulations are made using Mextram 504.12.

using MEXTRAM 504.12, an industry standard compact model of bipolar transistors [15]. C_{BC} is extracted from imaginary part of Y_{12}, $\Im(Y_{12})$, using $C_{BC} = -\Im(Y_{12})/\omega$. ω is angular frequency. The measured OIP3 increases with V_{BE} and peaks around 0.77 V, and then rolls off. Observe that the OIP3 peak occurs before the f_T peak, which was the case in another SiGe technology as well [10]. OIP3 is well modeled for V_{BE} up to 0.75 V. However, the model is not able to reproduce the position or the value of OIP3 peak, which presents a problem for biasing optimization to maximize linearity. No matter how parameters are tuned, even at the expense of worse f_T fitting, it is not possible to fit measured OIP3 around its peak. A small dip is produced by the model, which is misleading for bias optimization in RF design.

Fig. 3.1(b) compares measured and simulated magnitude, real and imaginary parts of third order output current $i_{2,3rd}$. The sharp dips of the real and imaginary parts indicate a change of sign. In the V_{BE} range near measured OIP3 peak, the *imaginary* part of $i_{2,3rd}$ dominates over the real part in simulation (lines) and its value is much higher than measurement (symbols). This points to C_{BC} modeling as a potential problem, as was also indicated in prior studies for SiGe HBTs from other technologies [12] [13] [14]. The simulated C_{BC} in Fig. 3.1(a) cannot capture a kink observed in measurement at $V_{BE} > 0.82$ V. This C_{BC} issue is related to high injection as peak f_T occurs at around 0.8 V.

3.1 Collector-Base Depletion Capacitance Model

We discussed earlier that a likely source for the OIP3 peak problem is the CB depletion capacitance since the imaginary part of $i_{2,3rd}$ is overestimated, as can be seen from Fig. 3.1(b). To confirm this, we first review the CB depletion capacitance model in MEXTRAM and analyse its behavior near the OIP3 peak. Fig. 3.2 shows a simplified equivalent circuit of MEXTRAM

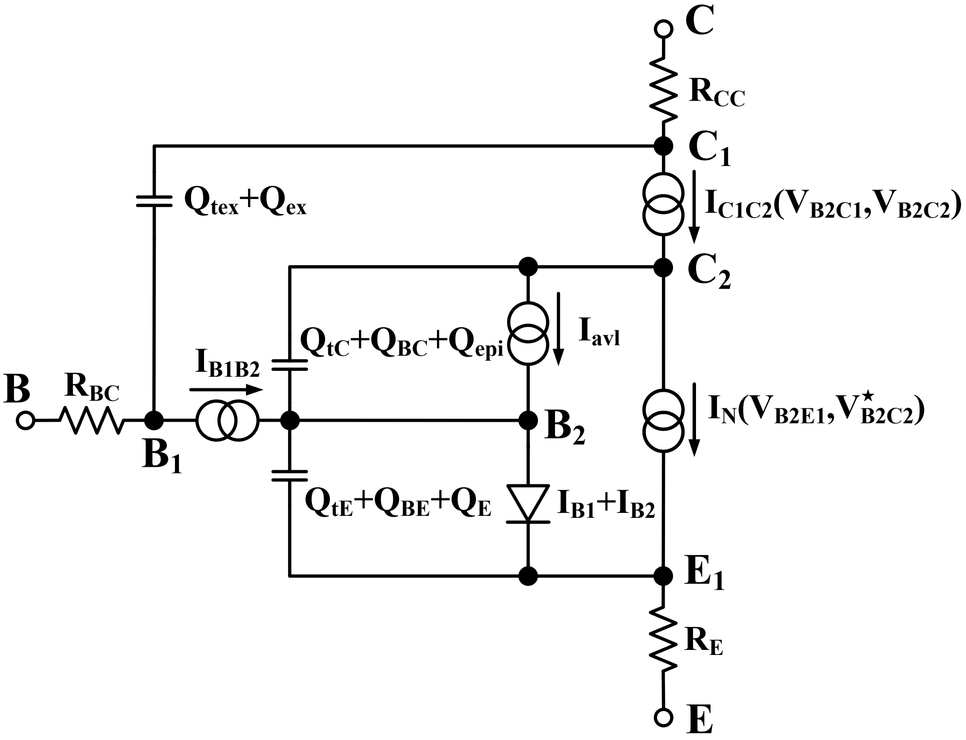

Figure 3.2: A simplified equivalent circuit of MEXTRAM.

504.12 [15]. The parasitic PNP, side-wall components and overlap capacitances are not shown.

In simulation, the complete Mextram circuit of Fig. 2.1 is used. C, C_1, C_2, B, B_1, B_2, E, E_1 are circuit nodes. I_{AVL} is avalanche current. I_{B1} and I_{B2} are ideal and non-ideal base currents. Q_{tC}, Q_{BC} and Q_{epi} are intrinsic base-collector depletion charge, base-collector diffusion charge and epi-layer diffusion charge, respectively. Q_{tE}, Q_{BE} and Q_E are intrinsic base-emitter depletion charge, base-emitter diffusion charge. and emitter diffusion charge, respectively. Q_{tex} and Q_{ex} are extrinsic base-collector depletion and diffusion charges. R_{CC}, R_{BC}, R_E are respectively constant collector, base and emitter resistances. $I_{B_1B_2}$ describes variable base resistance modulated by the base width variation. I_N is main current. $I_{C_1C_2}$, the epi-layer current, is calculated from $V_{B_2C_1}$ and $V_{B_2C_2}$ using the Kull model [16], according to Eqn. (2.1)-(2.5) in Chapter 2 . An effective intrinsic CB junction bias $V^{\star}_{B_2C_2}$ is calculated from $I_{C_1C_2}$ and $V_{B_2C_1}$, and used for I_N [30], as described in Chapter 2 by Eqn. (2.22]) to (2.24]). The $V_{B_2C_2}$ value given by circuit simulator thus does not have a physical meaning [30] [15], because no voltage drop over epi-layer is considered in $V_{B_2C_2}$.

Recall that in Fig. 3.1(b), simulated $\Im(i_{2,3rd})$ is much higher than the measurement near the measured OIP3 peak. This suggests CB capacitance modeling could be at issue, which was previously found to be important for IP3 in other SiGe HBT technologies [12] [13] [14] [2]. As OIP3 is very sensitive to CB depletion capacitance modeling, which we will show below, C_{tC} and its derivatives with respect to $I_{C_1C_2}$ and $V_{B_2C_1}$ can have a large impact on distortion. Even though C_{BC} around OIP3 peak from 0.75 to 0.79V is reasonably modeled, its internal derivatives with respect to $I_{C_1C_2}$ and $V_{B_2C_1}$ may not. Below we first describe the essence of MEXTRAM's CB junction depletion capacitance model.

For simplicity in discussion, below we set XP = 0 and XCJC = 1 in the complete C_{tC} model of Eqn. (2.3) in Chapter 2. In simulation, the extracted XP and XCJC are used. XP is a parameter for describing full depletion of epi-layer at high V_{CB} and XCJC is the fraction of intrinsic C_{tC} [15]. The intrinsic CB depletion capacitance C_{tC} is given by [15]

$$C_{tC} = C_{jC}\frac{f_I(I_{C_1C_2})}{(1 - V_{jC}/V_{dC})^{P_C}}, \tag{3.1}$$

where C_{jC} is the zero bias C_{tC}, V_{dC} is CB built-in potential, P_C is CB junction grading coefficient. $f_I(I_{C_1C_2})$ describes current modulation [15]

$$f(I_{C_1C_2}) = \left(1 - \frac{I_{C_1C_2}}{I_{C_1C_2} + I_{hc}}\right)^{M_C}, \tag{3.2}$$

where I_{hc} is hot-carrier current [15] and M_C is a parameter controlling I_C dependence. V_{jC} is a smoothly limited version of V_{junc}, the CB junction voltage for controlling depletion charge. The smoothing function used is

$$V_{jC} = V_{junc} - V_{ch} \ln\left[1 + \exp\left(\frac{V_{junc} - V_{FC}}{V_{ch}}\right)\right], \tag{3.3}$$

where V_{ch} controls the abruptness of the smooth limiting, V_{FC} controls the transition voltage. In MEXTREAM 504.12 [15] and earlier versions, V_{junc} is modeled as

$$V_{junc} = V_{B_2C_1} + V_{xi0}. \tag{3.4}$$

where V_{xi0} is epi-layer voltage drop assuming that epi-layer resistance is at its injection width $x_i = 0$ value when quasi-saturation starts. V_{ch} is made to increase with $I_{C_1C_2}$ to avoid a steep increase of the overall C_{BC} with V_{BE} at high injection [15]

$$V_{ch} = \left(0.1 + \frac{2I_{C_1C_2}}{I_{C_1C_2} + I_{qs}}\right) V_{dC}, \tag{3.5}$$

where I_{qs} is quasi-saturation onset current [15]. Although Q_{tC}, the CB depletion charge corresponding to C_{tC}, is placed between B_2 and C_2, $V_{B_2C_2}$ is not used for V_{junc} because $V_{B_2C_2}$ has no physical meaning in forward mode [15]. $V^{\star}_{B_2C_2}$ gives an unphysical value for Q_{tC} purpose at low current [9], because it is mainly a result of mathematical smoothing of epi-layer injection width x_i before onset of quasi-saturation. So $V^{\star}_{B_2C_2}$ is not used as V_{junc}.

In addition to $V^{\star}_{B_2C_2}$, V_{jC}, V_{junc}, $V_{B_2C_1}$ and V_{ch} are also shown as a function of V_{BE} in Fig. 3.3. At low V_{BE} and I_C when epi-layer voltage drop can be neglected, V_{jC} should be close to $V_{B_2C_1}$. However, $V^{\star}_{B_2C_2}$ is much higher than $V_{B_2C_1}$ even at low $V_{BE} < 0.7$ V, making

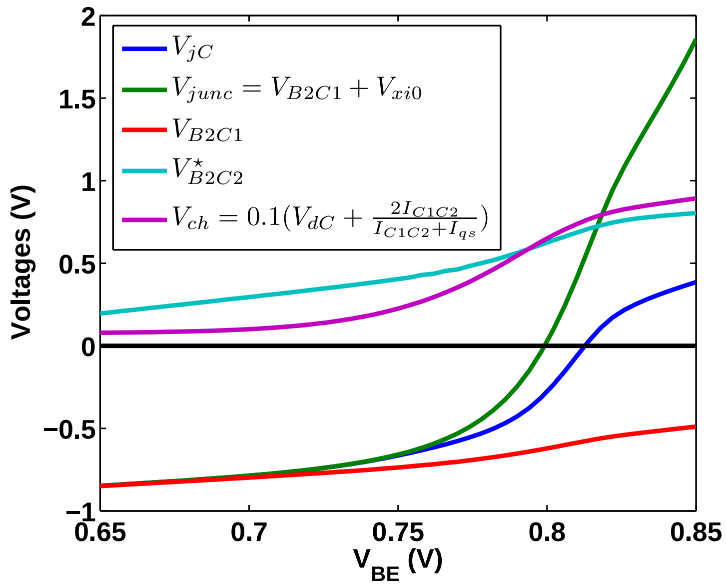

Figure 3.3: V_{BE} dependence of MEXTRAM 504.12 simulated V_{jC}, V_{junc}, $V_{B_2C_1}$, $V^{\star}_{B_2C_2}$ and V_{ch} for the same parameters used in Fig. 3.1. V_{CE} = 1.5 V.

$V^{\star}_{B_2C_2}$ unsuitable for use as C_{tC} control voltage. This high $V^{\star}_{B_2C_2}$ at $V_{BE} < 0.7$ V is simply due to the smoothing of injection width x_i necessitated by compact modeling, which is largely mathematical. At low current, V_{junc} = $V_{B_2C_1}$ + V_{xi0} increases much faster with increasing V_{BE} compared to $V_{B_2C_1}$, and becomes unphysically high in quasi-saturation, because V_{xi0} is calculated using epi-layer resistance at x_i = 0, while the actual epi-layer resistance decreases with increasing x_i. Around OIP3 peak from 0.75 to 0.78 V, V_{ch} becomes much larger than $0.1V_{dC}$ due to the current term in (3.5), which causes V_{jC} to be considerably less than V_{junc} even when V_{junc} is negative. This is clearly unphysical, particularly as this happens before any appreciable base push-out occurs. The underestimation of V_{jC} from 0.7 to 0.8 V results in poor modeling of third order output current and OIP3, as detailed below.

3.2 Improved OIP3 Modeling

To eliminate the large underestimation of V_{jC} from V_{junc} in the range of V_{BE} from 0.7 to 0.8 V, one can either remove the current dependence of V_{ch} when using V_{junc} = $V_{B_2C_1}$ + V_{xi0}, or simply use $V_{B_2C_1}$ as V_{junc}, i.e. neglecting epi-layer voltage drop so that there is no need to increase V_{ch} with increasing current. The effect of epi-layer voltage drop at higher current can be partially accounted for through the f_I term in (3.1) as detailed below.

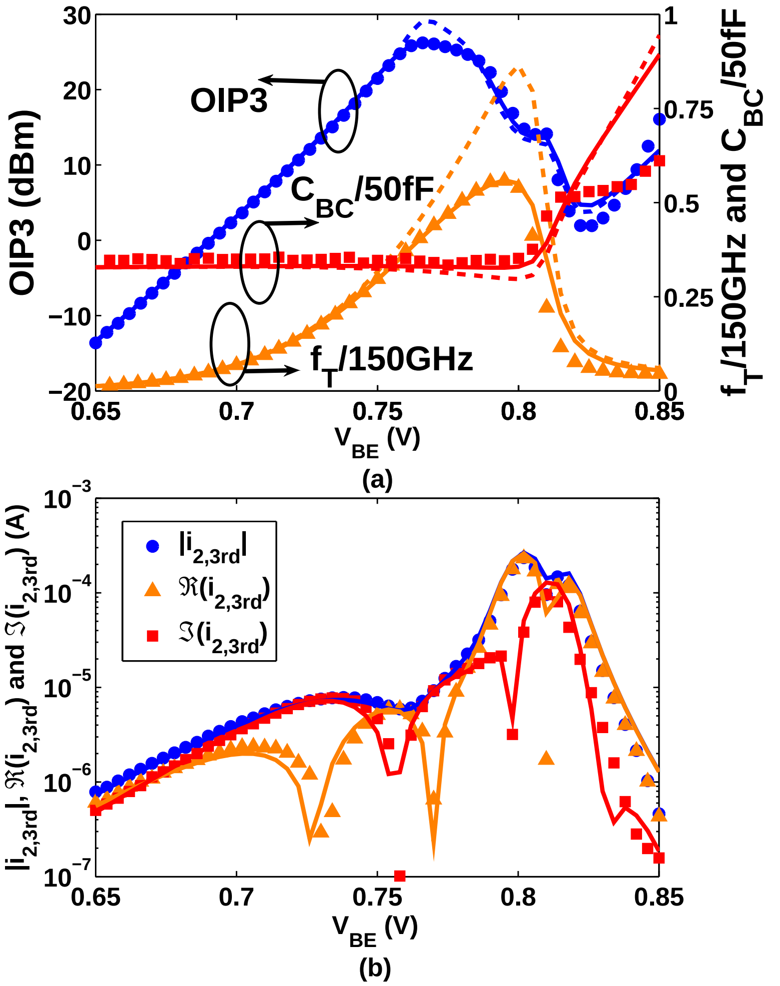

Figure 3.4: V_{BE} dependence of (a) OIP3, f_T, C_{BC} and (b) $|i_{2,3rd}|$, $\Re(i_{2,3rd})$, $\Im(i_{2,3rd})$ with V_{junc} = $V_{B_2C_1}$, V_{ch} = $0.1V_{dC}$.

We consider below first neglecting the epi-layer voltage drop, i.e. V_{junc} = $V_{B_2C_1}$, V_{ch} = $0.1V_{dC}$. Fig. 3.4(a) shows OIP3, f_T and C_{BC} obtained first using the same model parameters as in Fig. 3.1(a), as shown by the dashed lines. This change of C_{tC} model considerably improves OIP3 near its measurement peak. The peak behavior is correctly modeled, with a peak OIP3 value slightly higher than measurement. f_T and C_{BC} around the peak f_T become worse, as expected. As is shown in Fig. 3.5, without current dependence in V_{junc} and V_{ch}, V_{jC} is less, so C_{tC} is less, C_{BC} is then less compared to that in Fig. 3.1(a). Removal of epi-layer voltage drop in V_{junc} reduces the total effective resistance in series with C_{tC}. The decrease in C_{tC} and the effective series resistance cause a significant reduction of C_{tC} related transit time τ_{QtC}, and hence considerable f_T increase.

To further fit OIP3 peak value and f_T, τ_B, τ_E and the C_{tC} current dependence parameter M_C are adjusted. The results are shown in solid lines in Fig. 3.4(a). As we are using $V_{B_2C_1}$ as C_{tC} control voltage (V_{junc}), current dependence of C_{tC} is decreased compared to using $V_{B_2C_1}$ + V_{xi0} as V_{junc}. The use of a smaller M_C compensates this by making current modulation factor f_I in C_{tC} stronger, as shown in Fig. 3.5(a), where C_{tC} and the f_I factor are calculated from three modeling options

(i) $V_{junc} = V_{B_2C_1} + V_{xi0}$, $V_{ch} = \left(0.1 + \frac{2I_{C_1C_2}}{I_{C_1C_2}+I_{qs}}\right) V_{dC}$ with parameters from Fig. 3.1, including $M_C = 0.99$.

(ii) $V_{junc} = V_{B_2C_1}$, $V_{ch} = 0.1V_{dC}$ with parameters from Fig. 3.1, including $M_C = 0.99$. This gives the dashed lines in Fig. 3.4(a).

(iii) $V_{junc} = V_{B_2C_1}$, $V_{ch} = 0.1V_{dC}$ with parameters retuned to further fit OIP3 peak, and refit f_T and C_{BC}, including $M_C = 0.46$. This gives the solid lines in Fig. 3.4(a).

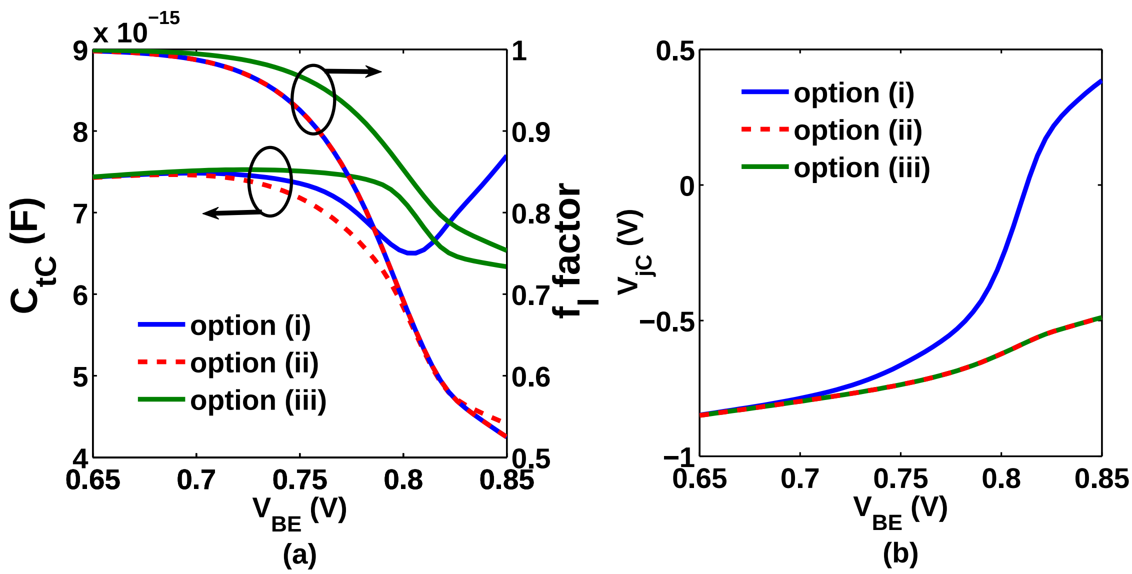

Figure 3.5: V_{BE} dependence of simulated (a) C_{tC} on the left y-axis and f_I factor on the right y-axis and (b) V_{jc} with modeling options (i), (ii) and (iii).

Fig. 3.5(b) shows V_{jC}-V_{BE} for option (i), (ii) and (iii). Although an increasing V_{jC}-V_{BE} with option (i) is shown in Fig. 3.5(a), C_{tC} first mainly decreases with V_{BE} up to 0.8 V due to a reduction of the f_I factor and then C_{tC} increases again because of largely increasing V_{jC} when high injection occurs around V_{BE} = 0.8 V. Without current dependence in V_{junc} and V_{ch}, V_{jC} slowly increases with V_{BE}, so the decreasing f_I factor makes C_{tC} in option (ii) monotonically decrease with V_{BE}. A smaller M_C in option (iii) leads to less decreasing of f_I and then less reduction of C_{tC} at high V_{BE}. Besides the M_C change, τ_B, τ_E are increased to tune back f_T and OIP3 peak. With this new V_{junc} and V_{ch} combination and retuned parameters, $\Im(i_{2,3rd})$ and $|i_{2,3rd}|$ are well modeled, as can be seen from Fig. 3.4(b), leading to the OIP3 peak improvement. At the same time, f_T and C_{BC} are also well modeled. However, a clear difference between measurement and simulation can still be observed on C_{BC}-V_{BE} at $V_{BE} > 0.82$ V.

The individual contribution of various charges are also shown in Fig. 3.6. For each charge Q, f_T is simulated by turning on only that charge, the corresponding transit time is denoted as τ_Q. The total transit time $\tau_T = 1/(2\pi f_T)$ for the V_{junc} and V_{ch} options (i) and (ii) are compared in Fig. 3.6, in blue solid and dashed lines, respectively. The individual contributions are simulated.

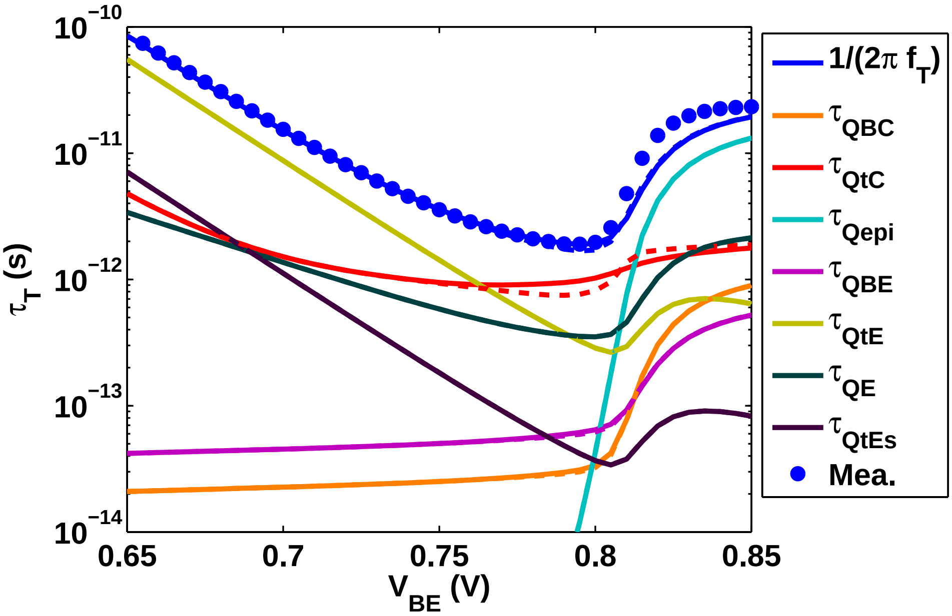

Figure 3.6: Measured and simulated τ_T versus V_{BE}. Individual contribution are simulated using modeling option (i) and (ii). in solid and dashed lines, respectively.

τ_T drops with increasing V_{BE} first, primarily due to τ_{QtE}. In the minimum τ_T (peak f_T) region, τ_{QtC} dominates. The MEXTRAM 504.12 V_{junc} and V_{ch}, i.e. option (i), give a τ_{QtC} that is much more flat at high V_{BE}, due to the use of a current independent epi-layer resistance in calculating

V_{junc} and a V_{ch} that increases with I_C. The C_{tC} value itself is less V_{BE} dependent as well, as shown earlier in Fig. 3.5(a). With $V_{junc} = V_{B_2C_1}$, $V_{ch} = 0.1V_{dC}$, i.e. option (ii), τ_{QtC} continues to decrease, as C_{tC} continues to decrease, as can be seen in Fig. 3.5(a). A smaller M_C reduces the variation of C_{tC} with increasing V_{BE}, as shown for option (iii) in Fig. 3.5(a). This makes τ_{QtC} less V_{BE} dependent at high injection, and helps to reduce f_T back to its desired value. This is confirmed by simulated τ_T for option (iii), but not shown to save space. At $V_{BE} > 0.8$ V, a large increasing τ_T is due to τ_{Qepi}.

The C_{BC} at high V_{BE}, however, remains higher than measurement in Fig. 3.4(a) for option (iii). To understand the reason, C_{BC} is simulated by turning on charges that contribute to C_{BC} individually. The charge symbols follow definitions in MEXTRAM documentation [15]. Fig. 3.7 shows C_{BC} and its contributions for option (iii), i.e. $V_{junc} = V_{B_2C_1}$, $V_{ch} = 0.1V_{dC}$ with

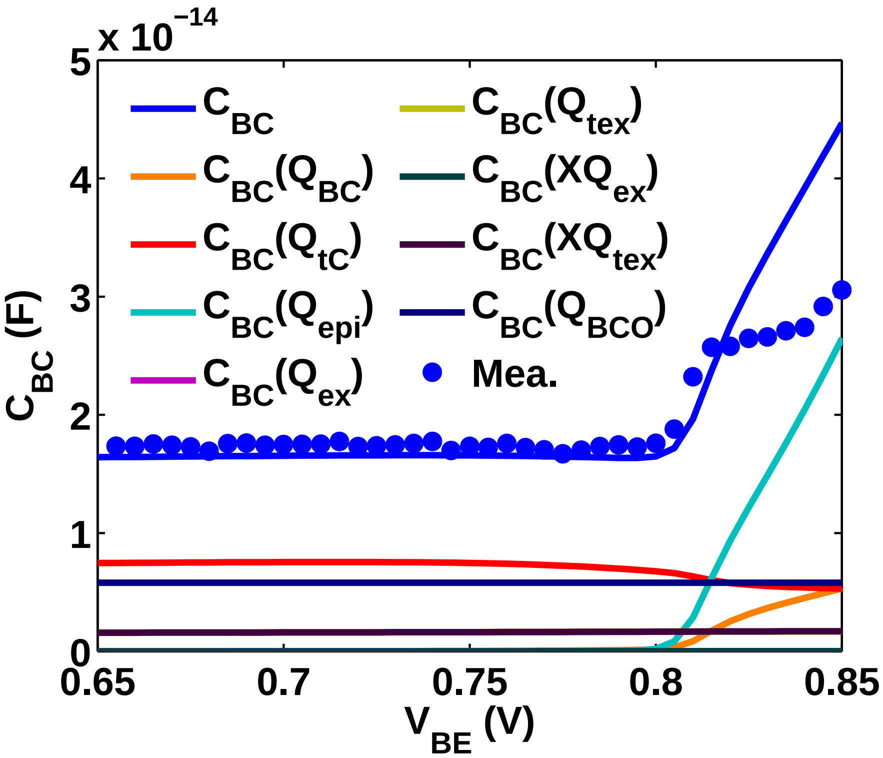

Figure 3.7: C_{BC} and its contributions for option (iii).

retuned parameters. The increasing C_{BC}-V_{BE} at $V_{BE} > 0.8$ V is mainly due to an increasing $C_{BC}(Q_{epi})$, which is used to fit the increase of C_{BC} in the V_{BE} range from 0.8 to 0.82 V. The disadvantage is that $C_{BC}(Q_{epi})$ continues to increase at $V_{BE} > 0.82$ V. We emphasize that at high injection, the contribution of Q_{tC} to C_{BC} differs from C_{tC}, due to important difference between V_{jC} and external V_{BC}. This is illustrated in Fig. 3.8 by comparing $C_{BC}(Q_{tC})$ with C_{tC}, as well as $\partial Q_{tC}/\partial V_{BC}$. $C_{BC}(Q_{tC})$ is from $\Im(Y_{12})$, while $\partial Q_{tC}/\partial V_{BC}$ is from DC simulation. $C_{BC}(Q_{tC})$ agrees with $\partial Q_{tC}/\partial V_{BC}$.

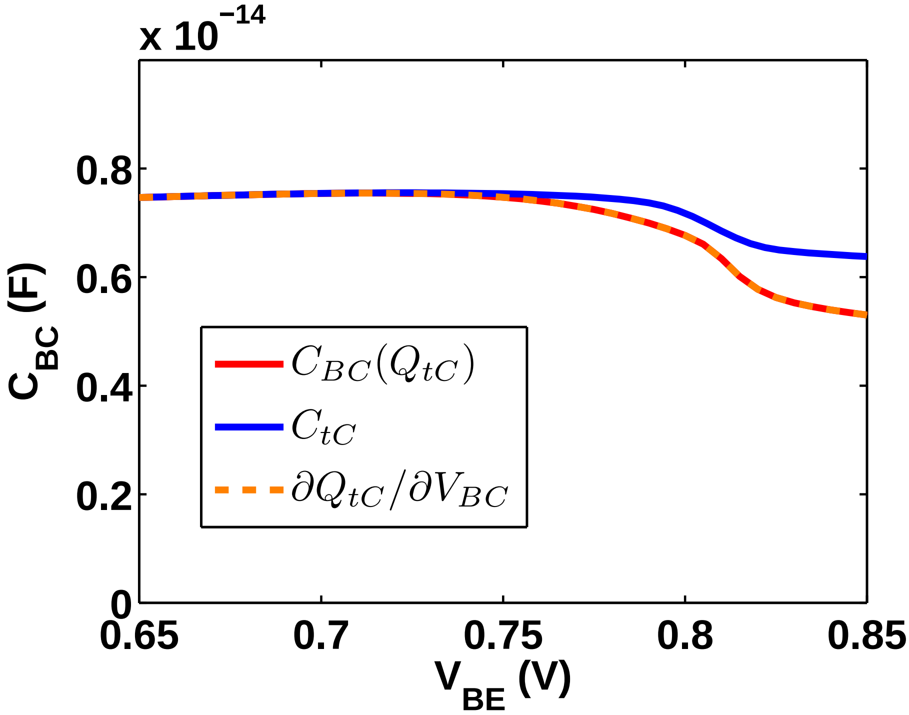

Figure 3.8: Simulated $C_{BC}(Q_{tC})$, C_{tC} and $\partial Q_{tC}/\partial V_{BC}$ versus V_{BE} with modeling option (iii).

3.3 Simultaneous Modeling of IP3 and C_{BC}

We discussed earlier in Section 3.2 that the rise of C_{BC} in the V_{BE} range from 0.8 to 0.82 V in Fig. 3.7 is fitted by a rising $C_{BC}(Q_{epi})$. Problem, however, is $C_{BC}(Q_{epi})$ continues to increase at high V_{BE}, leading to an overestimation of C_{BC}. To solve this problem, we need to decrease $C_{BC}(Q_{epi})$, and produce an increase of C_{BC} only in the range of V_{BE} from 0.8 to 0.82 V. The increase, however, should stop at higher V_{BE}. This is possible through the $C_{BC}(Q_{tC})$ contribution by considering the epi-layer voltage drop in V_{junc}, as was done in option (i), which creates a fast rising V_{jC}, as can be seen from Fig. 3.5(b), but without increasing the transition width V_{ch}, which has been shown to cause distortion problems near IP3 peak.

Fig. 3.9(a) shows C_{tC} obtained using the following modeling options

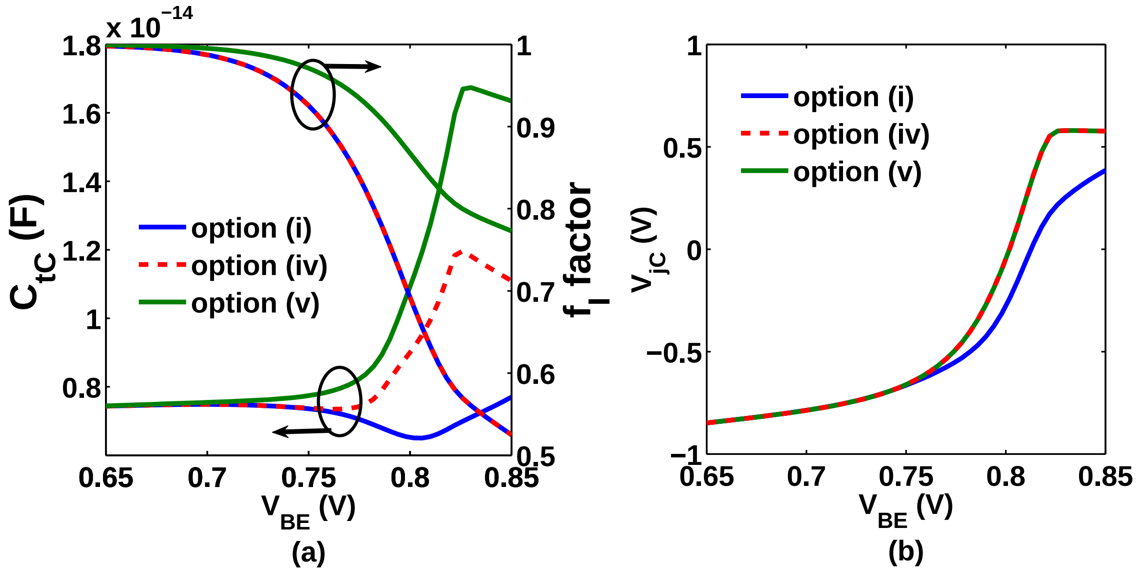

Figure 3.9: V_{BE} dependence of simulated (a) C_{tC} on the left y-axis and f_I factor on the right y-axis and (b) V_{jc} with modeling options (i), (iv) and (v).

(iv) $V_{junc} = V_{B_2C_1} + V_{xi0}$, $V_{ch} = 0.1V_{dC}$ with parameters from Fig. 3.1, including $M_C = 0.99$.

(v) $V_{junc} = V_{B_2C_1} + V_{xi0}$, $V_{ch} = 0.1V_{dC}$ with retuned parameters to refit the overall f_T and OIP3, including $M_C = 0.41$.

The f_I factor is also shown. The C_{tC} and f_I from option (i) are included as well for reference. The V_{jC} behavior is shown in Fig. 3.9(b). Compared to option (i), V_{jC} rises faster and saturates more abruptly due to V_{ch} being fixed at $0.1V_{dC}$, as we intended. This largely stops the rise of C_{tC} at high V_{BE}. Observe the rise of C_{tC} around $V_{BE} = 0.82$ V followed by a slight decrease. A small decrease is produced by decreasing the f_I factor through the M_C parameter, which offsets the increase of $C_{BC}(Q_{epi})$ and $C_{BC}(Q_{BC})$.

Fig. 3.10(a) shows OIP3, f_T and C_{BC} obtained using option (iv), in dashed lines and option (v), in solid lines. The epi-layer transit time τ_{epi} is reduced for option (v) than for option (iv). The initial rise of C_{BC} for option (v) is now mainly due to $C_{BC}(Q_{tC})$ as opposed $C_{BC}(Q_{epi})$ for option (iv). The C_{BC} at $V_{BE} > 0.82$ V for option (v) shows a plateau followed by another rise, which fits measurement much better. Fig. 3.10(b) shows $|i_{2,3rd}|$, $\Re(i_{2,3rd})$, $\Im(i_{2,3rd})$ versus V_{BE} using option (v). Besides a good fitting of $\Im(i_{2,3rd})$ and thus $|i_{2,3rd}|$, $\Im(i_{2,3rd})$ at $V_{BE} <$ 0.75 V is also better fitted.

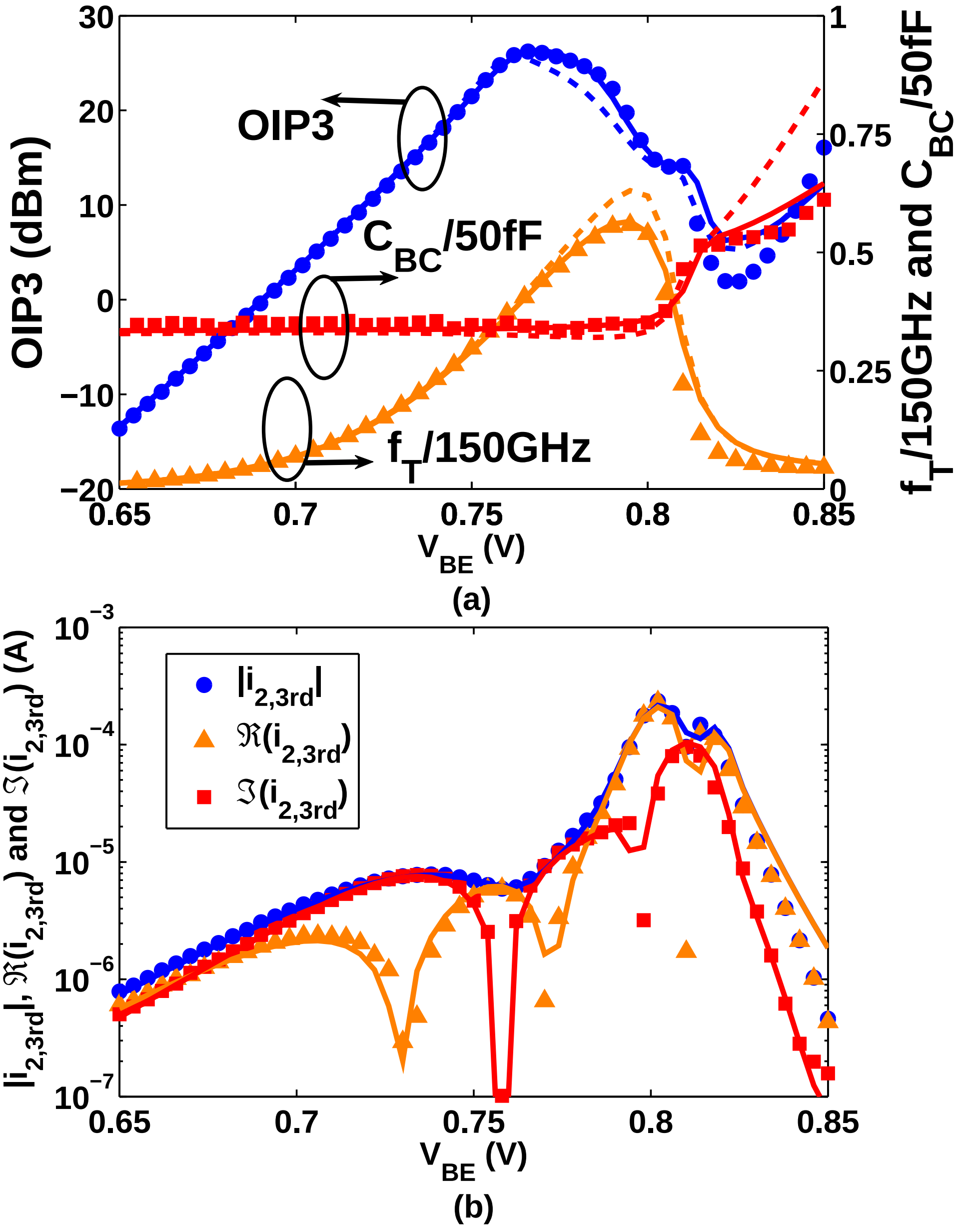

Figure 3.10: V_{BE} dependence of (a) OIP3, f_T, C_{BC} and (b) $|i_{2,3rd}|$, $\Re(i_{2,3rd})$, $\Im(i_{2,3rd})$ with $V_{junc} = V_{B_2C_1} + V_{xi0}$, $V_{ch} = 0.1V_{dC}$.

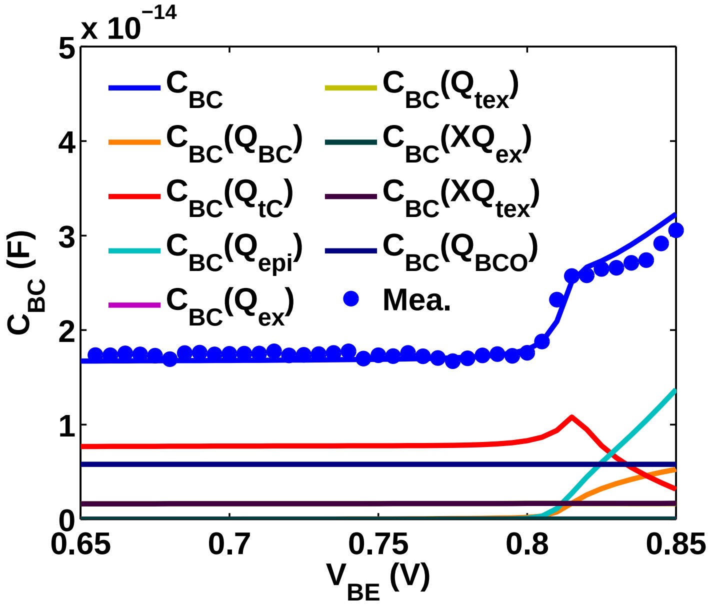

Figure 3.11: C_{BC} and its contributions for modeling option (v) versus V_{BE}.

Fig. 3.11 shows C_{BC} and its contributions for option (v), i.e. $V_{junc} = V_{B_2C_1} + V_{xi0}$, $V_{ch} = 0.1V_{dC}$ with retuned parameters. As V_{BE} increases from 0.8 to 0.82 V, V_{xi0} and V_{junc} increase fast, as was shown in Fig. 3.9(b), causing $C_{BC}(Q_{tC})$ to increase. Such an increase allows the use of a smaller τ_{epi}, which decreases $C_{BC}(Q_{epi})$. At $V_{BE} > 0.82$ V, $C_{BC}(Q_{tC})$ decreases, due to a decreasing C_{tC}, as discussed in Fig. 3.9(a). Overall, this produces the plateau of the overall C_{BC}.

Chapter 4

Avalanche modeling

Avalanche multiplication is important for modeling of safe operation area (SOA) [31], transistor output characteristics, and linearity [13]. Many M-1 models of different complexity exist [31], [32], [33], [34], [35], [36]. The model of [31] has temperature dependence and current dependence, but was mainly developed for strong avalanche near breakdown with a simplicity suitable for analytical SOA modeling.

4.1 Limitation of Previous Avalanche Models

The common-base SiGe HBT works at both high V_{CB} and I_E even beyond beyond peak f_T, which put stringent requirement on accuracy of avalanche modeling. Avalanche multiplication factor (M-1) model affects safe operation area (SOA) [37], transistor output characteristics and linearity [38] [39]. However, previously many M-1 models [40] [41] [42] [43] generally cannot be applied at such high current where high injection effect occurs, which leads an increasing M-1 with increasing I_E.

Fig. 4.1 shows measured and simulated I_B-I_E up to 150 mA at V_{CB} = 1, 2 and 3 V. The simulated I_B are made by using avalanche models from MEXTRAM 504.12 [15], MEXTRAM 505.00 [1] and [3], respectively. The device details will be given in Secion 4.2. A clear decreasing I_B at I_E larger than 100 mA is due to Kirk effect, which makes M-1 increase with increasing I_E. However, none of the models can get a good fitting of I_B-I_E, although Kirk effect has been considered in MEXTRAM 504 and [3]. A comprehensive avalanche multiplication compact model [44] including high current effect is in MEXTRAM 504 [15]. However, with only two parameters W_{AVL} and V_{AVL} provided, I_B-I_E at V_{CB} = 2 V are not fitted well

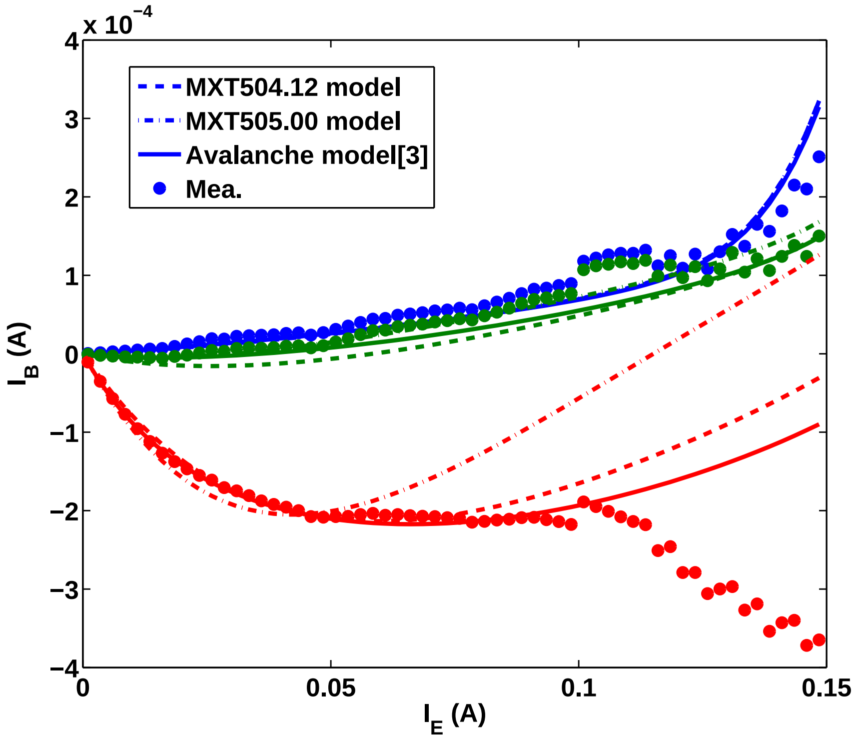

Figure 4.1: Measured and simulated I_B-I_E up to 150 mA at V_{CB} = 1, 2 and 3 V. The simulated I_B are results of using avalanche models from MEXTRAM 504.12, MEXTRAM 505.00 and [3].

even at $I_E < 50$ mA, in dashed lines of Fig. 4.1. Although an additional parameter SFH is provided to consider crowding effect at high current when EXAVL = 1, as described by Eqn. (2.49)-(2.58) in Chapter 2, the high injection parameters in avalanche model have a coupling difficulty with main current, which largely limits M-1 fitting accuracy at high current. A semi-empirical avalanche model [25] in Mextram 505 presents an improved fitting accuracy for M-1 dependence on both V_{CB} and I_E at low current. However, the empirical current dependent term with I_{TOavl} at low current makes it hard to take high injection effect into consideration, as the simulated I_B starts to deviate from measurement at medium current $I_E > 50$ mA, shown in dotted lines of Fig. 4.1. Recently a closed-form analytical expression for M-1 including high current effect is derived in [3]. However, the square root relation made in [3](12) will lead to clear limitation of M-1 fitting at high current, as shown in solid lines of Fig. 4.1. Moreover, [3] does not present a method to extract M-1 without the effect of self-heating at high current. In the following, a new method to extract M-1 at high current will be presented and an extended formulation based on [25] to include high current effect will be derived. Both V_{CB} and I_E dependence of the extracted M-1 will be verified in an advanced SiGe HBT technology. Instead of empirically considering current dependence, as was done in MEXTRAM 505.00, the new extended avalanche model physically derives current dependence of M-1 including Kirk effect.

4.2 Measurement and Extraction of M-1

A 0.4×7.8×20 μm^2 SiGe HBT from QUBiC4Xi technology is used [28]. The peak f_T is 84 GHz. Peak f_{max} is 162 GHz, and a BV_{CBO} is 12 V. I_B on this RF structure is calculated from measured I_C and I_E, which has been shown in Fig. 4.1. Another device with 0.5×20.7 μm^2 from the same technology on a DC structure is used.

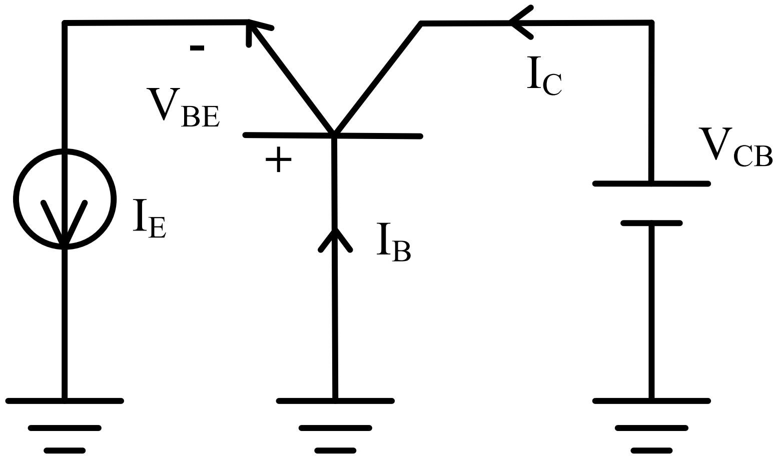

Figure 4.2: A schematic for forced-I_E with V_{CB} on a transistor of common-base configuration.

Fig. 4.2 shows a forced-I_E setup with V_{CB} on a transistor of common-base configuration. With forced I_E at emitter and sweeping V_{CB}, a forced-I_E technique [45] is used to allow a safe extraction of M-1 at higher V_{CB} and I_E than the conventional forced-V_{BE} method [46].

Under forced-I_E, M-1 in [46] [47] [48] [49] is extracted as

$$M - 1 = \frac{I_{AVL}}{I_{CnoAV}} = \frac{I_C}{I_E - I_B(I_E)|_{V_{CB}=0}} - 1, \tag{4.1}$$

where I_{CnoAV} is the collector current without avalanche effect. $I_B(I_E)|_{V_{CB}=0}$ is the measured I_B at the same I_E and V_{CB} = 0 V. Although (4.1) can have a good evaluation of M-1 at sufficiently low I_E, M-1 is overestimated at high I_E due to negligence of Early effect and self-heating effect. Another M-1 extraction including Early effect was proposed in [45]

$$M - 1 = \frac{I_C}{I_E - I_{B1}} - 1, \tag{4.2}$$

where $I_{B1} \approx I_B$(V_{BE}=V_{BE},V_{CB}=0) and I_{B1} is found from I_B-V_{BE} curve with V_{CB} = 0 V, using the V_{BE} value measured at each V_{CB}. However, as I_E goes up and self-heating effect becomes significant, the accuracy will decrease. In order to extract M-1 at high current when Kirk effect occurs, self-heating effect should be accurately considered and excluded to extract actual M-1. To accurately account for self-heating effect that affects I_{B1} calculation, I_B-V_{BE} at V_{CB} = 0 V should be fitted first in some reasonably wide temperatures. Self heating resistance R_{th} is also extracted. We propose to extract M-1 from a compact model that is able to fit above

$$M - 1 = \frac{I_C}{I_E - I_{B0.s}} - 1, \tag{4.3}$$

where $I_{B0,s}$ is the simulated base current under the same I_E and V_{CB} after temperature scaling of base current has been accurately extracted. Fig. 4.3 shows extracted M-1 versus I_E from different method at V_{CB} = 3 V. The simulated M-1 using the model of [3] is also shown. Due to negligence of both Early effect and self-heating, M-1 extracted using (4.1) is largely overestimated at high $I_E > 100$ mA. Compared to (4.3), M-1 extracted using (4.2) can still provide a good approximation even with large self-hating effect at high current due to high enough current gain. Due to high injection effect, the M-1 extracted using (4.3) starts to rise up at around 100 mA. When high injection occurs, the maximum of electrical field will relocate to epi-layer/ buried layer interface and increase with rising I_E, which directly cause M-1 to increase at high current. However, M-1 at high currents cannot be well fitted by model of [3], which directly results in deviation of I_B-I_E at high current seen in Fig. 4.1. Instead of using

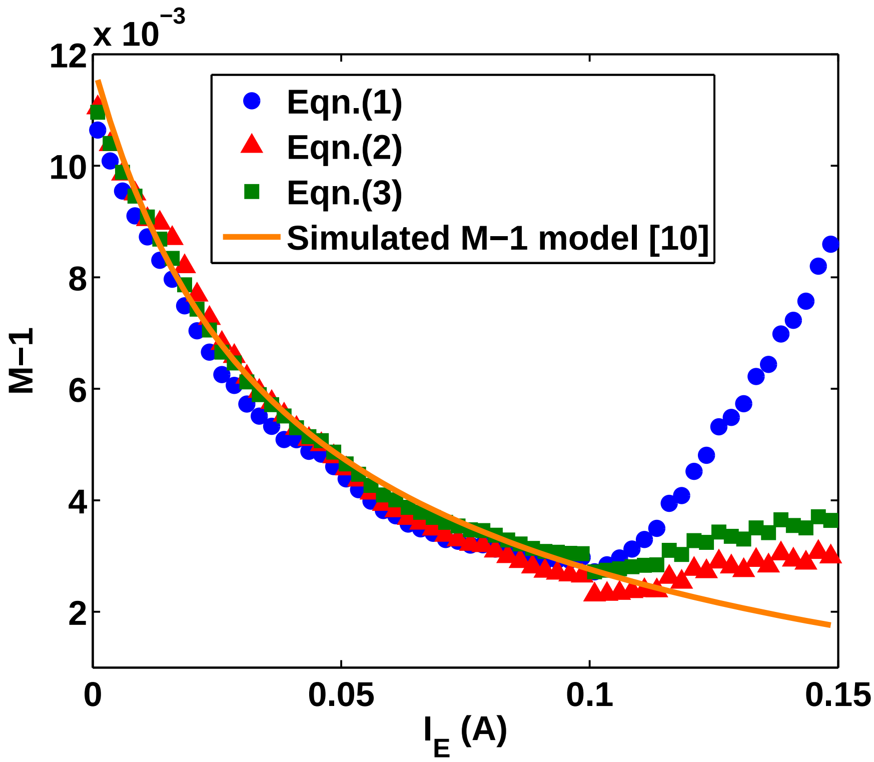

Figure 4.3: Different extraction of M-1 versus I_E at V_{CB} = 3 V. The simulated M-1 using model [3] is also shown.

empirical current relation, a new extended avalanche model based on [25] will be derived in the following section, to fit data at both low and high currents.

4.3 New Current Dependence M-1 Formulation

A basic form of M-1 can be derived by integration of ionization coefficient from Chynoweth's empirical law over CB depletion width [50]

$$M - 1 = \frac{a}{b} x_d E_M \exp\left(-\frac{b}{E_M}\right). \tag{4.4}$$

where a and b are material dependent constants of impact ionization coefficients dependent on electric field. x_d is CB depletion width. E_M is maximum electric field of CB junction. Related to CB depletion capacitance C_{jC} [40], the product of $x_d \cdot E_M$ can be approximated by

$$x_d \cdot E_M = \frac{V_{DC} - V_{B_2C_1}}{1 - P_C}, \tag{4.5}$$

where V_{DC} is built-in potential. $V_{B_2C_1}$ is intrinsic voltage drop over CB depletion junction. P_C is junction grading coefficient. In order to derive current dependence of M-1, the current dependence of CB depletion junction should be considered from low to high current below.

4.3.1 M-1 at low current

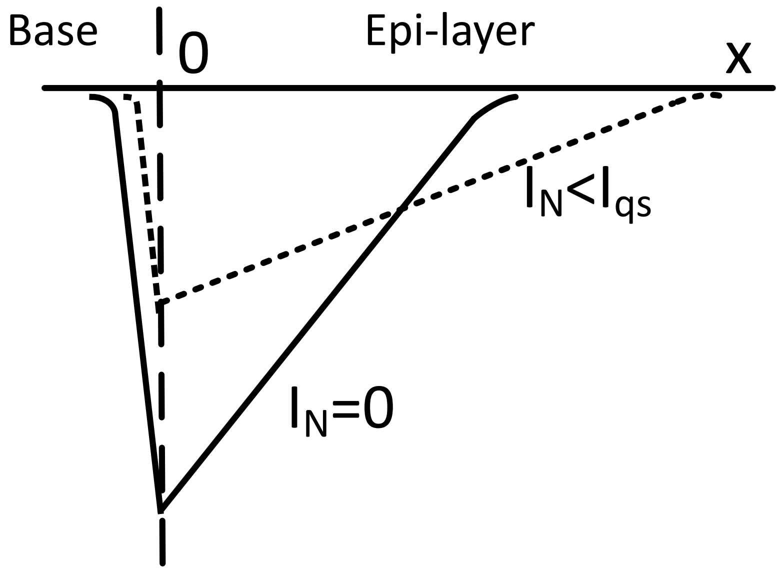

Figure 4.4: A diagram of current change on electrical field distribution at low current, before onset of quasi-saturation.

Fig. 4.4 shows the effect of current on electrical field distribution at low current. I_{qs} denotes the current when quasi-saturation occurs. With an increase of current, the slope of electrical field in epi-layer is modulated. From Poisson's equation,

$$\frac{dE}{dx} = \frac{qN_{epi}}{\varepsilon_{Si}}\left(1 - \frac{n}{N_{epi}}\right), \tag{4.6}$$

where q is electron charge, ε_{Si} is permittivity of Si, N_{epi} is epi-layer doping density, n is electron density in the epi-layer. Assuming velocity saturation, as electrical field is high enough for impact ionization, (4.6) can by expressed by

$$\frac{dE}{dx} = \frac{qN_{epi}}{\varepsilon_{Si}}\left(1 - \frac{I_N}{I_{hc}}\right), \tag{4.7}$$

where I_N is main current. $I_{hc} = qN_{epi}v_{sat}A_E$ is hot-carrier current. Under low current condition when epi-layer is not fully depleted, we also find

$$\frac{dE}{dx} = \frac{E_M}{x_d}, \tag{4.8}$$

So E_M can be solved by (4.5), (4.7) and (4.8)

$$E_M = \sqrt{\frac{qN_{epi}}{\varepsilon_{Si}(1-P_C)}(V_{DC} - V_{B_2C_1})} \cdot \sqrt{1 - \frac{I_N}{I_{hc}}}. \tag{4.9}$$

By bringing (4.5) and (4.9) into (4.4), then current dependence of M-1 can be formulated as

$$\begin{aligned} M - 1 =& \frac{a}{b(1-P_C)} \cdot (V_{DC} - V_{B_2C_1}) \exp\left[- \sqrt{\frac{\varepsilon_{Si}(1-P_C)}{qN_{epi}}} \right. \\ & \left. \cdot\, b(V_{DC} - V_{B_2C_1})^{-1/2} \cdot \left(1 - \frac{I_N}{I_{hc}}\right)^{-1/2} \right]. \end{aligned} \tag{4.10}$$

The following parametrizations are taken after an inspection of (4.10)

- $\phi = V_{DCavl} - V_{B_2C_1}$. V_{DCavl} is CB built-in potential dedicated for avalanche modeling, to distinguish from V_{DC} used in CB depletion capacitance or epi-layer modeling.
- I_{hcavl} = I_{hc} as model parameter of hot-carrier current for avalanche, distinguished with I_{hc} used in epi-layer model.
- B_{avl} = $\sqrt{\frac{\varepsilon_{Si}(1-P_C)}{qN_{epi}}} \cdot b$. B_{avl} is calculated from material constant b varying with temperature. So B_{avl} dominates temperature dependence of M-1, as proposed in [25].
- A_{avl} = $\sqrt{\frac{\varepsilon_{Si}}{qN_{epi}(1-P_C)}} \cdot a$. A_{avl} is calculated from material constant a, which will provide extra degree of freedom in fitting as treated as model parameter.
- The exponents -1/2 in the two exponential terms will be treated as model parameters C_{avl} and C_{avl2}, separately. Because the approximations made in (4.5) and (4.7) are uniform doping and carrier velocity, which will not be always the case in reality.

With these considerations, a new current dependence of M-1 at low current is obtained

$$M - 1 = \frac{A_{avl}}{B_{avl}}\phi \cdot \exp\left[-B_{avl} \cdot \phi^{C_{avl}} \left(1 - \frac{I_N}{I_{hcavl}}\right)^{C_{avl2}}\right], \tag{4.11}$$

and

$$\phi = V_{DCavl} - V_{B_2C_1}, \tag{4.12}$$

where A_{avl}, B_{avl}, V_{DCavl}, C_{avl} and C_{avl2} are model parameters.

4.3.2 M-1 at high current

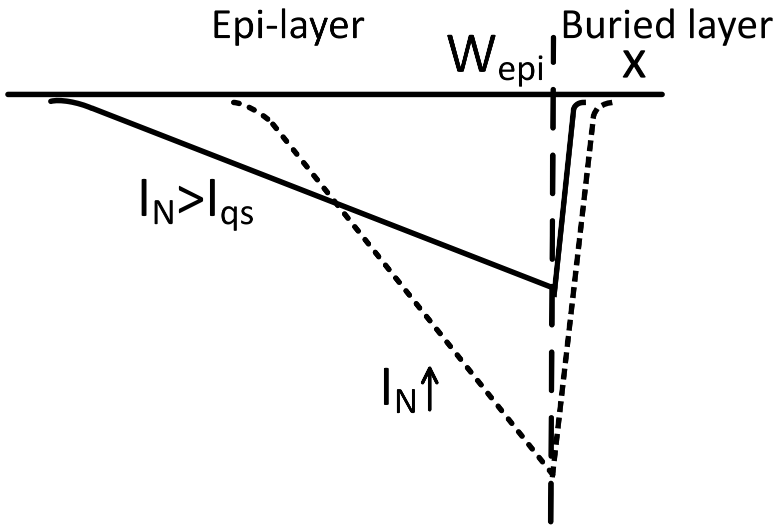

Figure 4.5: A diagram of current change on electrical field distribution at high current.

Fig. 4.5 shows the effect of current on electrical field distribution at high current when $I \gg I_{qs}$. When Kirk effect occurs, electron density becomes larger than the epi-layer doping, the slope of electrical field will be negative as in (4.6) and the maximum electrical field occurs at the boundary between epi-layer and buried layer. An further increase of current will decrease the slope of electrical field. However, the maximum electrical field will increase. We find (4.8) can be still approximately applied at such high current but only with negative sign of dE/dx

$$\frac{dE}{dx} = -\frac{E_M}{x_d}, \tag{4.13}$$

Bringing (4.5), (4.7) and (4.13) into 4.4, a current dependence of M-1 at high current can be derived

$$\begin{aligned} M-1 =& \frac{a}{b(1-P_C)} \cdot (V_{DC}-V_{B_2C_1}) \exp\Bigg[-\sqrt{\frac{\varepsilon_{Si}(1-P_C)}{qN_{epi}}} \\ & \cdot b(V_{DC}-V_{B_2C_1})^{-1/2} \cdot \left(\frac{I_N}{I_{hcavl}}-1\right)^{-1/2}\Bigg]. \end{aligned} \tag{4.14}$$

Following the same parametrization strategy as in low current, we obtain for $I_N \gg I_{hcavl}$

$$\begin{aligned} M-1 =& \frac{A_{avl}}{B_{avl}}\phi \cdot \exp\left[-B_{avl}\cdot\phi^{C_{avl}}\left(\frac{I_N}{I_{hcavl}}-1\right)^{C_{avl3}}\right] \\ \approx& \frac{A_{avl}}{B_{avl}}\phi \cdot \exp\left[-B_{avl}\cdot\phi^{C_{avl}}\left(\frac{I_N}{I_{hcavl}}\right)^{C_{avl3}}\right] \end{aligned}, \tag{4.15}$$

where C_{avl3} is new model parameter for high current dependence of M-1.

4.3.3 M-1 at all currents

(4.11) can only applied for low current when $I_N \ll I_{hc}$ and CB junction are not fully depleted. (4.15) can only applied for high current when $I_N \gg I_{hc}$ and electrical neural base has pushed out. To combine (4.11) and (4.15) together, we propose

$$\begin{aligned} M-1 =& \frac{A_{avl}}{B_{avl}} \cdot \phi \cdot \exp\Bigg[-B_{avl}\cdot\phi^{C_{avl}} \\ & \cdot \left(1-\frac{I_{cap}}{I_{hcavl}}\right)^{C_{avl2}} \cdot \left(\frac{I_{cc}}{I_{hcavl}}\right)^{C_{avl3}}\Bigg], \end{aligned} \tag{4.16}$$

where I_{cap} is a limiting current to be always lower than I_{hcavl} at all I_N [15]

$$I_{cap} = \frac{I_N I_{hcavl}}{I_N + I_{hcavl}}. \tag{4.17}$$

I_{cap} approaches to I_N when $I_N \ll I_{hcavl}$ and approaches to I_{hcavl} when $I_N \gg I_{hcavl}$. So $(1 - I_{cap}/I_{hcavl})^{C_{avl2}}$ term is used for low current fitting. The exponential term $(I_{cc}/I_{hcavl})^{C_{avl3}}$ is used for medium and high current fitting. So (I_{cc}/I_{hcavl}) should be close to 1 at low current to keep low current fitting not affected. I_{cc}/I_{hcavl} is a smoothly limiting function of I_N

$$\frac{I_{cc}}{I_{hcavl}} = 1 + \epsilon \cdot \ln\left\{1 + \exp\left[\frac{1}{\epsilon}(\frac{I'_N}{I_{hcavl}} - 1)\right]\right\}, \tag{4.18}$$

and

$$I'_N = I_N - \Delta I, \tag{4.19}$$

where ϵ is smoothing parameter. I'_N is I_N with an offset parameter ΔI to allow setting width of medium current range between low and high current.

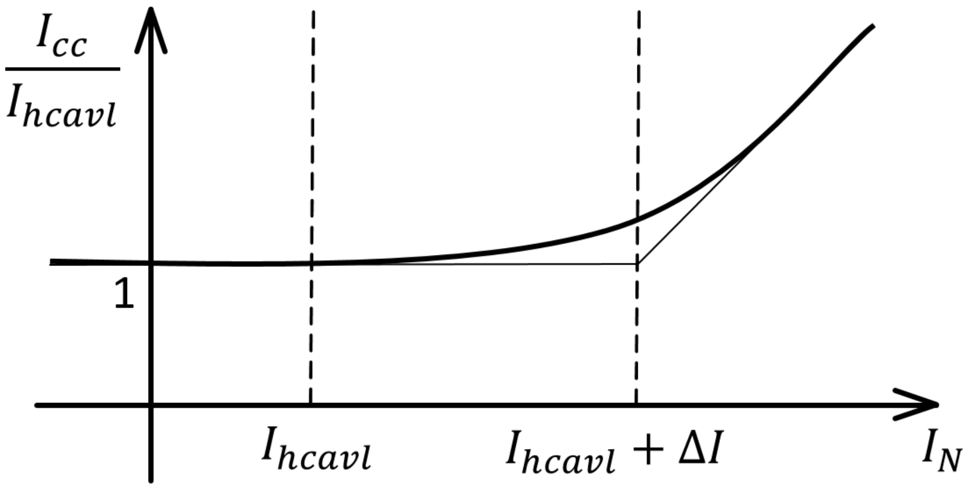

Figure 4.6: A diagram of I_{cc}/I_{hcavl}-I_N from low to high current.

Fig. 4.6 shows a diagram of I_{cc}/I_{hcavl}-I_N from low to high current. For $I_N < I_{hcavl}$, I_{cc}/I_{hcavl} approaches to 1 and $(I_{cc}/I_{hcavl})^{C_{avl3}}$ becomes 1, (4.16) becomes (4.11). For $I_N \gg I_{hcavl}$, I_{cc} equals $I_N - \Delta I$ and $(I_{cc}/I_{hcavl})^{C_{avl3}}$ dominates in the exponential term, (4.16) approximately becomes (4.15) and the difference between -1 and $-\Delta I/I_{hcavl}$ can be neglected due to $I_N \gg I_{hcavl}$. ϵ and ΔI are used to adjust transition between low and high current range. So a complete current dependence of avalanche modeling is expressed by (4.12), (4.16), (4.17), (4.18) and (4.19). Due to the reversal of the slope of electrical field, the maximum of electrical field moves to the interface of epi-layer and buried layer, the compact model becomes complex and may numerically be unstable. So a flag parameter EXAVL is included in compact model. When EXAVL = 1, the complete extended avalanche model will be used. When EXAVL = 0, then no high injection effect will be modeled.

For parameter extraction strategy, A_{avl}, B_{avl}, C_{avl}, V_{DCavl} should be extracted for V_{CB} dependence of M-1 at extremely low current. I_{hcavl} and C_{avl2} are then extracted for current dependence of M-1 up to medium current. ΔI, ϵ are extracted for transition from medium to high current. C_{avl3} is extracted for M-1 at high current when M-1 rises with increasing current.

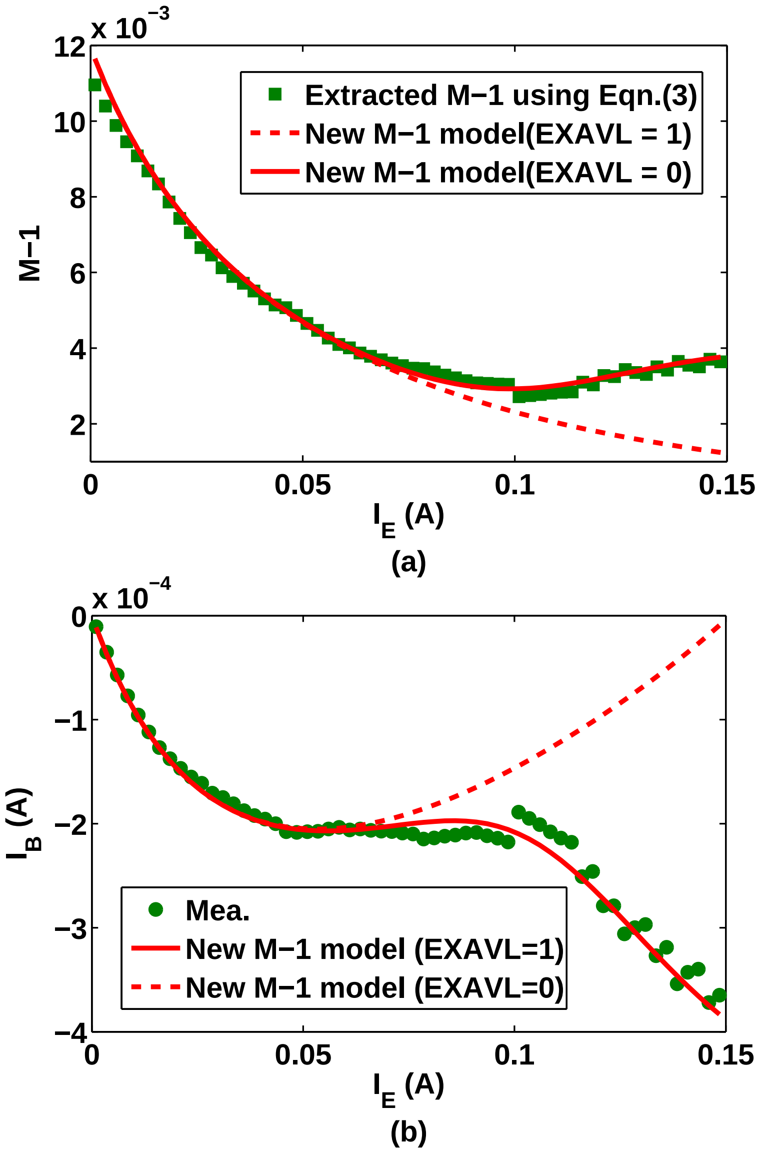

Figure 4.7: (a) Extracted and new avalanche model simulated M-1 versus I_E at V_{CB} = 3 V. (b) Measured and simulated I_B-I_E at V_{CB} = 3 V. The dashed lines are simulations without high injection effect.

Fig. 4.7(a) shows extracted M-1 using (4.3) and simulated M-1 using new extended avalanche model versus I_E at V_{CB} = 3 V. With EXAVL = 0, M-1 monotonically decreases with increasing current. A good fitting of M-1 versus I_E up to 150 mA can be obtained only when high injection effect considered (EXAVL = 1). The difference between EXAVL = 0 and 1 implies that high injection occurs at I_E around 60 mA, before M-1 shows a clear increase. Fig. 4.7(b) shows measured and simulated I_B versus I_E using new extended avalanche model at V_{CB} = 3 V. I_B-I_E can be well fitted as extracted M-1 matches well with simulated M-1 in Fig. 4.7(a). So (4.3) provides an accurate extraction of M-1 even at high current.

The new proposed avalanche model can be directly implemented in compact model. The following simulated results are made by new avalanche model incorporated into an experimental version of MEXTRAM 505.

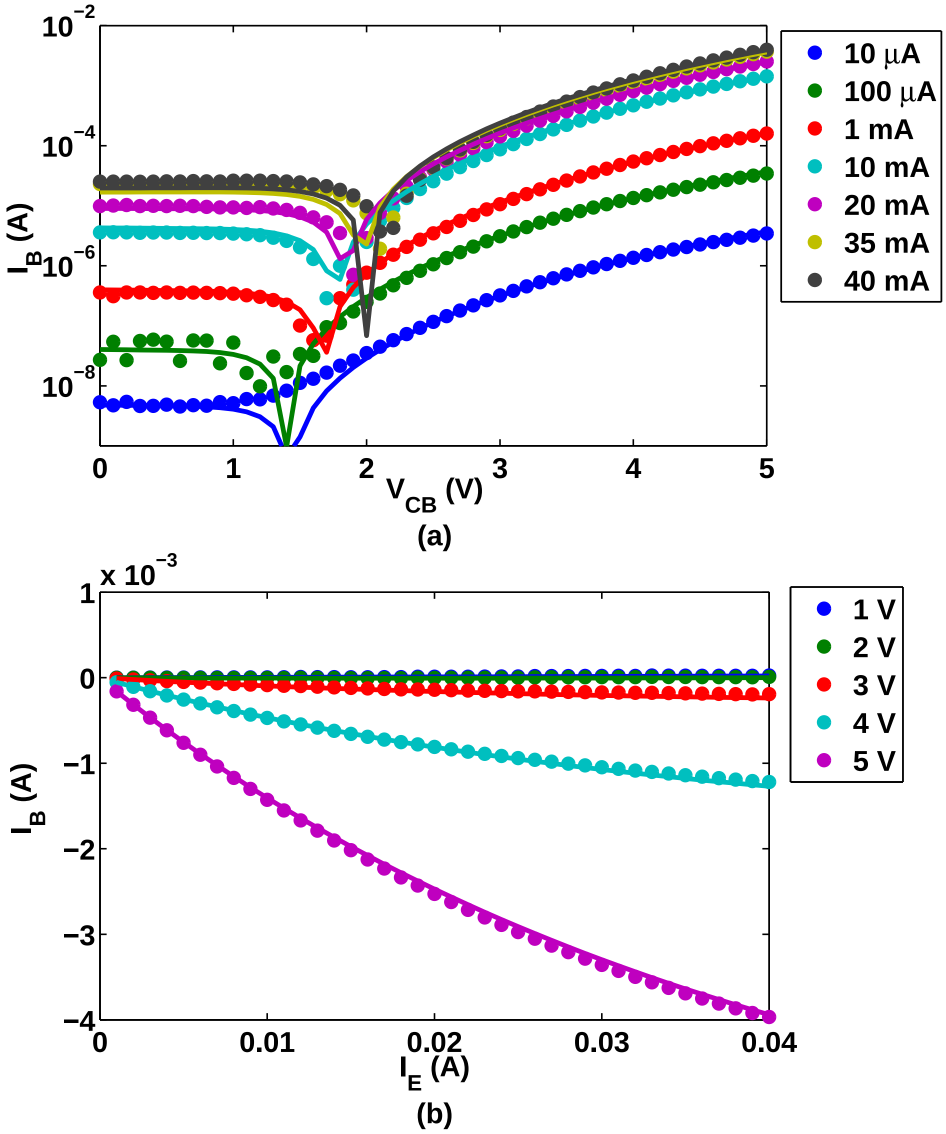

Figure 4.8: Measured (symbols) and new avalanche model simulated (lines) (a) I_B-V_{CB} at I_E from 10 μA to 40 mA and (b) I_B-I_E at V_{CB} from 1 to 5 V.

Fig. 4.8(a) shows measured and new avalanche model simulated I_B-V_{CB} at I_E from 10 μA to 40 mA. Fig. 4.8(b) shows measured and new avalanche model simulated I_B-I_E at V_{CB} from

1 to 5 V. So the new avalanche model provide a good fitting of both V_{CB} and I_E dependence of I_B up to 40 mA of I_E.

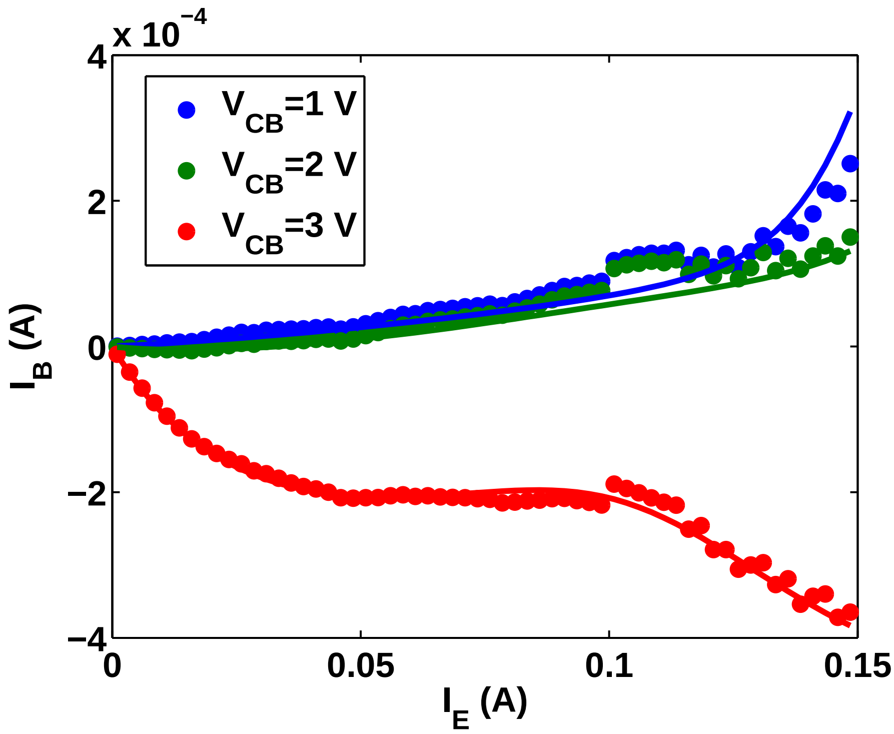

Figure 4.9: Measured (symbols) and new avalanche model simulated (lines) I_B-I_E up to 150 mA at V_{CB} from 1 to 3 V.

Fig. 4.9 shows measured and new avalanche model simulated I_B-I_E up to 150 mA at V_{CB} from 1 to 3 V. Based on an accurate extraction of M-1 in Fig. 4.7, a good fitting of I_B-I_E can be obtained from low to high current at each V_{CB}.

In order to testify the accuracy of new M-1 extraction method and new extended avalanche model, I_B-V_{CB} under forced I_E from low to high current are measured on a 0.5×20.7×1 μm^2 in a DC test structure from the same technology.

Fig. 4.10 shows measured and simulated I_B-V_{BE} at V_{CB} = 0 V are well fitted at multiple temperatures. So temperature scaling of base current is well simulated, which can be used as a good evaluation of base current under different bias without avalanche effect.

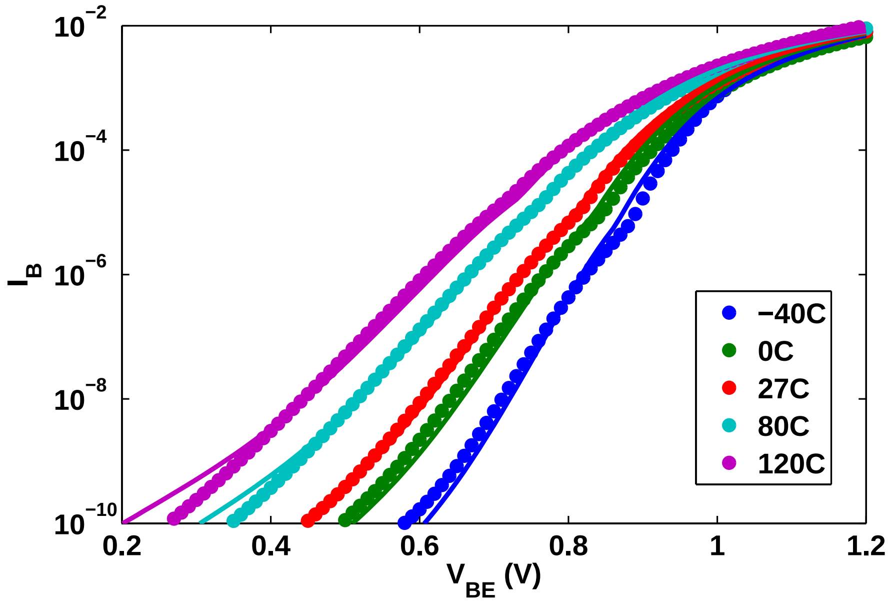

Figure 4.10: Measured(symbols) and simulated(lines) I_B-V_{BE} at V_{CB} = 0 V are well fitted at multiple temperatures.

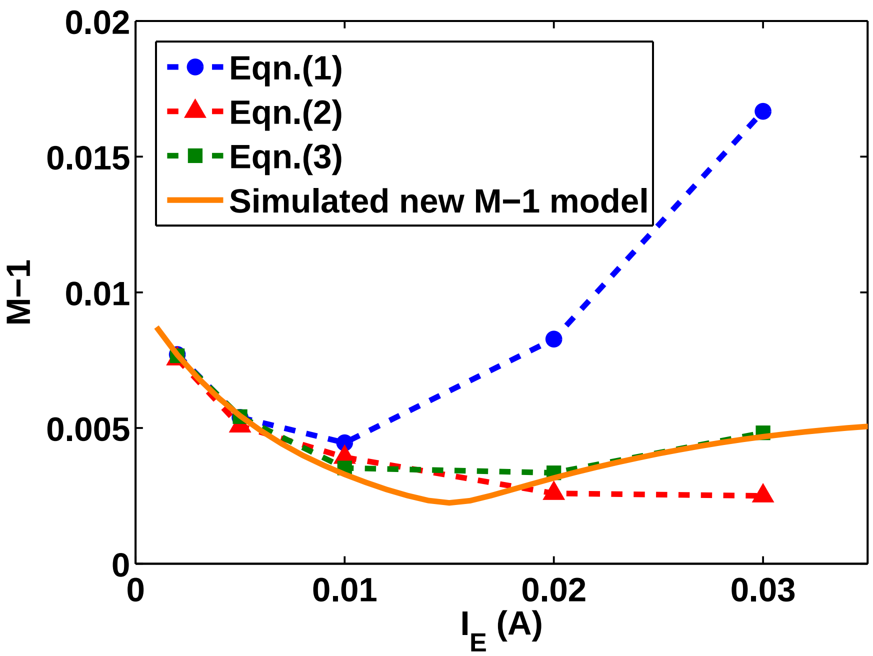

Figure 4.11: A comparison of different M-1 extraction at V_{CB} = 3 V and at I_E from 2 to 30mA. The solid line is simulated M-1 using new extended avalanche model.

Fig. 4.11 shows a comparison of different M-1 extraction at V_{CB} = 3 V and at I_E from 2 to 30mA. The lines are simulated M-1 using new extended avalanche model. At low $I_E < 10$ mA, all three methods give the same extracted M-1. Without considering Early effect, the M-1 from (4.1) becomes much higher with increasing I_E, especially for remarkable self-heating of base current at high current. (4.2) gives much more accurate approximation of M-1 until self-heating takes much effect at high $I_E > 10$ mA. As self-heating is well considered, a clear increase of M-1 from (4.3) at high I_E is due to high injection effect, which is also well fitted by new avalanche model in solid line.

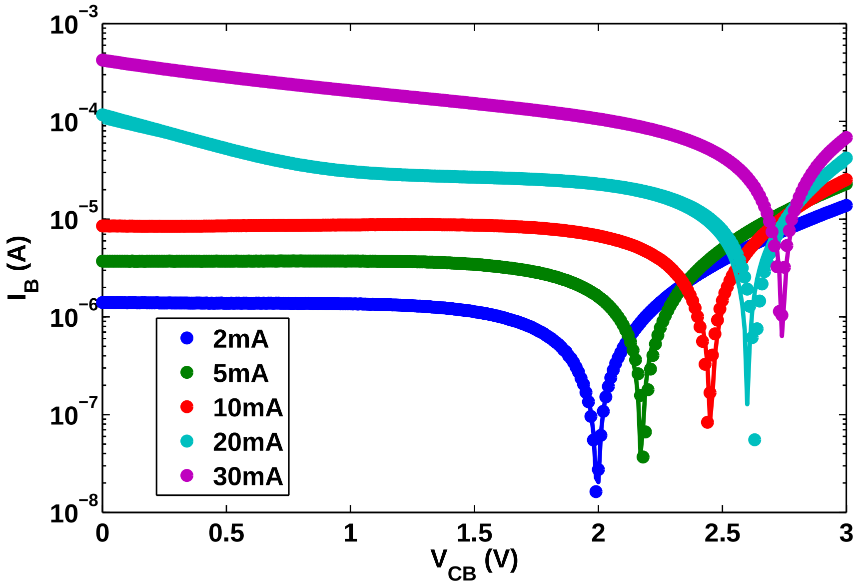

Figure 4.12: Measured (symbols) and new avalanche model simulated (lines) I_B-V_{CB} at I_E from 2 to 30 mA. The same M-1 as solid line of Fig. 4.11 is used.

Fig. 4.12 shows measured and new avalanche model simulated I_B-V_{CB} at I_E from 2 to 30 mA using the simulated M-1 in solid line of Fig. 4.11. The new avalanche model can accurately model high injection effect at high current with a good fitting of (M-1) versus I_E from new extraction method.

Chapter 5

Volterra series Implementation of Mextram

Volterra series describes nonlinear system in a way that is similar to the approximation of an analytical function with a Taylor series: small excursions around an operating point can be described with very few terms of a Volterra series [4]. A nonlinear system which is excited by a signal with small amplitude can be described by a Volterra series which can be broken down after the first few terms. The higher the input amplitude, the more terms of that series need to be taken into account in order to describe the system behavior properly. For very high amplitudes, the series diverges, just as Taylor series. This is often due to occurrence of a strong nonlinearity at high amplitude levels. Hence, Volterra series is only suitable for the analysis of weakly nonlinear circuits.

5.1 Volterra Series in Time and Frequency Domain

Fig. 5.1 shows operators in the block-diagram representation. $\boldsymbol{H_1}$, $\boldsymbol{H_2}$, ..., $\boldsymbol{H_n}$ represents an operator of order 1, 2, ..., n respectively. Each operator is described either in the time domain or in the frequency domain with a kind of transfer function, called a Volterra kernel. The relationship between the output $y(t)$ and the input $x(t)$ can be expressed by [4]

$$y(t) = \boldsymbol{H_1}[x(t)] + \boldsymbol{H_2}[x(t)] + ... + \boldsymbol{H_n}[x(t)] + ... \tag{5.1}$$

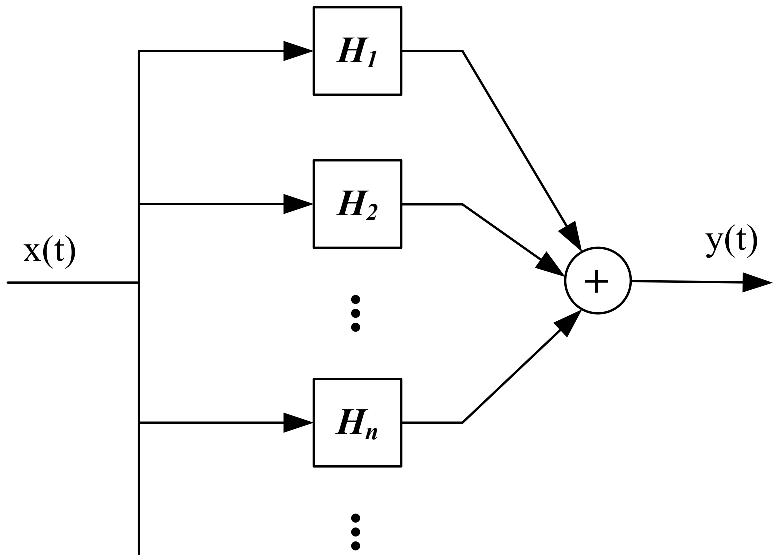

Figure 5.1: Schematic representation of a system characterized by a Volterra series [4].

in which

$$\boldsymbol{H_n}[x(t)] = \int_{-\infty}^{+\infty} \cdots \int_{-\infty}^{+\infty} h_n(\tau_1, \tau_2, \ldots, \tau_n) x(t-\tau_1) x(t-\tau_2) \cdots x(t-\tau_n) d\tau_1 d\tau_2 \ldots d\tau_n, \tag{5.2}$$

where $h_n(\tau_1, \tau_2, \ldots, \tau_n)$ is an nth-order Volterra kernel. The relationship between the input $x(t)$ and the output $y(t)$ of a nonlinear, time invariant system can, be expressed with the following series

$$\begin{aligned} y(t) = & \int_{-\infty}^{+\infty} h_1(\tau_1) x(t-\tau_1) d\tau_1 \\ & + \int_{-\infty}^{+\infty} \int_{-\infty}^{+\infty} h_2(\tau_1, \tau_2) x(t-\tau_1) x(t-\tau_2) d\tau_1 d\tau_2 \\ & \cdots + \int_{-\infty}^{+\infty} \cdots \int_{-\infty}^{+\infty} h_n(\tau_1, \tau_2, \ldots, \tau_n) x(t-\tau_1) x(t-\tau_2) \cdots x(t-\tau_n) d\tau_1 d\tau_2 \ldots d\tau_n + \ldots \end{aligned}, \tag{5.3}$$

in which for n=1,2,. . .,

$$h_n(\tau_1, \tau_2, \ldots, \tau_n) = 0 \qquad \text{for any } \tau_j < 0, \qquad j = 1, 2, \ldots, n. \tag{5.4}$$

Apart from a time-domain description, Volterra kernels can also be represented in the frequency domain. Assume that a second-order system is excited by a sinusoidal input

$$x(t) = A_x \cos \omega_x t. \tag{5.5}$$

The response of the first-order operator to this input is given by [4]

$$\begin{aligned} y_1(t) =& \boldsymbol{H_1}[A_x \cos \omega_x t] \\ =& A_x \mathrm{Re}(H_1(j\omega_x)e^{j\omega_x t}) \end{aligned}. \tag{5.6}$$

The response of the second-order operator to this input is given by [4]

$$\begin{aligned} y_2(t) =& \boldsymbol{H_2}[A_x \cos \omega_x t] \\ =& \frac{A_x^2}{2} \mathrm{Re}(H_2(j\omega_x, j\omega_x)e^{j2\omega_x t}) \end{aligned}. \tag{5.7}$$

The response of the third-order operator to this input is given by[4]

$$\begin{aligned} y_3(t) =& \boldsymbol{H_3}[A_x \cos \omega_x t] \\ =& \frac{A_x^3}{4} \mathrm{Re}(H_3(j\omega_x, j\omega_x, j\omega_x)e^{j3\omega_x t}) \end{aligned}. \tag{5.8}$$

5.2 Nonlinear Current Source Method

For a current source that is dependent on two voltages as

$$\begin{aligned} i(t) =& f(u(t), v(t)), \\ =& g_u u + K_{2_{g_u}} u^2 + K_{3_{g_u}} u^3 + \\ & g_v v + K_{2_{g_v}} v^2 + K_{3_{g_v}} v^3 + \\ & K_{2g_u\&g_v} uv + K_{3_{2g_u\&g_v}} u^2 v + K_{3_{g_u\&2g_v}} uv^2 + ... \end{aligned} \tag{5.9}$$

where u, v are the controlling voltages, respectively. where g_u, g_v, $K_{2_{g_u}}$, $K_{2_{g_v}}$, $K_{2g_u\&g_v}$, $K_{3_{g_u}}$, $K_{3_{g_v}}$ $K_{3_{2g_u\&g_v}}$ and $K_{3_{g_u\&2g_v}}$ are the first, second, third order nonlinear coefficients, which are defined by [4]

$$g_u = \frac{\partial i}{\partial u}, \tag{5.10}$$

$$g_v = \frac{\partial i}{\partial v}, \tag{5.11}$$

$$K_{n_{g_u}} = \frac{1}{n!}\frac{\partial^n i}{\partial^n u}, \tag{5.12}$$

$$K_{n_{g_v}} = \frac{1}{n!}\frac{\partial^n i}{\partial^n v}, \tag{5.13}$$

$$K_{m_{jg_u\&(m-j)g_v}} = \frac{1}{j!}\frac{1}{(m-j)!}\frac{\partial^m i}{\partial^j u \partial^{(m-j)} v}. \tag{5.14}$$

Then the second-order virtual current source consists of two virtual current sources for each controlling voltages, as well as a cross-term [4]

$$\begin{aligned} i_{NL2g}(u,v) =& i_{NL2g}(u) + i_{NL2g}(v) \\ &+ \frac{1}{2}K_{2g_u\&g_v}[\boldsymbol{H_{1u}}(s_1)\boldsymbol{H_{1v}}(s_2) + \boldsymbol{H_{1v}}(s_1)\boldsymbol{H_{1u}}(s_2)], \end{aligned} \tag{5.15}$$

where $\boldsymbol{H_{1u}(s)}$ and $\boldsymbol{H_{1v}(s)}$ is the first-order transfer function of the first controlling voltage u and v evaluated at frequency s, respectively.

$$i_{NL2_g}(u) = K_{2_{g_u}}\boldsymbol{H_{1u}}(s_1)\boldsymbol{H_{1u}}(s_2), \tag{5.16}$$

$$i_{NL2_g}(v) = K_{2_{g_v}}\boldsymbol{H_{1v}}(s_1)\boldsymbol{H_{1v}}(s_2). \tag{5.17}$$

$K_{2_{g_u}}$ and $K_{2_{g_v}}$ are the second-order nonlinearity coefficient that determines the second-order response of i to u and i to v, respectively.

The third-order virtual current source consists of two virtual current sources for each controlling voltages, as well as a cross-term [4]

$$\begin{aligned} i_{NL3g}(u,v) =& i_{NL3_g}(u) + i_{NL3_g}(v) \\ & i_{NL3C1_g}(u,v) + i_{NL3C2_g}(u,v) + i_{NL3C3_g}(u,v). \end{aligned}, \tag{5.18}$$

where

$$
\begin{aligned}
i_{NL3_g}(u) = & K_{3_{gu}} \boldsymbol{H_{1u}}(s_1)\boldsymbol{H_{1u}}(s_2)\boldsymbol{H_{1u}}(s_3) \\
& + \frac{2}{3} K_{2_{gu}} [\boldsymbol{H_{1u}}(s_1)\boldsymbol{H_{2u}}(s_2, 2_3) + \boldsymbol{H_{1u}}(s_2)\boldsymbol{H_{2u}}(s_1, s_3)], \\
& + \boldsymbol{H_{1u}}(s_3)\boldsymbol{H_{2u}}(s_1, s_2)],
\end{aligned}
\tag{5.19}
$$

$$
\begin{aligned}
i_{NL3_g}(v) = & K_{3_{gv}} \boldsymbol{H_{1v}}(s_1)\boldsymbol{H_{1v}}(s_2)\boldsymbol{H_{1v}}(s_3) \\
& + \frac{2}{3} K_{2_{gv}} [\boldsymbol{H_{1v}}(s_1)\boldsymbol{H_{2v}}(s_2, 2_3) + \boldsymbol{H_{1v}}(s_2)\boldsymbol{H_{2v}}(s_1, s_3)], \\
& + \boldsymbol{H_{1v}}(s_3)\boldsymbol{H_{2v}}(s_1, s_2)],
\end{aligned}
\tag{5.20}
$$

$$
\begin{aligned}
i_{NL3C1_g}(u, v) = \frac{1}{3} K_{2_{gu\&gv}} \cdot & [\boldsymbol{H_{1u}}(s_2)\boldsymbol{H_{2v}}(s_1, s_3) + \boldsymbol{H_{1u}}(s_1)\boldsymbol{H_{2v}}(s_2, s_3) \\
& + \boldsymbol{H_{1u}}(s_3)\boldsymbol{H_{2v}}(s_1, s_2) + \boldsymbol{H_{1v}}(s_2)\boldsymbol{H_{2u}}(s_1, s_3) \quad , \\
& + \boldsymbol{H_{1v}}(s_1)\boldsymbol{H_{2u}}(s_2, s_3) + \boldsymbol{H_{1v}}(s_3)\boldsymbol{H_{2u}}(s_1, s_2)],
\end{aligned}
\tag{5.21}
$$

$$
\begin{aligned}
i_{NL3C2_g}(u, v) = \frac{1}{3} K_{3_{2gu\&gv}} \cdot & [\boldsymbol{H_{1u}}(s_1)\boldsymbol{H_{1u}}(s_2)\boldsymbol{H_{1v}}(s_3) + \boldsymbol{H_{1u}}(s_1)\boldsymbol{H_{1u}}(s_3)\boldsymbol{H_{1v}}(s_2) \\
& + \boldsymbol{H_{1u}}(s_2)\boldsymbol{H_{1u}}(s_3)\boldsymbol{H_{1v}}(s_1)],
\end{aligned}
, \tag{5.22}
$$

$$
\begin{aligned}
i_{NL3C3_g}(u, v) = \frac{1}{3} K_{3_{gu\&2gv}} \cdot & [\boldsymbol{H_{1u}}(s_1)\boldsymbol{H_{1v}}(s_2)\boldsymbol{H_{1v}}(s_3) + \boldsymbol{H_{1u}}(s_1)\boldsymbol{H_{1v}}(s_3)\boldsymbol{H_{1v}}(s_2) \\
& + \boldsymbol{H_{1u}}(s_2)\boldsymbol{H_{1v}}(s_3)\boldsymbol{H_{1v}}(s_1)],
\end{aligned}
, \tag{5.23}
$$

where $K_{3_{gu}}$ and $K_{3_{gv}}$ are the third-order nonlinearity coefficient that determines the third-order response of i to the controlling voltage u and v, respectively. The completed formulations for first-, second and third-order derivatives of capacitive source that is dependent on two voltages can be found in [4].

5.3 Realization of Nonlinear Source Derivatives Calculation

I_N in Mextram is a function of $V_{B_2E_1}$ and $V^{\star}_{B_2C_2}$. $I_{C_1C_2}$ is calculated by $V_{B_2C_1}$ and $V_{B_2C_2}$. A Volterra series analysis program is developed below with a modified circuit topology that more closely resembles that of an ideal transistor equivalent circuit where the base-emitter and base-collector voltages control all circuit elements. So I'_N is only dependent on two controlling voltages, $V_{B_2C_1}$ and $V_{B_2E_1}$.

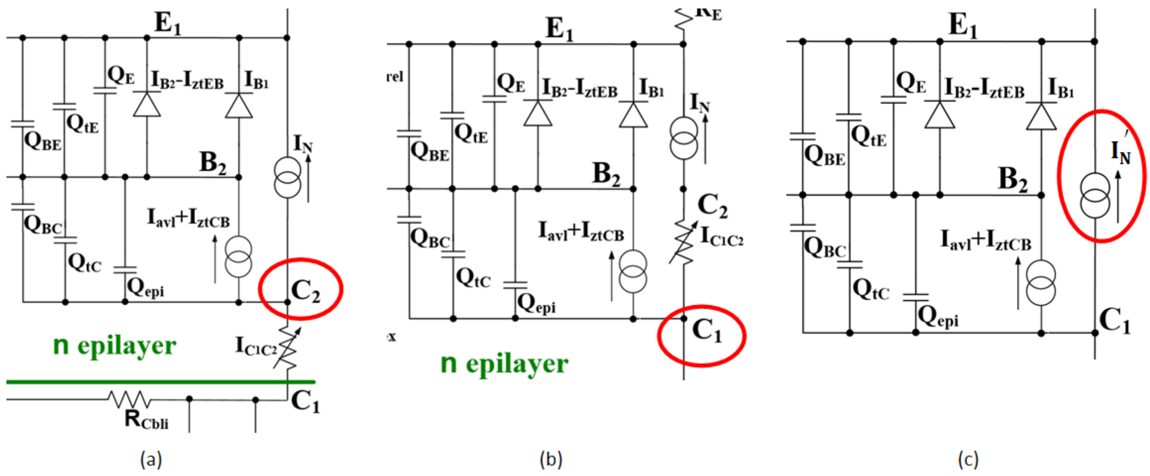

Figure 5.2: (a) Locations of I_N and $I_{C_1C_2}$ in Mextram. (b) I_N equals $I_{C_1C_2}$. (c) Combine I_N and $I_{C_1C_2}$ together into I'_N.

Fig. 5.2(a) shows I_N between C_2 and E_1 and $I_{C_1C_2}$ between C_1 and C_2 in Mextram. I_N and $I_{C_1C_2}$ are calculated by

$$I_N = I_N(V_{B_2E_1}, V^{\star}_{B_2C_2}), \tag{5.24}$$

$$I_{C_1C_2} = I_{C_1C_2}(V_{B_2E_1}, V_{B_2C_2}). \tag{5.25}$$

Fig. 5.2(b) shows I_N is in series with $I_{C_1C_2}$ after node change and then

$$I_N(V_{B_2E_1}, V^{\star}_{B_2C_2}) = I_{C_1C_2}(V_{B_2E_1}, V_{B_2C_2}). \tag{5.26}$$

Fig. 5.2(c) shows an equivalent main current I'_N, which is calculated by

$$I'_N = I'_N(V_{B_2E_1}, V_{B_2C_1}), \tag{5.27}$$

The DC, Y-parameter and IP3 at the bias of interest have been checked without much influence before and after node change approximation is applied.

The following will take i'_N dependent on $V_{B_2C_1}$ and $V_{B_2E_1}$ as an example to derive the first- and higher order derivative of I'_N on $V_{B_2C_1}$ and $V_{B_2E_1}$, respectively. The self-heating treatment will be also described below.

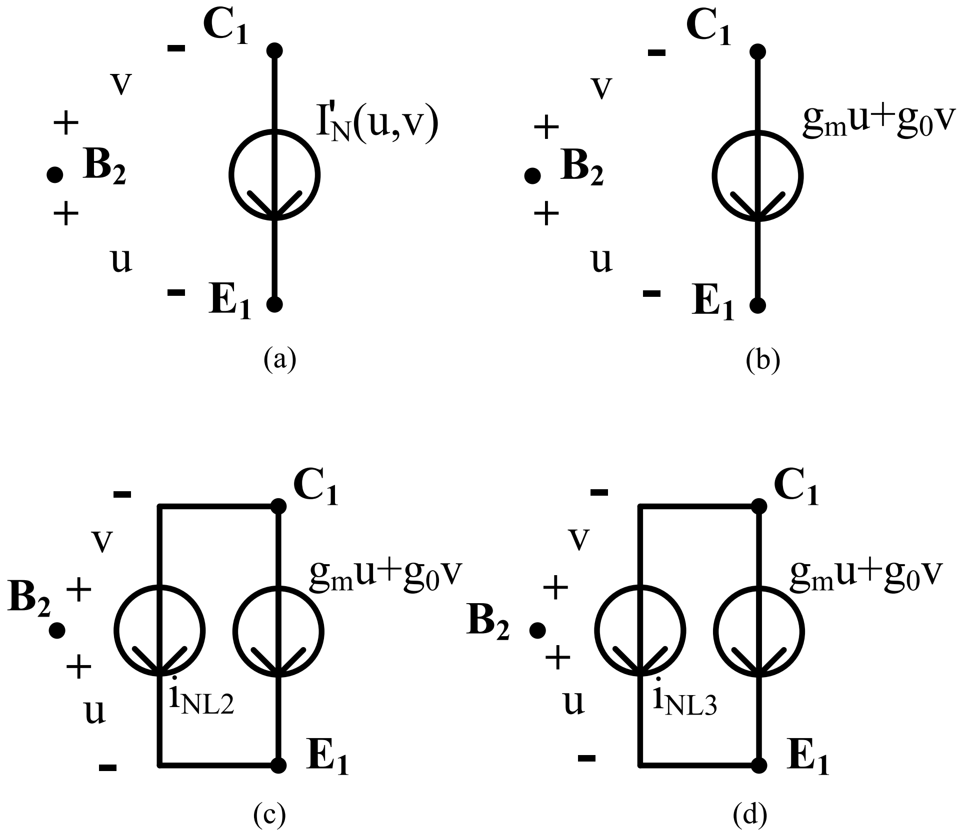

Figure 5.3: (a) i'_N dependence on u and v. (b) Network for first-order transfer function. (c) Network for second-order transfer function. (d) Network for third-order transfer function.

Fig. 5.3(a) shows i'_N dependence on u and v, where u denotes $V_{B_2E_1}$ and v denotes $V_{B_2C_1}$.

$$i'_N(u,v) = i'_N(V_{B_2E_1}, V_{B_2C_1}). \tag{5.28}$$

Fig. 5.3(b) shows the first order partial derivative of I'_N on $V_{B_2E_1}$ and $V_{B_2C_1}$, denoted as g_m and g_0, respectively.

$$g_m = \left.\frac{\partial I'_N}{\partial V_{B_2E_1}}\right|_{V_{B_2C_1}}. \tag{5.29}$$

$$g_0 = \left.\frac{\partial I'_N}{\partial V_{B_2C_1}}\right|_{V_{B_2E_1}}. \tag{5.30}$$

However, holding $V_{B_2C_1}$ constant while changing $V_{B_2E_1}$ also changes $V_{B_2C_2}$, so the "ddx()" cannot be directly used to calculate g_m or g_0. Instead, the following formulas are derived

$$\begin{aligned} g_m =& \left.\frac{\partial I'_N}{\partial V_{B_2E_1}}\right|_{V_{B_2C_1}} \\ =& \left.\frac{\partial I_N}{\partial V_{B_2E_1}}\right|_{V_{B_2C_1},V_{B_2C_2}} + \left.\frac{\partial I_N}{\partial V_{B_2C_2}}\right|_{V_{B_2E_1},V_{B_2C_1}} \cdot \left.\frac{\partial V_{B_2C_2}}{\partial V_{B_2E_1}}\right|_{V_{B_2C_1}}, \end{aligned} \tag{5.31}$$

where each partial derivative term can be then symbolically obtained by ddx() as

$$\left.\frac{\partial I_N}{\partial V_{B_2E_1}}\right|_{V_{B_2C_1},V_{B_2C_2}} = -ddx(I'_N, V(E_1)), \tag{5.32}$$

$$\left.\frac{\partial I_N}{\partial V_{B_2C_2}}\right|_{V_{B_2E_1},V_{B_2C_1}} = -ddx(I'_N, V(C_2)), \tag{5.33}$$

$$\left.\frac{\partial V_{B_2C_2}}{\partial V_{B_2E_1}}\right|_{V_{B_2C_1}} = -\frac{-ddx(I_{C_1C_2}, V(E_1)) + ddx(I'_N, V(E_1))}{-ddx(I_{C_1C_2}, V(C_2)) + ddx(I'_N, V(C_2))}. \tag{5.34}$$

Also a similar derivation can be applied to g_0 as

$$\begin{aligned} g_0 =& \left.\frac{\partial I'_N}{\partial V_{B_2C_1}}\right|_{V_{B_2E_1}} \\ =& \left.\frac{\partial I_N}{\partial V_{B_2C_1}}\right|_{V_{B_2E_1},V_{B_2C_2}} + \left.\frac{\partial I_N}{\partial V_{B_2C_2}}\right|_{V_{B_2E_1},V_{B_2C_1}} \cdot \left.\frac{\partial V_{B_2C_2}}{\partial V_{B_2C_1}}\right|_{V_{B_2E_1}}, \end{aligned} \tag{5.35}$$

where each partial derivative term can be then symbolically obtained by ddx() as

$$\left.\frac{\partial I_N}{\partial V_{B_2C_1}}\right|_{V_{B_2E_1},V_{B_2C_2}} = -ddx(I'_N, V(C_1)), \tag{5.36}$$

$$\left.\frac{\partial I_N}{\partial V_{B_2C_2}}\right|_{V_{B_2E_1},V_{B_2C_1}} = -ddx(I'_N, V(C_2)), \tag{5.37}$$

$$\left.\frac{\partial V_{B_2C_2}}{\partial V_{B_2C_1}}\right|_{V_{B_2E_1}} = -\frac{-ddx(I_{C_1C_2}, V(C_1)) + ddx(I'_N, V(C_1))}{-ddx(I_{C_1C_2}, V(C_2)) + ddx(I'_N, V(C_2))}. \tag{5.38}$$

Fig. 5.3(c) and (d) show the networks for second- and third-order transfer function, respectively. i_{NL2} an i_{NL3} are the second- and third-order virtual current sources, whose formulations are listed in the last section. So the following second- and third-order partial derivatives of I'_N

on $V_{B_2C_1}$, $V_{B_2E_1}$ and cross terms need to be numerically calculated

$$K_{n_u} = \frac{1}{n!}\frac{\partial^n I'_N}{\partial^n V_{B_2E_1}}, \qquad n = 2, 3... \tag{5.39}$$

$$K_{n_v} = \frac{1}{n!}\frac{\partial^n I'_N}{\partial^n V_{B_2C_1}}, \qquad n = 2, 3... \tag{5.40}$$

$$K_{m_{ju(m-j)v}} = \frac{1}{j!}\frac{1}{(m-j)!}\frac{\partial^m I'_N}{\partial^j V_{B_2E_1}\partial^{(m-j)} V_{B_2C_1}}. \qquad m, j = 2, 3...\text{and } j < m. \tag{5.41}$$

To evaluate the values of higher order derivatives, the following numerical calculation is used. Fig. 5.4 shows small perturbations of 10^{-6} V are added to generate ΔV_{EBsm} and

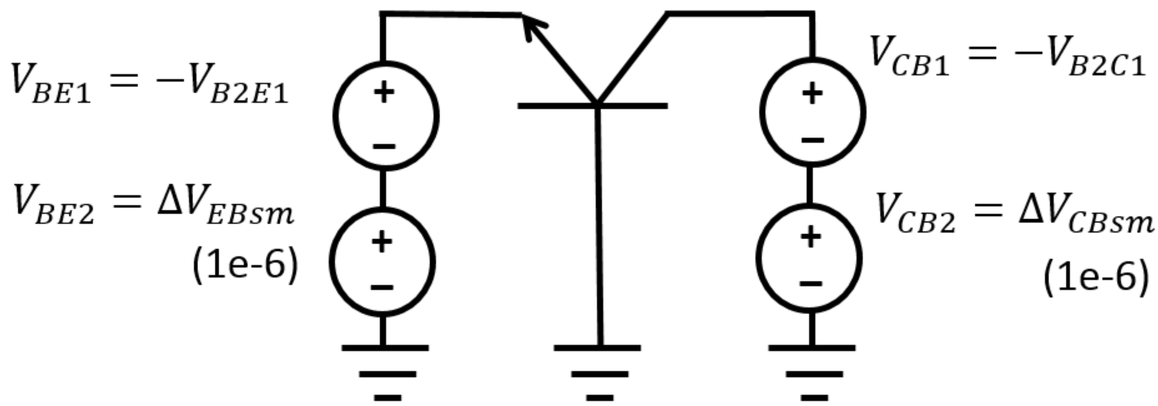

Figure 5.4: The calculation of second- and third-order partial derivative of current and charges in intrinsic circuit.

ΔV_{CBsm} needed for the calculation of higher order derivatives using numerical differentiation for each $V_{B_2C_1}$ and $V_{B_2E_1}$. The $V_{B_2C_1}$ and $V_{B_2E_1}$ are simulated first and used to bias only the intrinsic transistor. The nonlinear coefficients are then used to calculate the first, second and third order Volterra kernels using the nonlinear current source method [2]. The Volterra kernels are calculated in the increasing order by repeatedly solving the same linear network as in linear small-signal analysis [4] [2]. The first order kernel is essentially a linear transfer function. The second and third order kernels are solved by exciting the same linear network with virtual nonlinear current sources i_{NL2} and i_{NL3} placed in parallel with the corresponding linearized elements.

The self-heating effect at each bias should be also carefully considered. Tab. 5.1 shows

	Symbolic result	Numerical result	V(dT)
No self-heating	-2.236395	-2.236395	0
With self-heating	-2.363449	-3.520327	1.46
Using DTA=V(dT) and no self-heating	-2.363449	-2.363449	0

Table 5.1: A treatment of self-heating effect in numerical calculation of partial derivative of I'_N on $V_{B_2C_1}$ at $V_{B_2E_1}$ = 0.7 V and $V_{B_2C_1}$ = -1 V.

a treatment of self-heating effect in numerical calculation of partial derivative of I'_N on $V_{B_2C_1}$ at $V_{B_2E_1}$ = 0.7 V and $V_{B_2C_1}$ = -1 V. In order to testify the accuracy, the symbolic result from ddx() is also provided as a standard. Even with a small V(dT), the numerical calculation largely deviates from symbolic result. Only when setting DTA=V(dT) and manually turning off self-heating in the calculations, then the numerical result agrees well with symbolic result.

5.4 Verification and Analysis of Volterra Series Result

To examine the accuracy of Volterra series implementation of Mextram, the real and imaginary parts of the first, second and third order derivatives of output voltage calculated from Volterra series are compared with those from harmonic balance analysis in ADS. The same parameters used below, between ADS simulation and Volterra series analysis in Matlab calculation, are based on a good DC and f_T fitting by using Mextram 505.00 with the extended avalanche model.

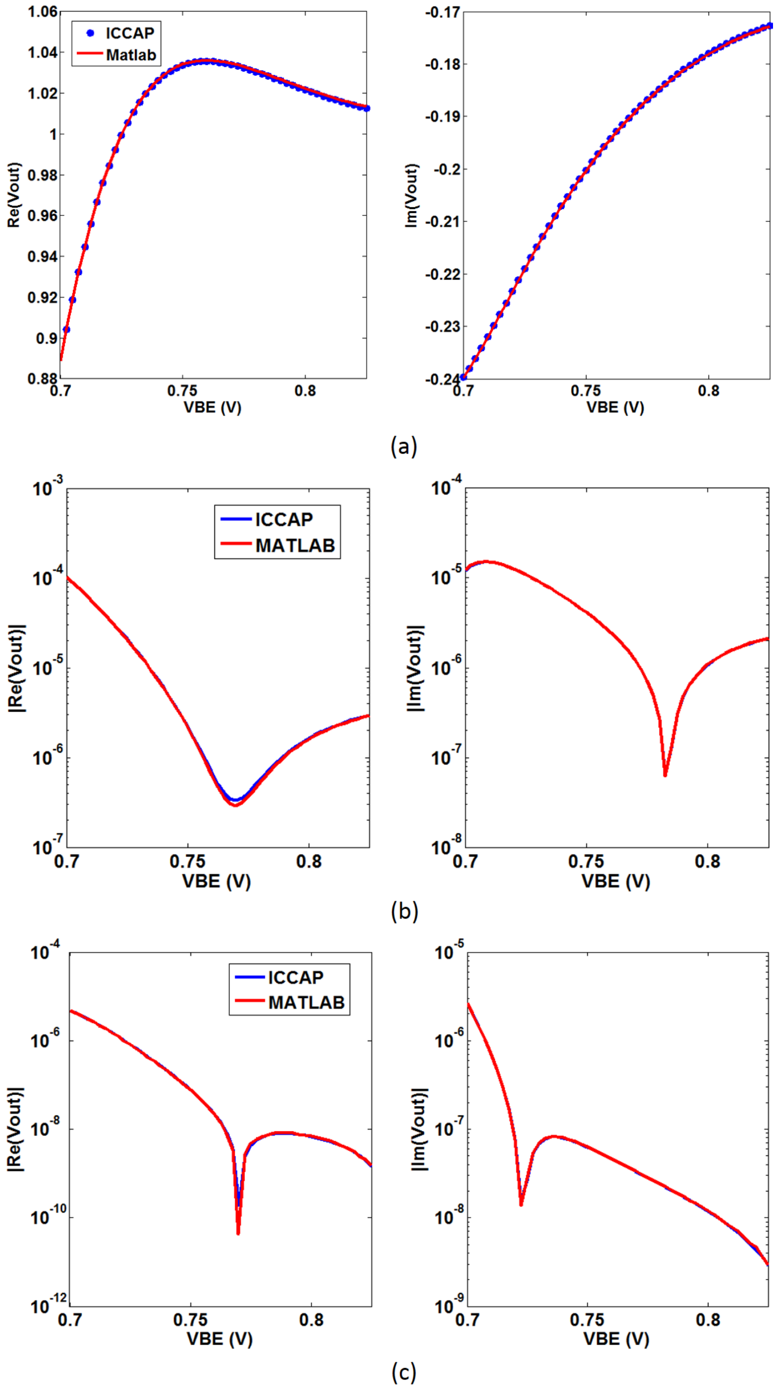

Figure 5.5: A comparison between V_{BE} dependence of harmonic balance simulated in ADS and Volterra series calculated in Matlab for real and imaginary parts of (a) first order, (b) second order and (c) third order of output voltage. V_{CB} = 3.75 V.

Fig. 5.5 shows a comparison of V_{BE} dependence of real and imaginary parts of first, second and third order of output voltages between harmonic balance and Volterra series. So a high accuracy has been achieved for V_{BE} dependence of each order calculation of output voltage using Volterra series analysis at V_{CB} = 3.75 V.

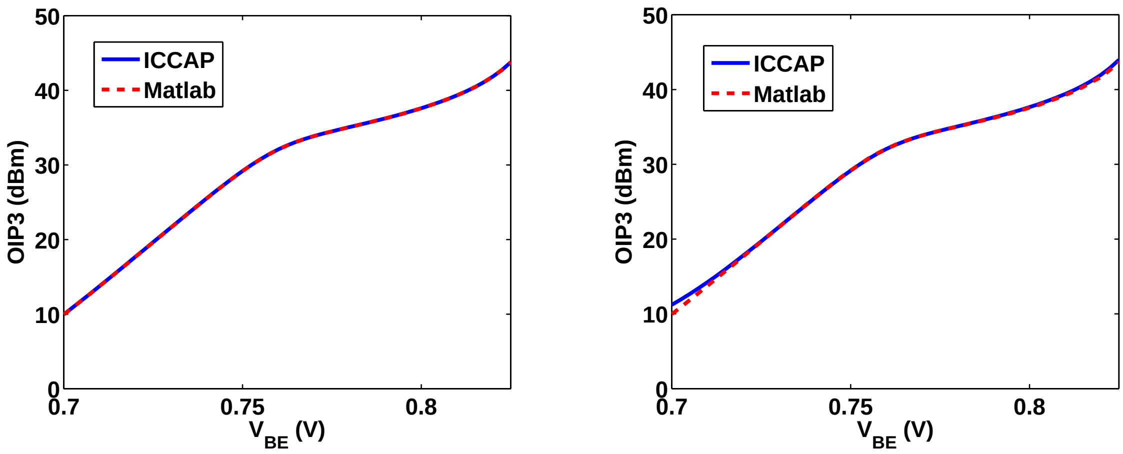

(a) (b)

Figure 5.6: For (a) P_{in} = -10 dBm, (b) P_{in} = -30 dBm, the measured (symbols), simulated (solid lines) and calculated (dash lines) OIP3 versus V_{BE} at V_{CB} = 3.75 V.

Fig. 5.6(a) shows the measured, harmonic balance simulated and Volterra series calculated OIP3 versus V_{BE} at V_{CB} = 3.75 V for P_{in} = -30 dBm. The calculated OIP3 matches well with simulated OIP3 at V_{BE} from 0.7 to 0.825 V, as expected. Fig. 5.6(b) shows the measured, harmonic balance simulated and Volterra series calculated OIP3 versus V_{BE} at V_{CB} = 3.75 V for P_{in} = -10 dBm. The calculated OIP3 matches well with simulated OIP3 at $V_{BE} > 0.72$ V. The OIP3 difference seen in the V_{BE} range from 0.7 to 0.72 V is due to P_{in} = -10 dBm. The measured OIP3 can be fitted well up to 0.76 V. However, a clear difference is observed at V_{BE} > 0.76 V, although a good fitting of DC and f_T is shown.

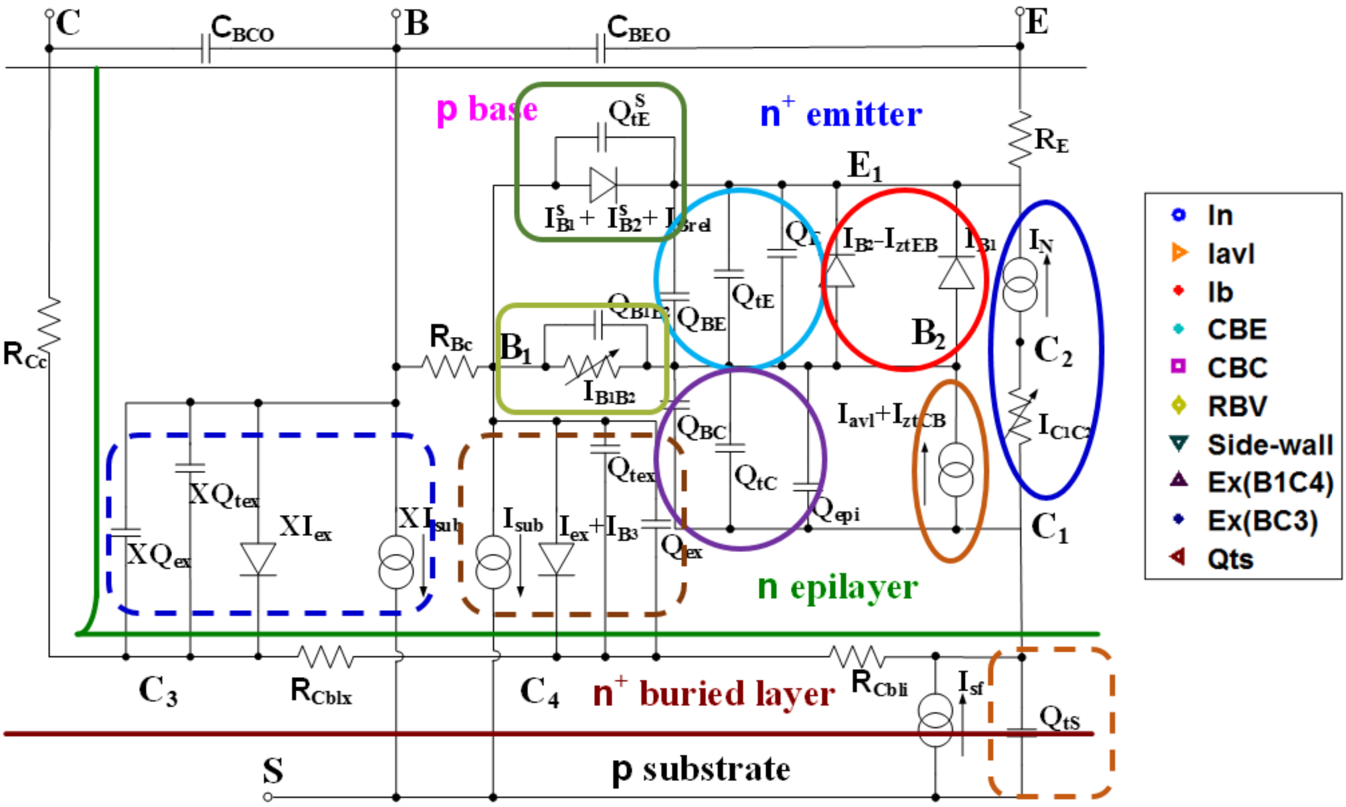

Figure 5.7: Combination of nonlinearity sources in complete MEXTRAM circuit into several groups.

Fig. 5.7 shows several groups of nonlinearity sources in complete MEXTRAM circuit. The following analysis will shows the relative importance of each group in OIP3 calculation from different ways.

Fig. 5.8(a) shows the calculated OIP3-V_{BE} with only one nonlinearity source current turned on in both second- and third-order output voltages calculation for V_{CB} = 3.75 V. It can be clearly seen that main current determines overall distortion at low V_{BE} up to 0.77 V. Then contribution of avalanche current cancels with main current at high V_{BE}, which makes overall OIP3 decrease with increasing V_{BE}. Fig. 5.8(b) shows the calculated OIP3-V_{CB} with only one nonlinearity source current turned on in second- and third-order output voltages calculation for I_E = 40 mA. At low $V_{CB} < 0.5$ V, the overall OIP3 is determined by main current, intrinsic CB charges and Q_{tS}. A increasing distortion of avalanche current and main current dominates the overall OIP3 at high $V_{CB} > 1$ V. A peak OIP3 also appears around V_{CB} = 3 V due to cancellation of avalanche and main current nonlinearities.

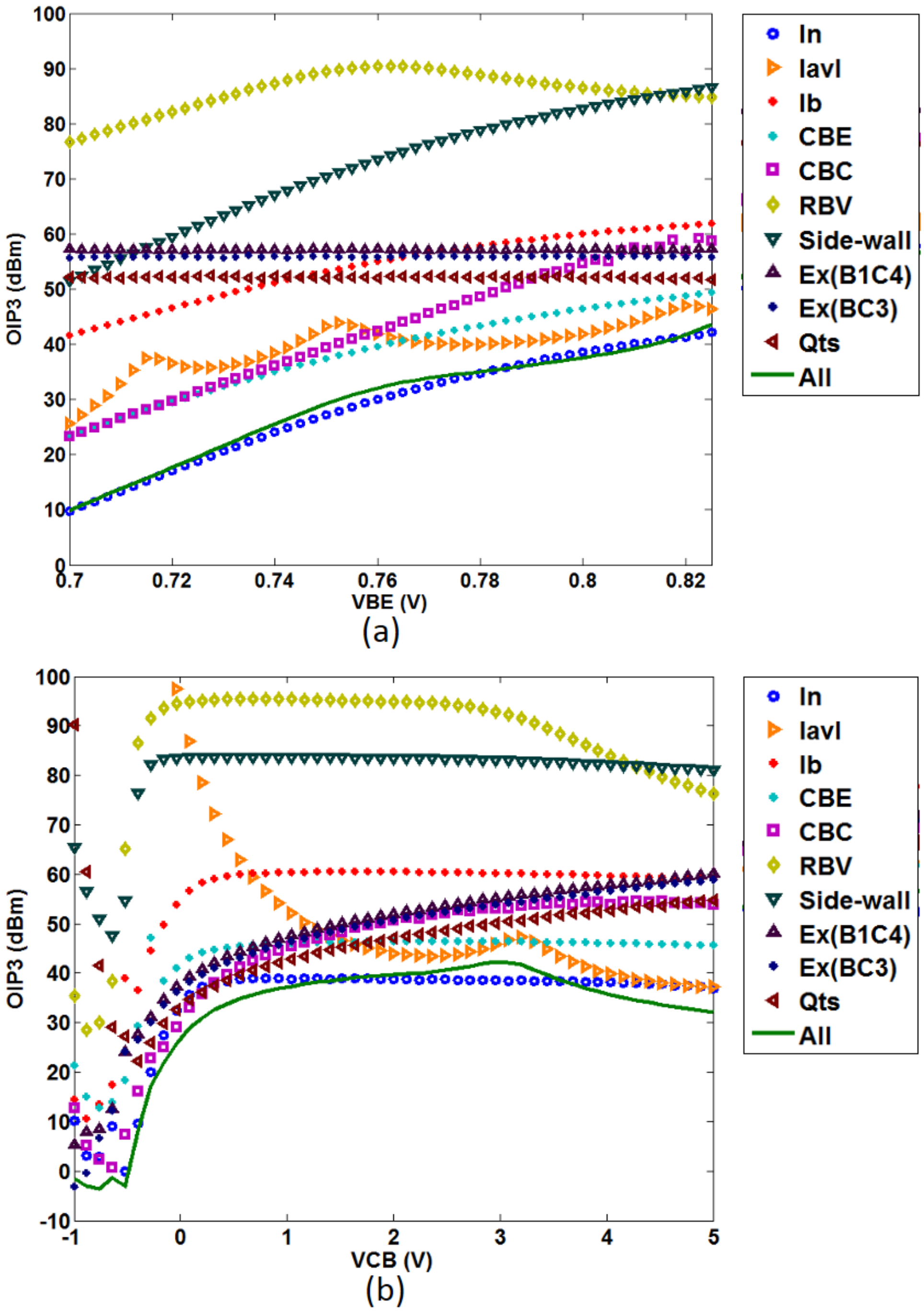

Figure 5.8: (a) The calculated OIP3-V_{BE} with only one nonlinearity source current turned on in second- and third-order output voltages calculation for V_{CB} = 3.75 V. (b) The calculated OIP3-V_{CB} with only one nonlinearity source current turned on in second- and third-order output voltages calculation for I_E = 40 mA.

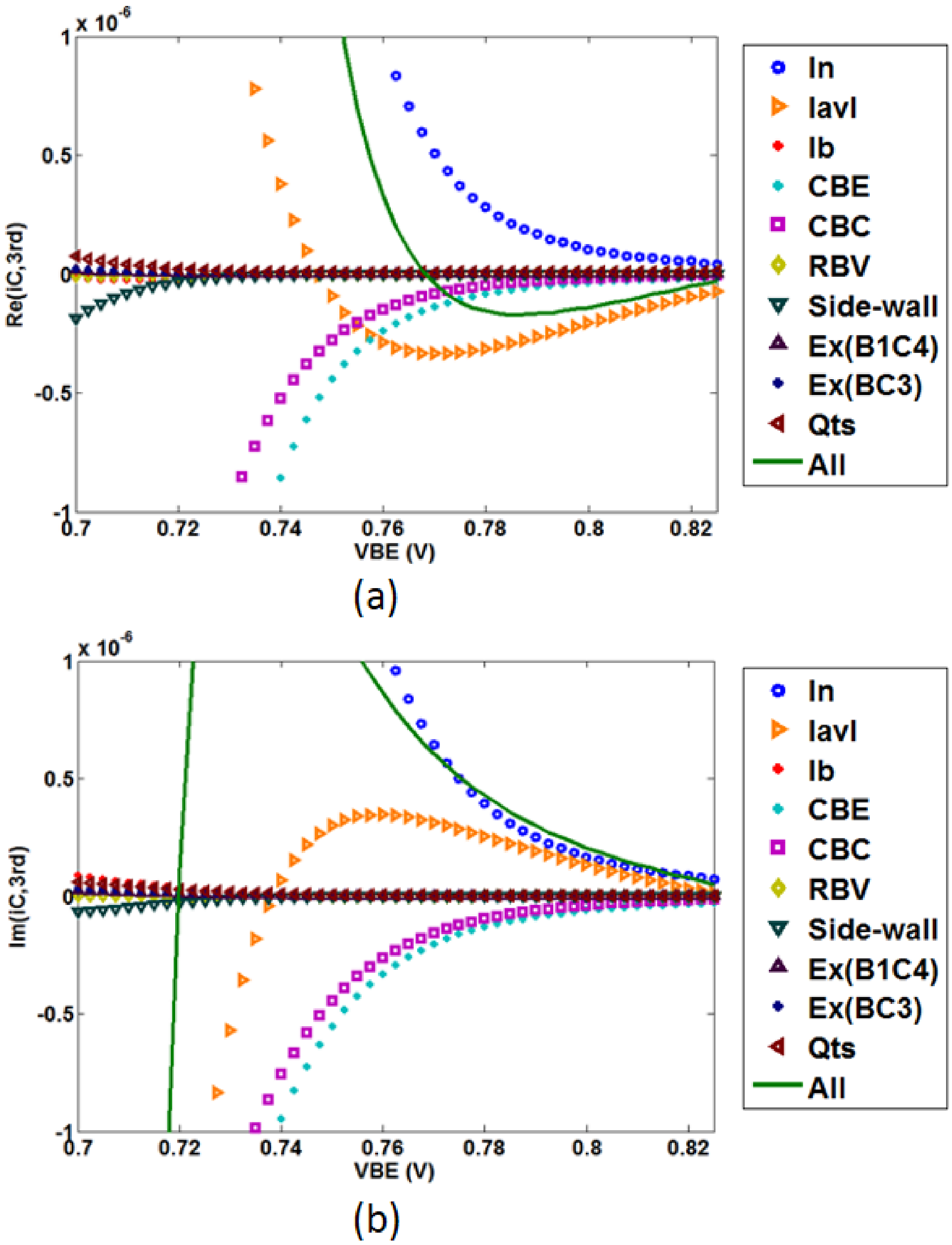

Figure 5.9: The calculated (a)real and (b)imaginary parts of $i_{C,3rd}$ versus V_{BE}. The contribution of each component on $i_{C,3rd}$ has been calculated separately. V_{CB} = 3.75 V.

Fig. 5.9(a) shows the calculated real part of $i_{C,3rd}$-V_{BE} with only one nonlinearity source current turned on in third-order output voltages calculation for V_{CB} = 3.75 V. At high $V_{BE} >$ 0.74 V, avalanche current becomes negative and cancels with main current, which makes real part of $i_{2,3rd}$ decrease and then increase with increasing V_{BE}. Fig. 5.9(b) shows the calculated imaginary part of $i_{C,3rd}$-V_{CB} with only one nonlinearity source current in third-order output voltages calculation for V_{CB} = 3.75 V. At high $V_{BE} >$ 0.74 V, both avalanche and main current keep positive and decrease, making overall imaginary part of $i_{2,3rd}$ monotonically decrease with increasing V_{BE}.

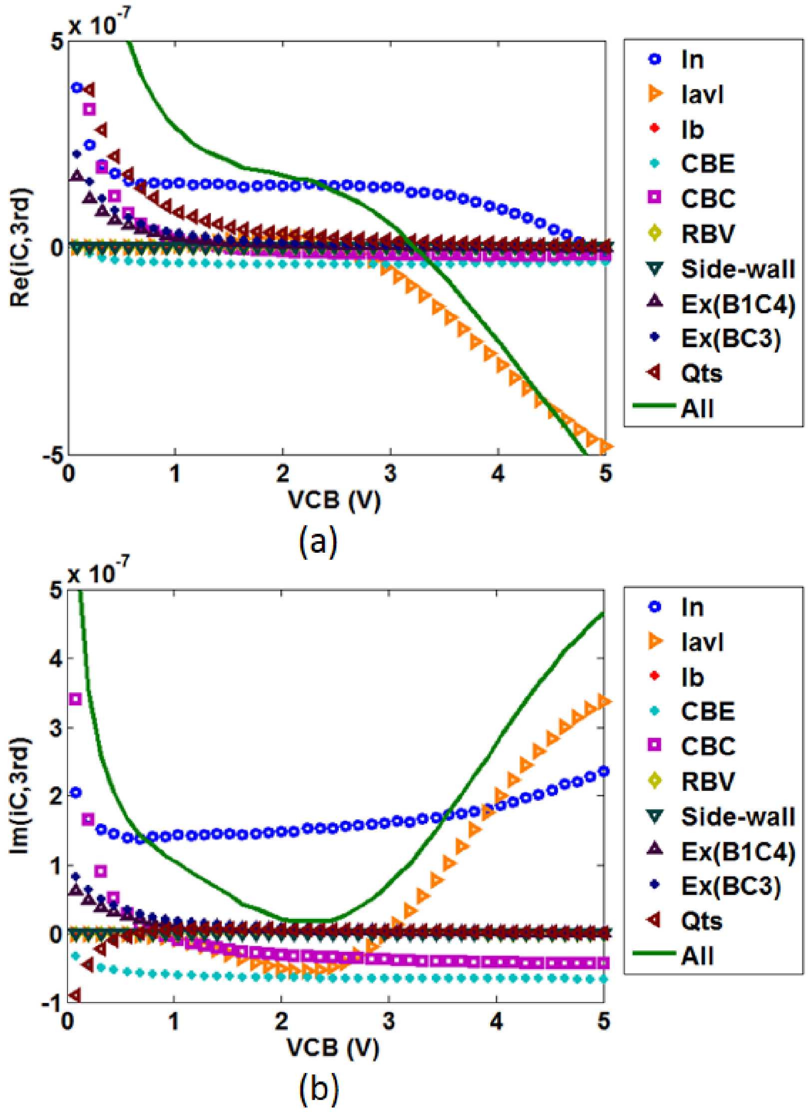

Figure 5.10: The calculated (a)real and (b)imaginary parts of $i_{C,3rd}$ versus V_{CB}. The contribution of each component on $i_{C,3rd}$ has been calculated separately. I_E = 40 mA.

Fig. 5.10(a) shows the calculated real part of $i_{C,3rd}$-V_{CB} with only one nonlinearity source current in third-order output voltages calculation for I_E = 40 mA. At $V_{CB} > 3$ V, avalanche current becomes negative and cancels out with main current, which eventually makes real part of $i_{2,3rd}$ decrease with increasing V_{CB}. Fig. 5.10(b) shows the calculated imaginary part of $i_{C,3rd}$-V_{CB} with only one nonlinearity source current in third-order output voltages calculation for I_E = 40 mA. The avalanche current determines the trend of overall imaginary part of $i_{C,3rd}$ over all V_{CB}, while other contributions almost keep constant.

Chapter 6

Common-Base IP3 modeling

This chapter will show the performance in modeling V_{BE} and V_{CB} dependence of OIP3 from Mextram 504.12, Mextram 505.00 and newly developed extended avalanche model.

6.1 Mextram 504.12 Performance

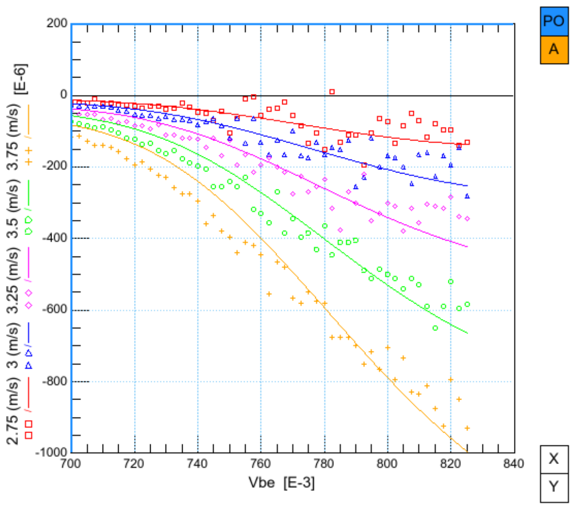

Figure 6.1: Measured and Mextram 504.12 simulated I_B-V_{BE} for V_{CB} from 2.75 to 3.75 V.

With best DC fitting by using Mextram 504.12, Fig. 6.1 shows measured and simulated I_B-V_{BE} for V_{CB} from 2.75 to 3.75 V. As only two dedicated parameters W_{AVL} and V_{AVL} provided, the simulated I_B at $V_{BE} < 0.78$ V becomes smaller than measurement for high V_{CB}, if keeping I_B well fitted at $V_{BE} > 0.78$ V.

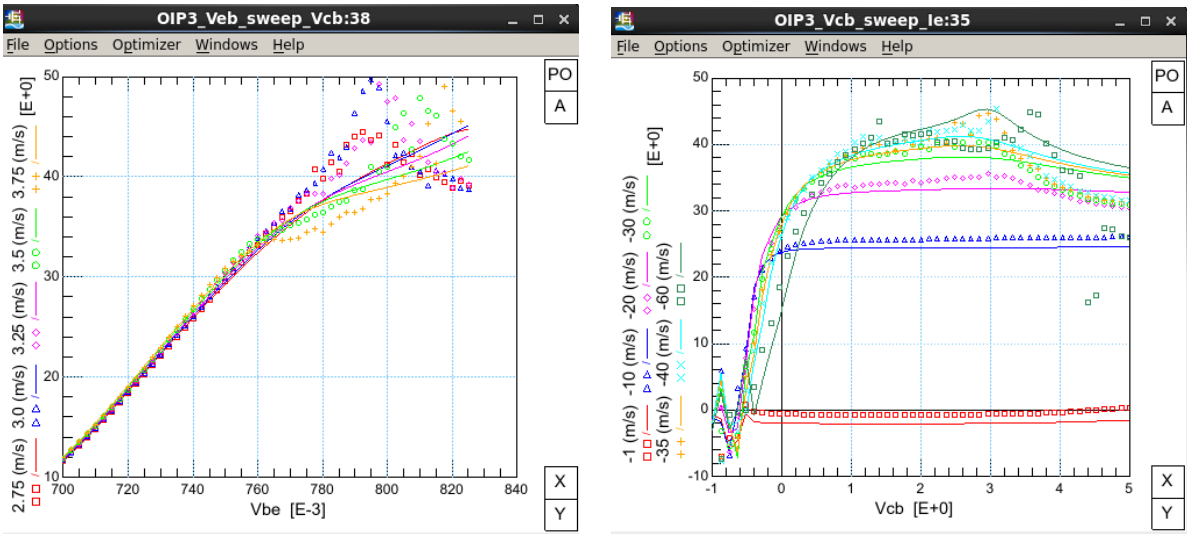

(a) (b)

Figure 6.2: Measured and MEXTRAM 504.12 simulated (a) OIP3-V_{BE} for V_{CB} from 2.75 to 3.75 V and (b) OIP3-V_{CB} for I_E from 1 to 60 mA.

Fig. 6.2(a) shows measured and Mextram 504.12 simulated OIP3-V_{BE} at V_{CB} from 2.75 to 3.75 V. A good fitting can be obtained for OIP3-V_{BE} up to 0.76 V. However, the simulated OIP3 at higher V_{BE} is way off compared to measurement where avalanche and main current dominates. So the third order of I_C is not accurately modeled, although I_B at $V_{BE} > 0.76$ V seems well fitted. Fig. 6.2(b) shows measured and Mextram 504.12 simulated OIP3-V_{CB} for I_E from 1 to 60 mA. As peak OIP3 is mainly determined by cancellation of avalanche and main current, a poor performance can be observed on OIP3-V_{CB} at $I_E > 20$ mA, which may be due to limited accuracy of avalanche model in MEXTRAM 504.12.

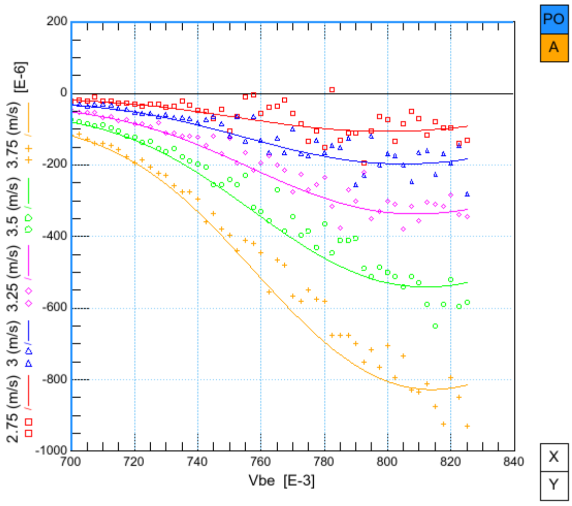

Figure 6.3: Measured and Mextram 505.00 simulated I_B-V_{BE} for V_{CB} from 2.75 to 3.75 V.

Fig. 6.3 shows measured and Mextram 505.00 simulated I_B-V_{BE} for V_{CB} from 2.75 to 3.75 V. With improved V_{CB} and I_E dependence, I_B-V_{BE} up to V_{BE} = 0.8 V can be well fitted. However, due to current dependence empirically considered through I_{TOavl} only for low current, the difference between simulated I_B and measurement is observed when V_{BE} gets larger than 0.8 V at $V_{CB} > 3.5$ V.

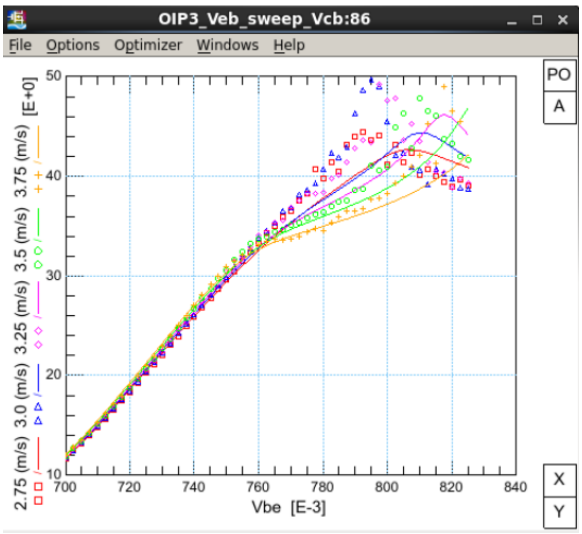

(a)

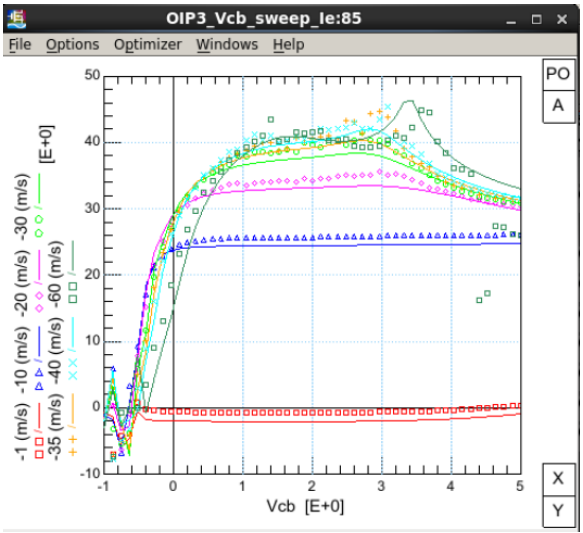

(b)

Figure 6.4: Measured and MEXTRAM 505.00 simulated (a) OIP3-V_{BE} for V_{CB} from 2.75 to 3.75 V and (b) OIP3-V_{CB} for I_E from 1 to 60 mA.

Fig. 6.4(a) shows measured and Mextram 505.00 simulated OIP3-V_{BE} for V_{CB} from 2.75 to 3.75 V. OIP3-V_{BE} can be well modeled up to 0.76 V, For larger V_{BE}, clear peaks at each V_{CB} appear due to avalanche current is well fitted up to $V_{BE} < 0.8$ V. However, the V_{BE} location where OIP3 peaks at each V_{CB} still deviates from measurement. Fig. 6.4(b) shows measured and Mextram 505.00 simulated OIP3-V_{CB} for I_E from 1 to 60 mA. Compared to Fig. 6.2(b), an overall improvement can be clearly seen at $I_E > 20$ mA due to improved avalanche model.

6.3 Extended Avalanche Model Performance

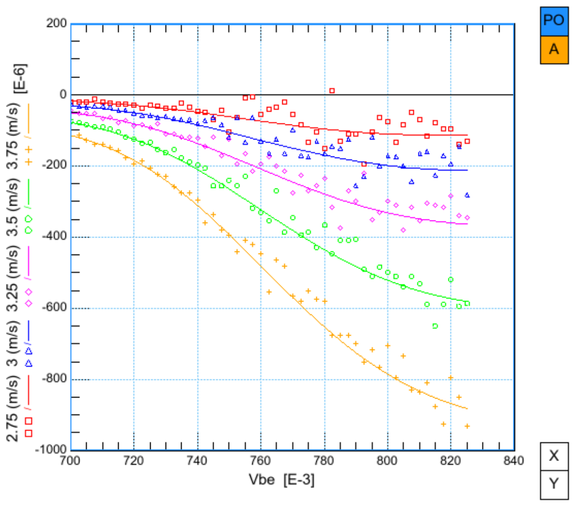

Figure 6.5: Measured and new extended avalanche model simulated I_B-V_{BE} at V_{CB} from 2.75 to 3.75 V.

Fig. 6.5 shows a good fitting of I_B-V_{BE} at V_{CB} from 2.75 to 3.75 V with new extended avalanche model. With Kirk effect at high current and a smoothing function between low to high current are accurately considered, the new extended avalanche model can provide accurate fitting on both V_{CB} and I_E dependence.

Fig. 6.6(a) shows measured and new extended avalanche model simulated OIP3-V_{BE} for V_{CB} from 2.75 to 3.75 V. As current dependence of avalanche current has been well modeled, OIP3-V_{BE} is well modeled at low V_{BE} up to 0.76 V. Compared to initial status in Fig. 1.14, OIP3-V_{BE} can be well fitted up to V_{BE} = 0.8 V for V_{CB} = 3.75 V and up to V_{BE} = 0.79 V for V_{CB} = 3.5 V, which is due to improved avalanche model at medium current. For V_{CB} = 2.75, 3 and 3.25 V, OIP3 peaks can be clearly seen but still deviate with measurement. Further

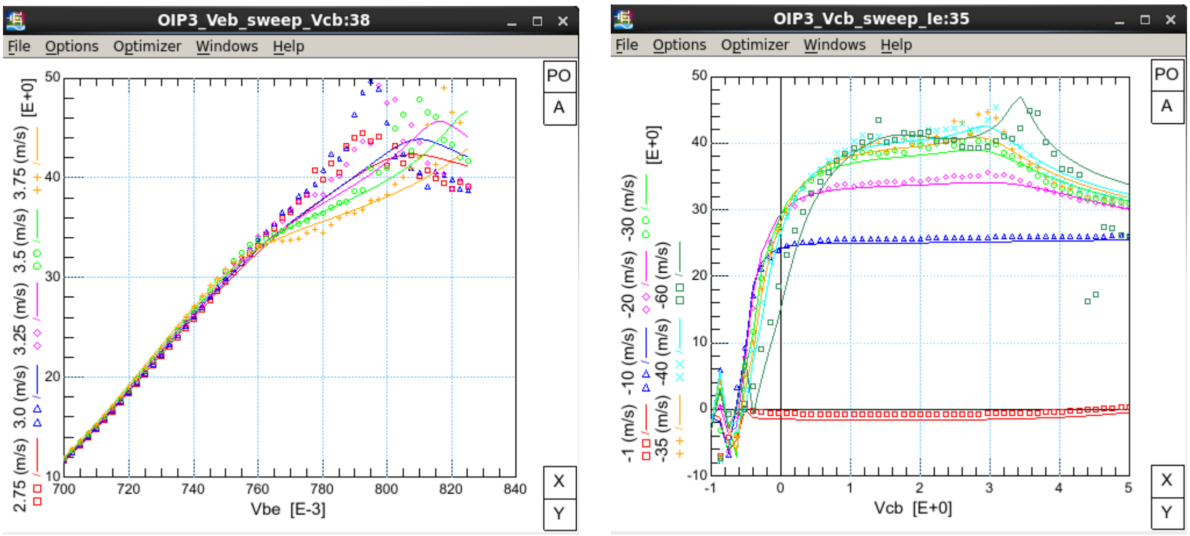

(a) (b)

Figure 6.6: Measured and new extended avalanche model simulated (a) OIP3-V_{BE} for V_{CB} from 2.75 to 3.75 V and (b) OIP3-V_{CB} for I_E from 1 to 60 mA.

improvements on above can be possibly achieved by accurate extraction of source resistance, epi-layer model parameter about high injection effect, which has not verified yet. Fig. 6.6(b) shows measured and new extended avalanche model simulated OIP3-V_{CB} for I_E from 1 to 60 mA. At I_E = 20, 30, 35 and 40 mA, the new extended avalanche model does a good job in capturing the location of the OIP3 peak. The actual values of the IP3 peak are difficult to determine accurately in both simulation and measurements, and of less practical interest than the location of IP3 peak. Compared to MEXTRAM 504.12 and MEXTRAM 505.00, an overall good performance in both DC and OIP3 is achieved by newly developed extended avalanche model.

Chapter 7

Conclusions

The importance of CB depletion capacitance model on IP3 for common-emitter SiGe HBT is detailed analysed. A new extended avalanche models is derived and verified at high current for common-base SiGe HBT. The Volterra series implementation based on MEXTRAM is realized on common-base SiGe HBT with high accuracy, which is helpful for both I_E and V_{CB} dependence of OIP3.

In chapter 3, a detailed investigation of the bias dependence of distortion, as measured by third order currents and IP3, is presented using MEXTRAM. The modeling of CB depletion capacitance, particularly its biasing current dependence is found to be critical in capturing IP3 peak characteristics that is of great importance for circuit design. New modeling options for CB depletion control voltage V_{junc} and smooth limiting transition width V_{ch} are proposed, to simultaneously fit IP3, f_T as well as a plateau of C_{BC} versus V_{BE} at high injection. Implications of each option on IP3, f_T, C_{tC} and C_{BC} are presented.

In chapter 4, the current dependence of M-1 at low current is derived with related to CB depletion capacitance. The current dependence of M-1 at high current is derived with Kirk effect considered. With a smoothing function combined both low and high currents, a comprehensive current dependence of new extended avalanche model is then proposed. A new M-1 extraction method is also proposed to accurately extract M-1 without self-heating effect at high current. Both I_E and V_{CB} dependence of new extended avalanche model are finally verified on two HV SiGe HBTs at high current.

In chapter 5, with symbolic calculation of first order derivative, numerical calculation of second, third order derivative and self-heating treatment, Volterra series analysis is implemented with Mextram. The high accuracy has been verified by first, second, third order of output voltage and OIP3 in comparison with those from harmonic balance analysis in ADS. In the I_E and V_{CB} dependence of OIP3 of interest, contributions from avalanche and main currents are two dominants to determine trend of $i_{2,3rd}$ and thus peak IP3 modeling.

In chapter 6, we show that Mextram 504.12 has limited performance on DC fitting, which directly leads to poor accuracy in IP3 modeling. Mextram 505.00 produces a good DC fitting at low current so that bias dependence of IP3 is better modeled. However, due to an empirical inclusion of current dependence only for low current, the IP3 at medium and high currents is not well modeled. A good DC fitting can be obtained with new extended avalanche model. Then an overall acceptable performance on OIP3-V_{CB} at I_E from 1 to 60 mA can be achieved. A further improvement on OIP3-V_{BE} at several V_{CB} still needs further investigation.

References

[1] G. Niu, R. van der Toorn, J. C. J. Paasschens, and W. J. Kloosterman, *The Mextram Bipolar Transistor Model, 505.00, Model Definition Document*. Auburn University, 2017.

[2] J. D. Cressler and G. Niu, *Silicon-Germanium Heterojunction Bipolar Transistors*. Artech House, 2003.

[3] M. Jaoul, C. Maneux, D. Celi, M. Schroter, and T. Zimmer, "A compact formulation for avalanche multiplication in SiGe HBTs at high injection levels," *IEEE Trans. Electron Devices*, pp. 264–270, Nov. 2018, doi:10.1109/TED.2018.2875494.

[4] P. Wambacq and W. Sansen, *Distortion Analysis of Analog Integrated Circuits*. Boston, MA: Springer, 1998, doi:10.1007/978-1-4757-5003-4.

[5] K.-M. Chen, A.-S. Peng, G.-W. Huang, H.-Y. Chen, S.-Y. H. C.-Y. Chang, H.-C. Tseng, T.-L. Hsu, and V. Liang, "Linearity and power characteristics of SiGe HBTs at high temperatures for RF applications," *IEEE Trans. Electron Devices*, vol. 52, pp. 1452–1458, Jul. 2005, doi:10.1109/TED.2005.850633.

[6] G. Qin, N. Jiang, G. Wang, and Z. Ma, "Configuration dependence of SiGe HBT linearity characteristics," *European Microwave Integrated Circuits Conference*, pp. 107–110, 2006, doi:10.1109/EMICC.2006.282762.

[7] C. M. Grens, S. Seth, and J. D. Cressler, "Common-base intermodulation characteristics of advanced SiGe HBTs," *Proc. IEEE BCTM*, pp. 244–247, 2008, doi:10.1109/BIPOL.2008.4662753.

[8] Z. Li and G. Niu, “Second order intermodulation linearity of a 200 GHz SiGe HBT technology,” *ECS Transactions*, vol. 64, no. 6, pp. 303–313, 2014, doi:10.1149/06406.0303ecst.

[9] G. Niu, H. Zhang, Y. Li, X. Ding, M. Willemsen, and A. Scholten, “Physics and compact modeling of SiGe HBT linearity using Mextram,” *ECS Transactions*, pp. 145–154, Oct. 2018, doi:10.1149/08607.0145ecst.

[10] G. Niu, Y. Li, Z. Feng, J. Pan, and D. C. Sheridan, “Characterization and modeling of intermodulation linearity in a 200 GHz SiGe HBT technology,” *Proc. IEEE BCTM*, pp. 162–165, Oct. 2006, doi:10.1109/BIPOL.2006.311165.

[11] M. C. A. M. Koolen, J. A. M. Geelen, and M. P. J. G. Versleijen, “An improved de-embedding technique for on-wafer high-frequency characterization,” *IEEE Bipolar Circuits Tech. Meet.*, pp. 188–191, Sep. 1991, doi:10.1109/BIPOL.1991.160985.

[12] G. Niu, J. D. Cressler, C. S. Webster, A. J. Joseph, and D. L. Harame, “Volterra series simulations of RF intermodulation characteristics of SiGe HBT’s,” *Tech. Digest of IEEE Topical Meeting of Silicon Monolithic Integrated Circuits in RF Systems*, pp. 142–146, Apr. 2000, doi:10.1109/SMIC.2000.844318.

[13] G. Niu, Q. Liang, J. D. Cressler, C. S. Webster, and D. Harame, “RF linearity characteristics of SiGe HBTs,” *IEEE Transactions on Microwave Theory and Techniques*, vol. 49, pp. 1558–1565, Sep. 2001, doi:10.1109/22.942567.

[14] G. Niu, Q. Liang, J. D. Cressler, C. S. Webster, and D. L. Harame, “Systematic analysis of RF distortion in SiGe HBT’s,” *Tech Digest of IEEE Radio Frequency Integrated Circuits Symposium*, pp. 147–150, May 2001, doi:10.1109/RFIC.2001.935663.

[15] J. C. J. Paasschens, W. J. Kloosterman, and R. van der Toorn, *Model Derivation of Mextram 504: The Physics behind the Model*. Koninklijke Philips Electronics, 2004.

[16] G. M. Kull, L. W. Nagel, S.-W. Lee, P. Lloyd, E. J. Predergast, and H. Dirks, "A unified circuit model for bipolar transistors including quasi-saturation effects," *IEEE Trans. Electron Devices*, pp. 1103–1113, June 1985, doi:10.1109/T-ED.1985.22081.

[17] H. K. Gummel and H. C. Poon, "An integral charge control model of bipolar transistors," *The Bell System Tech. J.*, pp. 872–852, May 1970, doi:10.1002/j.1538-7305.1970. tb01803.x.

[18] C. C. McAndrew, J. A. Seitchik, D. F. Bowers, M. Dunn, M. Foisy, I. Getreu, M. McSwain, S. Moinian, J. Parker, D. J. Roulston, M. Schroter, P. van Wijnen, and L. F. Wagner, "VBIC95, the vertical bipolar inter-company model," *IEE Journal of Solid-State Circuits*, vol. 31, no. 10, pp. 1476–1483, Oct. 1996.

[19] J. C. J. Paasschens, W. J. Kloosterman, R. J. Havens, and H. C. Graaff, "Improved compact modeling of output conductance and cutoff frequency of bipolar transistors," *IEEE J. of Solid-State Circuits*, vol. 36, no. 9, pp. 1390–1398, Sep. 2001, doi:10.1109/4.944668.

[20] J. L. Moll and I. M. Ross, "The dependence of transistor parameters on the distribution of base layer resistivity," *Proc. of the IRE*, vol. 44, pp. 72–78, Jan. 1956, doi:10.1109/ JRPROC.1956.274853.

[21] H. K. Gummel, "A charge control relation for bipolar transistor," *The Bell System Tech. J.*, vol. 49, pp. 115–120, Jan. 1970, doi:10.1002/j.1538-7305.1970.tb01759.x.

[22] ——, "A charge control relation for bipolar transistors," *The Bell Sys. Tech. J.*, pp. 115–120, Jan. 1970, doi:10.1002/j.1538-7305.1970.tb01759.x.

[23] H. Kroemer, "Two integral relations pertaining to the electron transport through a bipolar transistor with a nonuniform energy gap in the base region," *Solid-State Electrons*, pp. 1101–1103, Nov. 1985, doi:10.1016/0038-1101(85)90190-X.

[24] J. C. J. Paasschens, W. J. Kloosterman, and R. J. Havens, "Modelling two SiGe HBT specific features for circuit simulation," *IEEE Bipolar Circuits Tech. Meet.*, pp. 38–41, Oct. 2001, doi:10.1109/BIPOL.2001.957853.

[25] H. Zhang and G. Niu, "An analytical model of avalanche multiplication factor for wide temperature range compact modeling of silicon-germanium heterojunction bipolar transistors," *ECS Transactions*, vol. 75, no. 8, pp. 141–150, 2016, doi:10.1149/07508.0141ecst.

[26] A. G. Chynoweth, "Ionization rates for electrons and holes in silicon," *Physical Review*, vol. 109, pp. 1537–1540, Oct. 1958.

[27] R. Singh, M. M. Oprysko, and D. Harame, *Silicon Germanium: Technology, Modeling and Design*. Piscataway, NJ: IEEE Press, 2003.

[28] W. D. van Noor, A. Rodriguez, H. Sun, F. Zaato, N. Zhang, T. Nesheiwaat, F. Neuilly, J. Melai, and E. Hijzen, "BiCMOS technology improvements for microwave application," *Proc. IEEE BCTM*, pp. 93–96, Oct. 2008, doi:10.1109/BIPOL.2008.4662720.

[29] D. E. Root, J. Verspecht, J. Horn, and M. Marcu, *X-Parameters: Characterization, Modeling, and Design of Nonlinear RF and Microwave Components*. Cambridge University Press, 2011, doi:10.1017/CBO9781139042970.

[30] J. C. J. Paasschens, W. J. Kloosterman, R. J. Havens, and H. C. de Graaff, "Improved compact modeling of output conductance and cutoff frequency of bipolar transistors," *IEEE J. of Solid-State Circuits*, pp. 1390–1398, Sept. 2001, doi:10.1109/4.944668.

[31] N. Rinaldi and V. d'Alessandro, "Theory of electrothermal behavior of bipolar transistor: Part III-Impact ionization," *IEEE Trans. Electron Devices*, vol. 49, pp. 1683–1697, June 2006, doi:10.1109/TED.2006.876285.

[32] P. F. Lu and C. T. Chuang, "Effect of reverse base current on bipolar and BiCMOS circuits," *IEEE Trans. Electron Devices*, vol. 39, pp. 1902 – 1908, Aug. 2005, doi:10.1109/16.144682.

[33] M. Rickelt and H. M. Rein, "A novel transistor model for simulating avalanche-breakdown effects in Si bipolar circuits," *IEEE J. Solid-State Circuits*, vol. 37, pp. 1184–1197, Sep. 2002, doi:10.1109/JSSC.2002.801197.

[34] M. Reisch, *High-Frequency Bipolar Transistor: Physics, Modeling, Applications*. Springer, 2003.

[35] M. Pfost, V. Kubrak, and A. Romanyuk, “Modeling avalanche multiplication for advanced high-speed SiGe bipolar transistor,” *Silicon Monolithic Integrated Circuits in RF Systems*, pp. 18–21, Apr. 2003, doi:10.1109/SMIC.2003.1196658.

[36] G. Sasso, M. Costagliola, and N. Rinaldi, “Avalanche multiplication and pinch-in models for simulating electrical instability effects in SiGe HBTs,” *Microelectronics Reliability*, vol. 50, pp. 1577–1580, Sep. 2010, doi:10.1016/j.microrel.2010.07.081.

[37] N. Rinaldi and V. d’Alessandro, “Theory of electrothermal behavior of bipolar transistor: part III-impact ionization,” *IEEE Trans. Electron Devices*, vol. 53, no. 7, pp. 1683–1697, Jul. 2006, doi:10.1109/TED.2006.876285.

[38] G. Niu, Q. Liang, J. D. Cressler, C. S. Webster, and D. L. Harame, “RF linearity characteristics of SiGe HBTs,” *IEEE Transactions on Microwave Theory and Techniques*, vol. 49, no. 9, pp. 1558–1565, Sep. 2001, doi:10.1109/22.942567.

[39] G. Niu, H. Zhang, Y. Li, X. Ding, M. Willemsen, and A. Scholten, “Physics and compact modeling of SiGe HBT linearity using mextram,” *ECS Transactions*, vol. 86, no. 7, pp. 145–154, 2018, doi:10.1149/08607.0145ecst.

[40] W. J. Kloosterman and H. C. D. Graaff, “Avalanche multiplication in a compact bipolar transistor model for circuit simulation,” *IEEE Trans. Electron Devices*, vol. 36, no. 7, pp. 1376–1380, 1989, doi:10.1109/16.30944.

[41] M. Rickelt and H.-M. Rein, “A novel transistor model for simulating avalanche-breakdown effects in Si bipolar circuits,” *IEEE Trans. Electron Devices*, vol. 37, no. 9, pp. 1184–1197, Sep. 2002, doi:10.1109/JSSC.2002.801197.

[42] M. Pfost, V. Kubrak, and A. Romanyuk, “Modeling avalanche multiplication for advanced high-speed SiGe bipolar transistors,” *Proc. Silicon Monolithic Integr. Circuits RF Syst.*, pp. 18–21, Apr. 2003, doi:10.1109/SMIC.2003.1196658.

[43] G. Sasso, M. Costagliola, and N. Rinaldi, "Avalanche multiplication and pinch-in models for simulating electrical instability effects in SiGe HBTs," *Microelectronics Reliability*, vol. 50, no. 9, pp. 1577–1580, 2010, doi:10.1016/j.microrel.2010.07.081.

[44] W. J. Kloosterman, J. C. J. Paasschens, and R. J. Havens, "A comprehensive bipolar avalanche multiplication compact model for circuit simulation," *Proc. IEEE BCTM*, pp. 172–175, 2000, doi:10.1109/BIPOL.2000.886197.

[45] G. Niu, J. D. Cressler, S. Zhang, U. Gogineni, and D. C. Ahlgren, "Measurement of collector-base junction avalanche multiplication effects in advanced UHV/CVD SiGe HBT's," *IEEE Trans. Electron Devices*, vol. 46, pp. 1007–1015, May 1999, doi:10.1109/16.760410.

[46] P.-F. Lu and T.-C. Chen, "Collector-base junction avalanche effects in advanced double-poly self-aligned bipolar transistors," *IEEE Trans. Electron Devices*, vol. 36, pp. 1182–1188, Jun. 1989, doi:10.1109/16.24366.

[47] L. Vendrame, E. Zabotto, A. D. Fabbro, A. Zanini, and G. Verzellesi, "Influence of impact-ionization-induced base current reversal on bipolar transistor parameters," *IEEE Trans. Electron Devices*, vol. 42, pp. 1636–1646, Sept. 1995, doi:10.1109/16.405278.

[48] E. Zanoni, E. F. Crabbe, J. M. C. Stork, P. Pavan, G. Verzellesi, L. Vendrame, and C. Canali, "Extension of impact-ionization multiplication coefficient measurements to high electric field in advanced Si BJT's," *IEEE Electron Devices Letters*, vol. 14, pp. 69–71, Feb. 1993, doi:10.1109/55.215111.

[49] V. d'Alessandro and M. Schroter, "On the modeling of the avalanche multiplication coefficient in SiGe HBTs," *IEEE Trans. Electron Devices*, vol. 66, pp. 2472–2482, Jun. 2019, doi:10.1109/TED.2019.2912872.

[50] H. C. Poon and J. C. Meckwood, "Modeling of avalanche effect in integral charge control model," *IEEE Trans. Electron Devices*, vol. 19, no. 1, pp. 90–97, Jan. 1972, doi:10.1109/T-ED.1972.17376.